

Master's Thesis

Disentangling Quantum Mechanics in Top Quark Pairs at the ATLAS Experiment

Entschlüsselung der Quantenmechanik in Top-Quark-Paaren am ATLAS-Experiment

prepared by

Theresa Reisch

from Northeim

at the II. Physikalischen Institut

Thesis number: II.Physik-UniGö-MSc-2024/09

Thesis period: 1st October 2023 until 30th September 2024

First referee: Prof. Dr. Arnulf Quadt

Second referee: Prof. Dr. Ariane Frey

Abstract

This thesis presents sensitivity studies for possible measurements of quantum entanglement and quantum discord in top quark pairs at $\sqrt{s} = 13$ TeV with the ATLAS experiment using simulations of proton-proton collisions corresponding to an integrated luminosity of 140 fb^{-1} .

Quantum entanglement can be found in inseparable correlated systems. Top quark pairs are predicted to be generated in a maximally entangled state close to the production threshold. In the semileptonic decay channel, the angular separation between the decay products of the top quarks is used as an indicator of quantum entanglement. The expected result for the entanglement marker is $D = -0.598 \pm 0.006(\text{stat.}) \pm 0.017(\text{syst.})$ for $M_{t\bar{t}} < 390 \text{ GeV}$, which is more than five standard deviations from the entanglement limit.

Quantum discord quantifies the quantumness of a correlation, also found in separable states. The full spin density matrix is determined in the dileptonic decay channel to calculate quantum discord. It is separately determined for the top and the anti-top quark. The expected results for the top quark and anti-top quark discord inclusively are $\mathcal{D}_t = \mathcal{D}_{\bar{t}} = 0.07 \pm 0.4$, which are 1.7 standard deviations away from zero. The sensitivity is significantly impacted by systematic signal modelling uncertainties.

Zusammenfassung

In dieser Arbeit werden Sensitivitätsstudien für mögliche Messungen von Quantenverschränkung und Quantendiskordanz in Top-Quark-Paaren bei $\sqrt{s} = 13$ TeV mit dem ATLAS Experiment vorgestellt. Dabei werden Simulationen von Proton-Proton-Kollisionen verwendet, die einer integrierten Luminosität von 140 fb^{-1} entsprechen.

Quantenverschränkung kann in untrennbaren korrelierten Systemen gefunden werden. Top-Quark-Paare werden laut Vorhersagen in einem maximal verschränkten Zustand nahe der Produktionsschwelle erzeugt. Im semileptonischen Zerfallskanal wird der Winkelabstand zwischen den Zerfallsprodukten der Top-Quarks als Indikator für Quantenverschränkung verwendet. Das erwartete Ergebnis für den Verschränkungsmarker ist $D = -0,598 \pm 0,006(\text{stat.}) \pm 0,017(\text{syst.})$ für $M_{t\bar{t}} < 390 \text{ GeV}$, was mehr als fünf Standardabweichungen vom Verschränkungslimit entfernt ist.

Quantendiskordanz quantifiziert die Quantenhaftigkeit einer Korrelation, die auch in trennbaren Zuständen zu finden ist. Zur Berechnung der Quantendiskordanz wird die volle Spindichtematrix im dileptonischen Zerfallskanal bestimmt. Sie wird getrennt für das Top- und das Anti-Top-Quark bestimmt. Die erwarteten, inklusiven Ergebnisse für die Top-Quark- und Anti-Top-Quark-Diskordanz sind $\mathcal{D}_t = \mathcal{D}_{\bar{t}} = 0,07 \pm 0,04$, die 1,7 Standardabweichungen von Null entfernt sind. Die Sensitivität wird signifikant durch die systematischen Unsicherheiten der Signalmodellierung beeinträchtigt.

Contents

1. Introduction	1
2. Theoretical Background	3
2.1. The Standard Model of Particle Physics	3
2.2. Physics of the Top Quark	6
2.3. Quantum Correlations	10
2.3.1. Quantum Entanglement	10
2.3.2. Quantum Discord	15
3. Experimental Setup	21
3.1. The Large Hadron Collider	21
3.2. The ATLAS Experiment	22
4. Modelling and Object Reconstruction	25
4.1. Monte Carlo Simulations	25
4.2. Object Definitions	26
4.3. b -Tagging Algorithm	27
4.4. Kinematic Reconstruction of the Top-Anti-Top Quark System	29
4.4.1. Semileptonic Decay Channel	29
4.4.2. Dileptonic Decay Channel	31
5. Systematic Uncertainties	33
5.1. Signal Modelling Uncertainties	33
5.2. Experimental Uncertainties	34
6. Quantum Entanglement in the Semileptonic Decay Channel	35
6.1. Event Selection	35
6.2. Analysis Strategy	38
6.3. Sensitivity Study	41
6.3.1. Detector-Level Distributions	42
6.3.2. Curve from Detector- to Particle-Level	43

Contents

6.3.3.	Curve from Parton- to Particle-Level	46
6.3.4.	Comparison to Measurements Already Performed	49
7.	Quantum Discord in the Dileptonic Decay Channel	53
7.1.	Event Selection	53
7.2.	Analysis Strategy	53
7.2.1.	Calculation of Discord	54
7.2.2.	Profile Likelihood Unfolding	58
7.2.3.	Extraction of Spin Polarisation Coefficients	59
7.3.	Sensitivity Study	60
7.3.1.	Unfolding of Inclusive Distributions	60
7.3.2.	Unfolding of Distributions in Patches	64
8.	Conclusion and Outlook	69
A.	Uncertainty Estimation of Quantum Discord	81
A.1.	Uncertainty Propagation of the Von Neumann Entropy	81
A.2.	Uncertainty Propagation of the Construction of the Density Matrices . . .	82
A.3.	Uncertainty Estimation due to the Patch Size	83
B.	Additional Figures for the Quantum Discord of the Anti-Top Quark	85

List of Figures

2.1. Elementary particles of the Standard Model	4
2.2. Quark confinement	5
2.3. Leading order top quark pair production at the LHC	7
2.4. Semileptonic decay of a top quark pair	7
2.5. Helicity and beam spin basis	9
2.6. Hierarchy of quantum correlations	10
2.7. Entanglement as a function of $M_{t\bar{t}}$ and Θ	13
2.8. Spin configurations of top quark pair production	13
2.9. Statistical significance of quantum entanglement	15
2.10. Venn diagram on mutual information	16
2.11. Quantum discord as a function of β and θ	19
2.12. Quantum discord as a function of C_{\perp} and C_z	19
3.1. The ATLAS detector	22
3.2. Signatures of particles in the ATLAS detector	23
4.1. DL1r b -jet discriminant	28
4.2. High level structure of SPA-NET	29
6.1. Down-type jet identification efficiencies	37
6.2. Calibration curve schematic representation	39
6.3. $D_{\text{parton}}(M_{t\bar{t}})$ distribution	40
6.4. Reweighted $\cos \varphi_{ld}$ on parton-level	40
6.5. Calibration curves from detector-level to particle-level and parton-level for PYTHIA and HERWIG	41
6.6. $\cos \varphi$ with different hadronic spin analysers	42
6.7. Detector-level $\cos \varphi$	43
6.8. Detector-level $M_{t\bar{t}}$, SPA-NET hadtop detection and $\beta_{t\bar{t}}$	43
6.9. Calibration curve mapping detector-level to particle-level for signal region .	45
6.10. Calibration curves mapping detector-level to particle-level for validation regions	45

List of Figures

6.11. Calibration curve mapping parton-level to particle-level for signal region . . .	47
6.12. PYTHIA and HERWIG calibration curves mapping from parton-level to particle-level	47
6.13. Particle-level D values and entanglement limit	48
6.14. Measurement in the dileptonic channel and expected results from this thesis	50
6.15. CMS measurement in the dileptonic decay channel	51
6.16. CMS measurement in the semileptonic decay channel	51
7.1. Discretisation of the kinematics of the lepton	54
7.2. Top quark polarisation within the patches	56
7.3. Minimisation for the definition of the discord	57
7.4. Migration matrices for the inclusive $\cos \theta_i^+ \cos \theta_i^-$	61
7.5. Unfolded Asimov-data for $\cos \theta_i^+ \cos \theta_i^-$ inclusively	61
7.6. Contributions to the total uncertainty of C_{xx} , C_{yy} and C_{zz} inclusively . . .	62
7.7. Impact of the nuisance parameters on C_{xx} , C_y and C_{zz} inclusively	62
7.8. Constraints for the nuisance parameters inclusively	63
7.9. Migration matrices for the inclusive $\cos \theta_i^+ \cos \theta_i^-$ with HERWIG	63
7.10. Unfolding distributions for PYTHIA and HERWIG	64
7.11. Number of expected events per patch	65
7.12. Migration matrices for $\cos \theta_i^+$ in a patch	66
7.13. Unfolded Asimov-data for $\cos \theta_i^+$ in a patch	66
7.14. Contributions to the total uncertainty of B_x^+ , B_y^+ and B_z^+ in a patch	67
7.15. Unfolding distributions for nominal and the twelfth variation of the PDFs .	67
B.1. Migration matrices for $\cos \theta_i^-$ in a patch	85
B.2. Unfolded Asimov-data for $\cos \theta_i^-$ in a patch	85
B.3. Contribution to the total uncertainty of B_x^- , B_y^- and B_z^-	86

1. Introduction

“I would not call that *one* but rather *the* characteristic trait of quantum mechanics”

- Erwin Schrödinger, one of the founders of quantum mechanics, 1935, talking about quantum entanglement [1]. At the same time, his colleague, Albert Einstein, derided it as "spukhafte Fernwirkung" (spooky action at distance) in a letter [2]. This academic dispute highlights the way quantum mechanics has fundamentally revolutionised the way we think about nature and physics. Specifically, quantum entanglement is one of the key elements of quantum mechanics that has polarised the scientific community.

So far, quantum entanglement has already been observed in photons [3], atoms [4], superconductors [5], mesons [6], neutrinos [7] and electrons [8]. Entanglement is not only a fundamental feature of quantum mechanics but also a key element for quantum teleportation, quantum information and quantum computation [9]. In 2022, the Nobel Prize in physics was awarded jointly to Alain Aspect, John Clauser and Anton Zeilinger "for experiments with entangled photons, establishing the violation of Bell inequalities and pioneering quantum information science" [10]. In 2023, the ATLAS collaboration observed entanglement in top quark pairs for the first time [11]. This has been the observation of quantum entanglement at the highest energy scale and the first one in "free" quarks. The measurement showed more entanglement than the simulations predicted, which has to be investigated with further measurements. In 2024, the CMS collaboration observed quantum entanglement as well in top quark pairs in both the dileptonic and semileptonic decay channel [12, 13]. The measurement in the dileptonic channel also hinted at a discrepancy between the simulation and data, which seemed to be resolved by including the hypothetical toponium particle in the simulation.

Measuring quantum entanglement in top quark pairs does not only test the Standard Model of particle physics but also tests fundamental quantum mechanical predictions at high energies [14, 15]. Besides quantum entanglement, a more general measure of the quantumness of the correlation can be studied, the quantum discord [16]. In contrast to

1. Introduction

entanglement, it can also be found in separable states that show non-classical behaviour. Quantum discord has experimentally been observed in nuclear-magnetic-resonance systems [17, 18] as well as optical systems [19, 20]. The tests of entanglement and discord are paving the way for future tests of quantum information theory of a two-qubit system at high-energy colliders such as the Large Hadron Collider (LHC).

This thesis presents the first sensitivity study for measuring quantum entanglement in top quark pairs in the semileptonic decay channel at the ATLAS experiment. Additionally, the first sensitivity study for measuring quantum discord in top quark pairs in the dileptonic decay channel at the ATLAS experiment is shown. The results pave the way for future measurements of quantum properties in top quark pairs at the ATLAS experiment. This leads to a better understanding of top quark properties and quantum mechanics at high energies.

In Chapter 2, the theoretical background for a study of entanglement and discord in top quark pairs is provided. The following Chapter 3 describes the experimental setup necessary for such a measurement: the Large Hadron Collider and the ATLAS experiment. Chapter 4 explains the modelling of the signal and background processes and the reconstruction of the relevant physics objects. An overview over systematic uncertainties is presented in Chapter 5. In Chapter 6, the sensitivity study of quantum entanglement in the semileptonic decay channel is presented, including the event reconstruction, analysis strategy and the results. The sensitivity study for quantum discord in the dileptonic decay channel is shown in Chapter 7. Finally, Chapter 8 provides an outlook for further developments of the measurements or related measurements.

2. Theoretical Background

Before performing any physics measurement, the theoretical predictions tested need to be understood. This chapter provides the theoretical background for measuring quantum entanglement and quantum discord in top quark pairs.

2.1. The Standard Model of Particle Physics

The Standard Model (SM) of particle physics is a quantum field theory describing the elementary particles and the fundamental interactions of the universe, the electroweak interaction [21–23] and the strong interaction [24–26] - yet missing the gravitational force. The underlying symmetries of the form of

$$SU(3)_C \times SU(2)_L \times U(1)_Y, \quad (2.1)$$

with the colour charge C , the left-handedness L , and the hypercharge Y . They allow, according to Noether's theorem [27], for fundamental conservation laws like the conservation of electric charge.

The particles described by the SM are displayed in Figure 2.1. There are three generations of spin-1/2 fermions, which can be classified as either quarks or leptons. These types of particles make up matter. Next to the fermions are the integer-spin bosons, of which the vector bosons (W^\pm , Z boson, gluon and photon) mediate the fundamental interactions. The scalar Higgs boson originates from the Brout-Englert-Higgs mechanism, which is responsible for giving mass to the particles [28, 29]. A boson comparable with the SM expectations for the Higgs boson has first been observed in 2012 by the ATLAS and CMS collaborations [30, 31]. All particles have an anti-particle with the same mass and spin but opposite physical charges.

To date, six quarks are predicted by the SM, and all of them have been discovered [32–36]. The last and most massive one, the top quark, was the last one to be discovered and will be further discussed in Chapter 2.2. The up-type quarks (u, c, t) have an electric charge

2. Theoretical Background

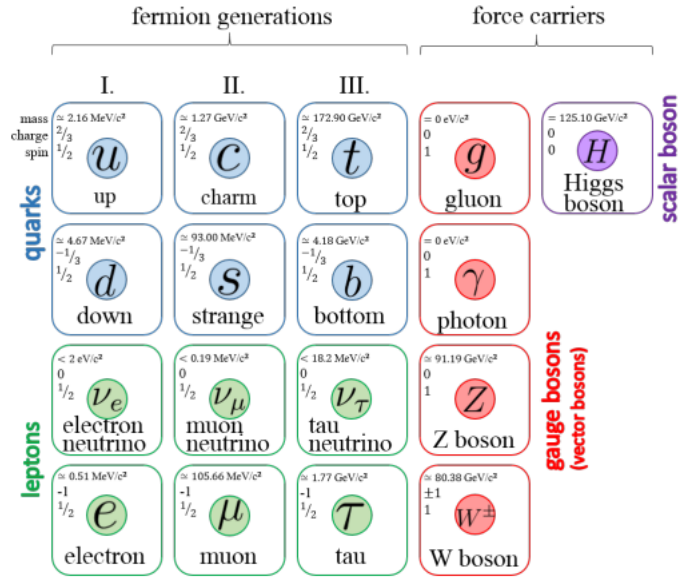


Figure 2.1.: Overview of the elementary particles of the Standard Model.

of $Q = +2/3e$ and a third component of isospin of $I_3 = +1/2$, while the down-type quarks have an electric charge of $Q = -1/3e$ and a third component of isospin of $I_3 = -1/2$. Characteristically, quarks carry colour charge and, therefore, interact via the strong interaction. Due to the nature of the colour confinement, they can form bound states, called hadrons. Most commonly, quarks form states of three quarks or anti-quarks (baryons) or one quark and one anti-quark (mesons), which also ensures an integer value of electric charge.

The leptons can also be sorted into up-type and down-type according to the isospin. The up-type leptons with $I_3 = +1/2$ are the neutrinos, which are electrically neutral and predicted to be massless by the SM. The down type leptons with $I_3 = -1/2$ are the charged leptons (e, μ, τ) with an electric charge of $Q = -e$ and an ascending order of masses.

The strong interaction is described by quantum chromodynamics (QCD) and based on the colour charge. There are three different values for the colour charge: red (r), blue (b) and green (g) with their corresponding anti-colours: anti-red (\bar{r}), anti-blue (\bar{b}) and anti-green (\bar{g}). The underlying symmetry of QCD is the $SU(3)$ group, which has eight generators corresponding to a colour octet of gluons. Gluons always carry a colour and an anti-colour to conserve colour charge. Because the $SU(3)$ group is a non-Abelian group, the gluons have self-interactions, and the coupling strength of the strong interaction, α_s , increases with the distance between two colour-charged objects. Consequently, quarks can never be separated because the energy stored increases with the distance between

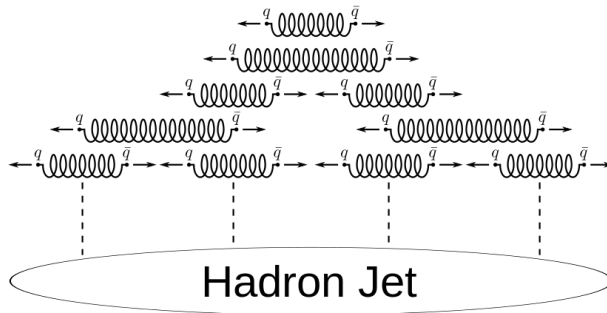


Figure 2.2.: Scheme of confined quarks that move away from each other. The energy of the potential between the two quarks becomes larger with the distance between them until a new pair of quarks is created.

the quarks, similar to an elongated rubber band. When the energy is large enough to create a new pair of quark and anti-quark, it is produced out of the vacuum. Then, both quarks are again in bound states with the newly produced quarks. This process of building bound states is called hadronisation. When quarks are created with high energies originating from collisions at the LHC, they move apart with high momenta, constantly creating new pairs of quarks. This avalanche of hadrons is called a jet. In simulations, there are different approaches to modelling the hadronisation process. One approach, the Lund-string model [37, 38], is shown schematically in Figure 2.2. This model is used in the PYTHIA generator [39]. An alternative model, the cluster model [40, 41] is implemented in HERWIG [42, 43].

The fermions of the SM can be sorted into right-handed chiral singlets, χ_R , and left-handed chiral doublets, χ_L , according to their weak isospin, I_3 , with chirality being defined by the chirality operator $P_{L/R} = \frac{1 \mp \gamma^5}{2}$. The vertex factor of the weak charged current, mediated by W^\pm , is

$$\frac{-ig_W}{\sqrt{2}} \frac{1}{2} \gamma^\mu (1 - \gamma^5) \quad (2.2)$$

which means that the weak charged current only acts on left-handed particles and right-handed anti-particles. Because of this vector-axialvector structure (V-A), the charged current weak interaction is maximally parity violating.

For quarks, the mass eigenstates of the quarks d, s, b do not coincide with their weak eigenstates d', s', b' . Instead, the weak eigenstates are a mixture of the mass eigenstates of the quarks, described by the Cabibbo-Kobabyashi-Maskawa (CKM) matrix, V_{CKM} [44, 45].

The underlying symmetry of the charged current interaction is the $SU(2)$ symmetry group with three generators, W_μ^k . The physical W bosons are a linear combination of W_μ^1 and

2. Theoretical Background

W_μ^2

$$W_\mu^\pm = \frac{1}{\sqrt{2}} \left(W_\mu^{(1)} \mp iW_\mu^{(2)} \right). \quad (2.3)$$

In the unified electroweak model, the two neutral bosons, the photon A_μ and the Z boson, are written as a linear combination of the $U(1)$ B_μ field and $W_\mu^{(3)}$

$$A_\mu = +B_\mu \cos \theta_W + W_\mu^{(3)} \sin \theta_W, \quad (2.4)$$

$$Z_\mu = -B_\mu \sin \theta_W + W_\mu^{(3)} \cos \theta_W, \quad (2.5)$$

with the weak mixing angle, θ_W .

2.2. Physics of the Top Quark

The top quark is the most massive of the elementary particles in the Standard Model. It was predicted by Makoto Kobayashi and Toshihide Maskawa in 1973 when they introduced a third generation of quarks to explain the already observed CP -violation [45]. Its weak isospin partner, the bottom quark, was already discovered in 1977 [34]. Due to the large mass of the top quark, it took until 1995 for it to be observed by the CDF and DØ collaborations at the TEVATRON [35, 36]. The current world average for the mass of the top quark is

$$m_t = 172.69 \pm 0.30 \text{ GeV} \quad (2.6)$$

via direct measurements [46] which is roughly the mass of a whole gold atom [47].

Due to its large mass, it not only has the largest Yukawa coupling to the Higgs field (in the order of 1) but also has the shortest lifetime of $\tau \approx 5 \cdot 10^{-25}$ s [46]. In contrast, the time for quarks to hadronise is in the order of $\tau_{\text{had}} \approx 10^{-23}$ s [48] which means that the top quark decays before it hadronises. Similarly, the timescale for spin decorrelation is $\tau_{\text{deco}} \approx 10^{-21}$ s [49] such that the top quark transfers its spin properties directly to its decay products. This property can be used for measurements of classical and quantum spin correlations. Despite the short lifetime of the top quark, pseudo-bound states of top quark and anti-top quark, so-called toponium states, are predicted to form near the production threshold [50–54]. Toponium has not been observed yet but it is predicted to be a spin-singlet, which could enhance the level of quantum entanglement near the top quark pair production threshold.

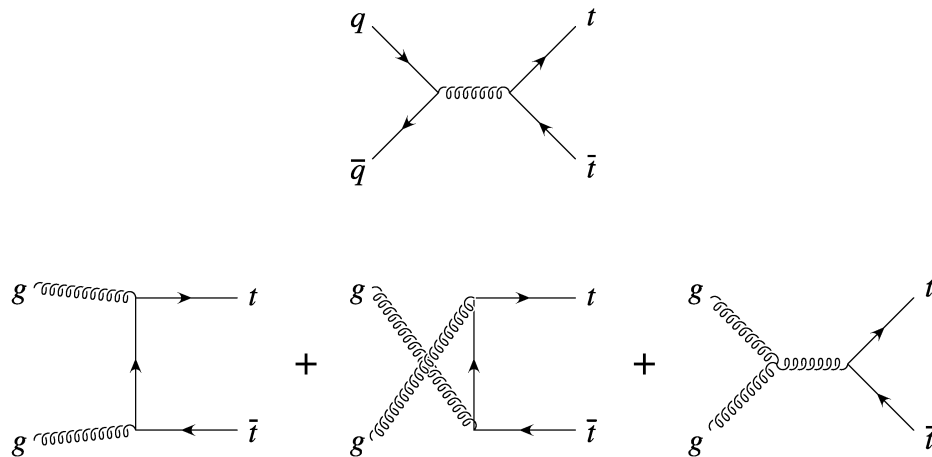


Figure 2.3.: Feynman diagrams of the leading order processes for top quark pair production at the LHC.

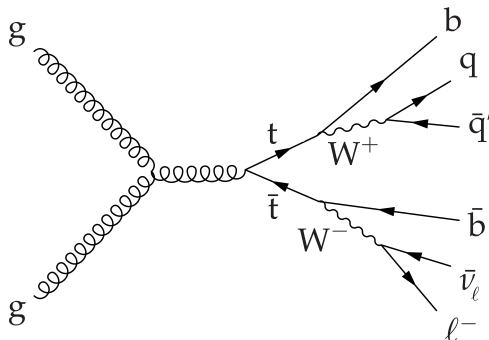


Figure 2.4.: Feynman diagram of the semileptonic decay of a top quark pair.

In the proton-proton collisions at the LHC (see Chapter 3), top quarks are most likely produced in top-anti-top quark pairs. The leading order processes for top quark pair production are shown in Figure 2.3. Due to the parton density functions of the proton, the process with gluons in the initial state (ggF) dominates at the energies of the LHC. Top quarks decay almost exclusively to bottom quarks and a W boson since the CKM matrix element is close to unity $V_{tb} \approx 1$ [46]. The W boson can decay both hadronically ($\text{BR}(W \rightarrow q\bar{q}) \approx 2/3$) and leptonically ($\text{BR}(W \rightarrow l^+l^-) \approx 1/3$) [46]. While the leptonic decay has a smaller branching ratio and consequently lower statistics, it provides a better separation from the background experimentally. The semileptonic decay channel of the $t\bar{t}$ pair as shown in Figure 2.4 where one W boson from one top quark decays leptonically and the other one hadronically therefore provides a suitable choice for analyses because of its mixture of high branching ratio and low background contributions.

The degree to which the spin information from the top quark is being transferred to

2. Theoretical Background

Table 2.1.: Standard Model predictions of the spin analysing power at LO and NLO for the decay products of the top quark. The corresponding decay products of the anti-top quark have a reversed sign [55–58].

	b quark	W	l	d/s quark	u/d quark
$\alpha_i(\text{LO})$	−0.41	0.41	1	1	−0.31
$\alpha_i(\text{NLO})$	−0.39	0.39	0.998	0.97	−0.32

the decay product is called the spin analysing power, α . The spin analysing power is determined by the weak interaction and its parity violating $V - A$ structure. In Table 2.1, the numerical values at LO and NLO in QCD are shown for the different top quark decay products. Two spin analysers, one from each top quark decay, are needed to construct spin-sensitive observables. Both the charged lepton and the light down-type quark have a high spin analysing power of $|1|$ due to the $V - A$ structure of the weak interaction, as further described in [56, 57]. In contrast, the b quark coming directly from the top quark has a lower spin analysing power of -0.41 . This can be understood by looking at the rest frame of the top quark: the spin orientation of the b quark depends on the helicity of the W boson. If the W is longitudinally polarised, the spins of the b and top quarks are parallel, while for a left-handed polarised W boson, they are antiparallel. Alternatively, a different hadronic spin analyser, called the "optimal hadronic polarimeter", q_{opt} , can be constructed [59, 60]. The optimal hadronic polarimeter q_{opt} is a helicity weighted average of the two jets of the hadronic W boson and can be used to avoid the identification of the down-type jet explicitly. It has a spin analysing power $\alpha_{q_{\text{opt}}} \approx 0.64$. The experimental feasibility of the different hadronic spin analysers has been studied in Chapter 6.3 for the sensitivity to quantum entanglement in the semileptonic decay channel.

The spin density matrix of the $t\bar{t}$ system ρ can be written as

$$\rho = \frac{1}{4} \left(\mathbb{1}_4 + \sum_{i=1}^3 (B_i^+ \sigma^i \otimes \mathbb{1}_2 + B_i^- \mathbb{1}_2 \otimes \sigma^i) + \sum_{i,j=1}^3 C_{ij} \sigma^i \otimes \sigma^j \right) \quad (2.7)$$

with the spin correlation matrix C_{ij} , and individual spin polarisations B_i^+ (for the top quark) and B_i^- (for the anti-top quark) [61]. To access the spin polarisations, B_i^\pm , the differential distribution of $\cos \theta_i^\pm$ can be used

$$\frac{1}{\sigma} \frac{d\sigma}{d \cos \theta_i^\pm} = \frac{1}{2} (1 + \alpha^\pm \cdot B_i^\pm \cos \theta_i^\pm), \quad i = \{1, 2, 3\}, \quad (2.8)$$

with the spin analysing power α and the angle between the spin analyser θ and the

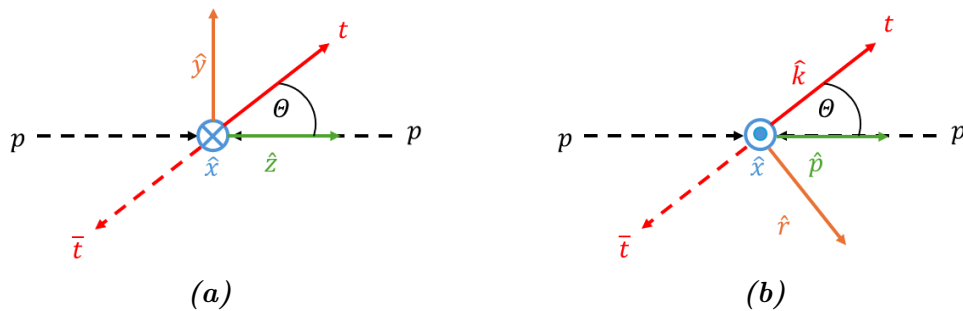


Figure 2.5.: Illustration of the spin bases, **a)** helicity, **b)** beam basis.

respective spin quantisation axis in the rest frame of the respective top quark. This relation can be used to calculate the polarisation via the mean of the distributions

$$B_i^\pm = \alpha^\pm \cdot 3 \cdot \langle \cos \theta_i^\pm \rangle. \quad (2.9)$$

The spin correlation coefficients can similarly be obtained via the differential distributions of the product of the $\cos \theta$ distributions

$$\frac{1}{\sigma} \frac{d\sigma}{d \cos \theta_i^+ \cos \theta_i^-} = \frac{1}{2} \left(1 + \alpha^\pm \alpha^\mp C_{ii} \cos \theta_i^+ \cos \theta_i^- \right) \ln \left(\frac{1}{|\cos \theta_i^+ \cos \theta_i^-|} \right). \quad (2.10)$$

Again, the coefficients can equivalently be extracted via the mean of the distribution

$$C_{ij} = \alpha^\pm \alpha^\mp \cdot 9 \cdot \langle \cos \theta_i^\pm \cos \theta_j^\mp \rangle. \quad (2.11)$$

The spin correlation coefficients are described by

$$C_{ij} = \frac{\uparrow\uparrow + \downarrow\downarrow - \uparrow\downarrow - \downarrow\uparrow}{\uparrow\uparrow + \downarrow\downarrow + \uparrow\downarrow + \downarrow\uparrow} \quad (2.12)$$

depending on the cross-sections for producing top quark pairs where the top quark has spin up (\uparrow) or down (\downarrow) with respect to the top spin axis i , and equivalently for the anti-top quark and the spin axis j . The trace of the spin correlation matrix is used for the entanglement criterion as described in Chapter 2.3.1. For the calculation of discord, the whole spin density matrix needs to be constructed, as described in 2.3.2. The value for the spin correlation depends on the choice of the spin basis. One useful choice is the beam basis illustrated in Figure 2.5a. As the name indicates, the beam basis is defined with respect to the beam directions in the lab frame. The z axis is defined along the beam line and the x and y directions are constructed orthogonally. Another spin basis is the helicity basis, shown in Figure 2.5b. In this basis, the direction of flight of the top

2. Theoretical Background

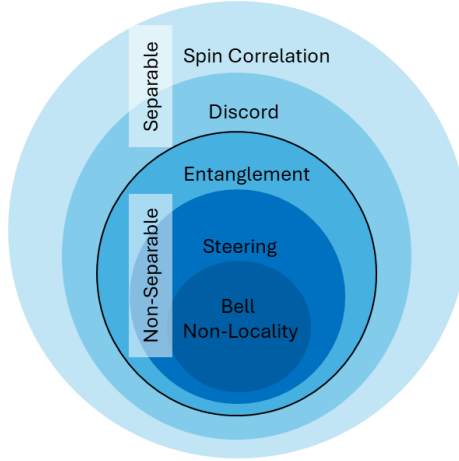


Figure 2.6.: Scheme of the hierarchy of correlations in a $t\bar{t}$ system: spin correlation, quantum discord, quantum entanglement, quantum steering and Bell non-locality. The border between separable and non-separable correlations is shown.

quark in the centre-of-mass frame is taken as the spin quantisation axis.

2.3. Quantum Correlations

Two-qubit systems can display multiple kinds of correlation, ranging from purely classical correlations over quantum discord, quantum entanglement, and quantum steering to Bell non-locality [62]. Quantum steering describes the phenomenon of influencing one qubit in a non-separable correlation by manipulating the other one [1, 63]. Bell non-locality describes a correlation which exhibits a quantum correlation that cannot be explained by a local hidden variable theory [64]. The hierarchy regarding the strictness of the correlations is shown in Figure 2.6. The $t\bar{t}$ spin system is a well-suited two-qubit system to explore these kinds of correlations because the top quark passes its spin properties directly to its decay products, and hundreds of million $t\bar{t}$ events were already recorded at ATLAS. This provides ample statistics to study subtle effects. In the following, the concepts of quantum entanglement and quantum discord are covered in detail, and applications to the top quark pair production are discussed.

2.3.1. Quantum Entanglement

In 1935, Erwin Schrödinger coined the term "entanglement" [1] for a quantum mechanical phenomenon of a pair of objects prepared in a particular way. An entangled quantum state is an inseparable whole and cannot be factored as a product of the states of its

constituents. One constituent cannot be described without knowledge about the other one. In a bipartite Hilbert space, \mathcal{H} , consisting of the two subsystems A and B , a composite quantum state, ρ , is separable if and only if it can be factorised into the states of the subsystems, ρ_n^A and ρ_n^B , with coefficients p_n

$$\rho = \sum_n p_n \rho_n^A \otimes \rho_n^B, \quad \sum_n p_n = 1, \quad p_n \geq 0 \quad \forall n, \quad (2.13)$$

which is a purely quantum mechanical feature.

The necessary condition for a joint density matrix, ρ , of the two quantum mechanical systems A and B to be separable is the Peres-Horodecki criterion [65, 66]. It states that the general state, ρ , acting on $\mathcal{H}_A \otimes \mathcal{H}_B$

$$\rho = \sum_{ijkl} p_{ijkl}^ij |i\rangle\langle j| \otimes |k\rangle\langle l|, \quad (2.14)$$

is separable if the eigenvalues of the partial transpose with respect to one of the parties

$$\rho^{T_B} := (\mathbb{1} \otimes T)(\rho) = \sum_{ijkl} p_{ik}^{ij} |i\rangle\langle j| \otimes |k\rangle\langle l|, \quad (2.15)$$

are all non-negative. Consequently, ρ is entangled if ρ^{T_B} has a negative eigenvalue. Applying the Peres-Horodecki criterion on the separable state shown in Equation (2.13), yields

$$\rho^{T_B} = \sum_n p_n \rho_n^A \otimes (\rho_n^B)^T. \quad (2.16)$$

Since the transposition preserves the eigenvalues, $(\rho_n^B)^T$ must still be positive semidefinite and all the eigenvalues are non-negative. Intuitively, it can be understood that the quantum state is separable if the transposition is applied to only one subsystem of the state and the state still is a physical quantum state (by having a positive semidefinite density matrix). For an entangled state, the subsystems cannot be treated individually and the transposition of one subsystem results in an unphysical state with negative eigenvalues.

A quantitative measurement of the degree of entanglement is described by the concurrence $C[\rho]$ [67], which is defined as

$$C[\rho] \equiv \max(0, \lambda_1 - \lambda_2 - \lambda_3 - \lambda_4) \quad (2.17)$$

2. Theoretical Background

with λ_i the eigenvalues in decreasing order of magnitude of the matrix $\mathcal{C}(\rho) = \sqrt{\sqrt{\rho}\tilde{\rho}\sqrt{\rho}}$ with the spin-flipped state $\tilde{\rho} = (\sigma_2 \otimes \sigma_2)\rho^*(\sigma_2 \otimes \sigma_2)$. The concurrence takes a value between 0 and 1 for an entangled state, where a concurrence of 1 means maximally entangled. This can be understood by looking at the more general definition of the concurrence

$$C(\psi) = |\langle\psi|\tilde{\psi}\rangle| \quad (2.18)$$

with $\tilde{\psi}$ the spin flipped state $|\tilde{\psi}\rangle = \sigma_2|\psi^*\rangle$ using the complex conjugate ψ^* . For the four maximally entangled Bell states, the spin-flipped state $\tilde{\psi} = \pm\psi$, which results in the concurrence of 1. In case of a separable state, they are orthogonal to each other, $\tilde{\psi} \perp \psi$, resulting in a concurrence of 0 [67].

The simplest model of a pair of quantum systems is a pair of qubits, where a qubit is a two-level quantum system, e.g. a spin-1/2 particle. The spin density matrix, ρ , of this state is given by Equation (2.7). Applying the Peres-Horodecki criterion to this state yields an entanglement criterion of

$$\Delta \equiv \text{tr}[C] - 1 > 0, \quad (2.19)$$

with the concurrence given by

$$C[\rho] = \frac{\max(0, \Delta)}{2} \quad (2.20)$$

as shown in [61].

Quantum Entanglement in Top Quark Pairs

The spin of the top quark is predicted to be 1/2 as for the other elementary fermions. Classical spin correlations between a top and an anti-top quark have already been theoretically described [68–72] and experimentally measured by the DØ [73–76] and CDF [77] collaboration at the TEVATRON and by the ATLAS [78–83] and CMS [84–87] collaboration at the LHC, but the connection between the top spin correlation and entanglement has only recently been discussed in [61].

The spin orientations of the top quarks are determined by the production process. As described in the previous section, a top quark pair can originate from a quark anti-quark pair ($q\bar{q}$) or a gluon pair (gg). In Figure 2.7, the concurrence of the spin density matrix $\rho(M_{t\bar{t}}, \hat{k})$ as a function of the invariant mass $M_{t\bar{t}}$, and the production angle Θ , is shown for both the production modes. The invariant mass is defined as $M_{t\bar{t}}^2 \equiv (k_t + k_{\bar{t}})^2$ with k

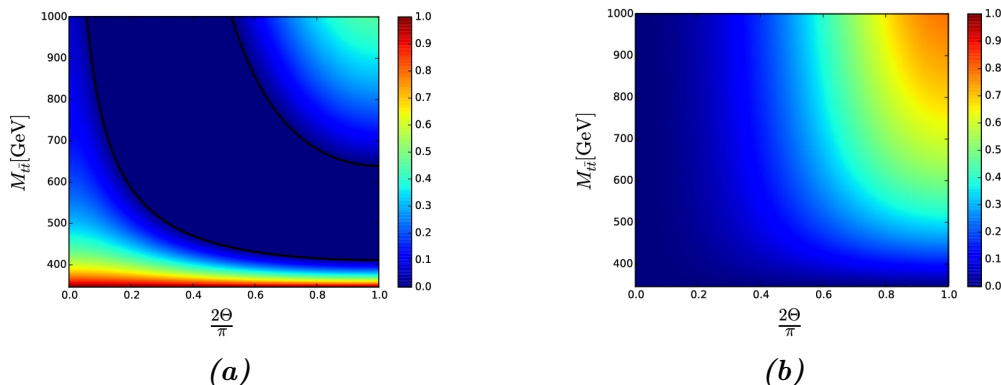


Figure 2.7.: Measure of Entanglement as a function of the invariant mass, $M_{t\bar{t}}$, and the production angle, Θ , in the $t\bar{t}$ CM frame [61] for **a)** $gg \rightarrow t\bar{t}$, **b)** $q\bar{q} \rightarrow t\bar{t}$.



Figure 2.8.: Spin configurations at production threshold for **a)** $gg \rightarrow t\bar{t}$, **b)** $q\bar{q} \rightarrow t\bar{t}$.

being the momentum vector.

The presence of entanglement in the lower region of Figure 2.7a can be explained from the nature of the $t\bar{t}$ production through gluon fusion. In the spin-singlet state

$$\rho^{gg}(2m_t, \hat{k}) = |\psi_0\rangle\langle\psi_0|, \quad |\psi_0\rangle = \frac{|\uparrow_{\hat{n}}\downarrow_{\hat{n}}\rangle - |\downarrow_{\hat{n}}\uparrow_{\hat{n}}\rangle}{\sqrt{2}}, \quad (2.21)$$

with $|\uparrow_{\hat{n}}\rangle, |\downarrow_{\hat{n}}\rangle$ the spin eigenstates along the direction \hat{n} , the spin polarisations of the initial state gluon pair point in different directions [61], as can be seen in Figure 2.8a. The spin-singlet is maximally entangled, as is the spin-triplet state. In general, the top quark pairs are produced as a mixture of those states and other states which are less or not entangled at all, which makes detection difficult. The spin-singlet specifically is the lowest energy state possible, which means that the fraction of maximally entangled top quark pairs is enhanced in the low energy regime at the production threshold ($M_{t\bar{t}} = 2m_t$). Because of this, the production threshold region is feasible for studies of entanglement. This can also be seen in the lower region of Figure 2.7a. At high energies and large production angles (upper right corner of Figure 2.7a), the $t\bar{t}$ pair is produced in an also

2. Theoretical Background

maximally entangled spin triplet state

$$\rho^{gg}(\infty, \hat{k}) = |\psi_\infty\rangle\langle\psi_\infty|, \quad |\psi_\infty\rangle = \frac{|\uparrow_{\hat{n}}\downarrow_{\hat{n}}\rangle + |\downarrow_{\hat{n}}\uparrow_{\hat{n}}\rangle}{\sqrt{2}}. \quad (2.22)$$

In contrast, for the $q\bar{q}$ induced $t\bar{t}$ production, the $t\bar{t}$ pairs are not produced in an entangled state at the production threshold, as can be seen in Figure 2.7b. In the limit of high energies and production angles, the quantum state converges to the same one independent of the initial state due to the dominance of the orbital angular momentum over the spin [61]. Only the entanglement scenario at the production threshold is studied in this work. The measurement of quantum entanglement in top quark pairs can be used to search for new physics scenarios, as shown in [14].

Experimentally, the marker

$$D = \frac{\text{tr}[\mathbf{C}]}{3} = -\frac{1 + \Delta}{3} \quad (2.23)$$

is measurable and relates to the entanglement criterion described in Equation (2.19) which transforms to

$$D < -\frac{1}{3}. \quad (2.24)$$

D can be extracted from the differential cross-section of the angular separation of the spin analysers of the top quarks

$$\frac{1}{\sigma} \frac{d\sigma}{d \cos \varphi} = \frac{1}{2}(1 - \alpha_i \alpha_j D \cos \varphi) \quad (2.25)$$

where φ is the angle between the spin analysers in the rest frame of their respective top quark and $\alpha_{i/j}$ the spin analysing power of the decay products [61]. Since the entanglement is studied in the semileptonic decay channel, $\alpha_i = \alpha_l$ is set to 1 in the following, since only the charged lepton is considered as the leptonic spin analyser and $\alpha_j = \alpha_h$ remains flexible as the hadronic spin analysing power. The D coefficient can be extracted from the $\cos \varphi$ distribution using either a linear fit or the average of the distribution

$$\langle \cos \varphi \rangle = \int_{-1}^1 \cos \varphi \frac{1}{\sigma} \frac{d\sigma}{d \cos \varphi} d \cos \varphi = \int_{-1}^1 \cos \varphi \frac{1}{2}(1 - \alpha_h D \cos \varphi) d \cos \varphi = -\frac{\alpha_h D}{3} \quad (2.26)$$

resulting in $D = -3\langle \cos \varphi \rangle / \alpha_h$. The CMS collaboration has already measured the D coefficient for spin correlations precisely in the full $M_{t\bar{t}}$ phase space, resulting in $D = -0.237 \pm 0.011$ [87]. The $\cos \varphi$ distribution is consequently already well-known.

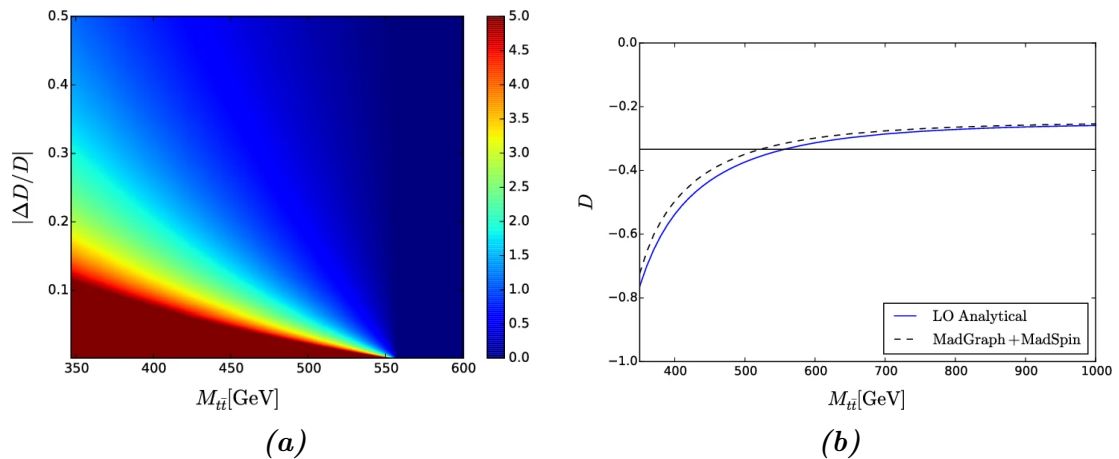


Figure 2.9.: **a)** Statistical deviation from the null hypothesis ($D \geq -1/3$) for different assumptions of relative uncertainty on D . **b)** The value of D within $[2m_t, 1000 \text{ GeV}]$ as upper threshold on $M_{t\bar{t}}$ for analytical and numerical calculations [61].

In Figure 2.9a, the statistical deviation from the null hypothesis ($D \geq -1/3$)

$$n_{\Delta} \equiv \max \left[\frac{D + 1/3}{\Delta D}, 0 \right] \quad (2.27)$$

as a function of the selection on the invariant mass, $M_{t\bar{t}}$, and the relative uncertainty, $|\Delta D/D|$, with D the expected value and ΔD the uncertainty, is shown. In the lower left corner, the significance exceeds the 5σ threshold, allowing for an observation of entanglement. In Figure 2.9b, the theoretical calculations of D as a function of $M_{t\bar{t}}$ are shown, stressing the relevance of an upper limit on $M_{t\bar{t}}$ in order to measure the entangled system. For high limits on $M_{t\bar{t}}$, the convergence to a non-entangled value of D , as observed by CMS [87], can be seen.

2.3.2. Quantum Discord

The original paper about quantum discord is called "A Measure of the Quantumness of Correlations" [16]. Quantum discord describes the difference of two classically identical expressions for the mutual information that is non-zero for quantum systems. By this, quantum discord quantifies the degree of quantumness in a correlation. Quantum discord can also be found in separable states, which means that non-separability is not necessary for general quantum behaviour but for quantum entanglement specifically.

In information theory, the mutual information of two random variables, A , B , measures

2. Theoretical Background

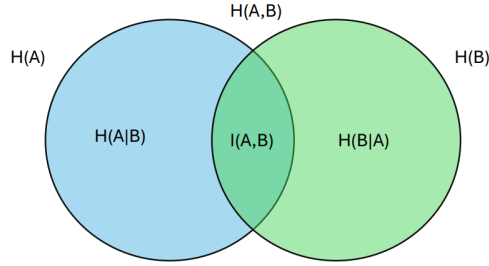


Figure 2.10.: Venn diagram illustrating the relationship between the conditional entropy ($H(A|B)$ and $H(B|A)$) and the mutual information ($I(A; B)$) in classical information theory

the mutual dependence between the two variables or more precise, quantifies how much about one variable can be learned by measuring the other one. In the classical theory, it can equivalently be expressed by both

$$I(A; B) = H(A) + H(B) - H(A, B) \quad (2.28)$$

and

$$J(A; B) = H(A) - H(A|B), \quad (2.29)$$

with $H(A)$ being the information entropy, $H(A, B)$ being the joint entropy and $H(A|B)$ being the conditional entropy [88]. The relations are illustrated in Figure 2.10. When transferring the classical information theory to the quantum information theory, $H(A)$ becomes $S(\rho_A)$, the Von Neumann entropy of the probability density function ρ_A , $H(A, B)$ becomes the joint quantum entropy $S(\rho)$ for the joint probability density function ρ , and $H(A|B)$ becomes $S(\rho_A|\rho_B)$ the generalised conditional entropy. Then, the expressions for the mutual information can be written as

$$I(\rho) = S(\rho_A) + S(\rho_B) - S(\rho), \quad (2.30)$$

$$J_A(\rho) = S(\rho_B) - S(\rho_B|\rho_A) \quad (2.31)$$

which are not equivalent any more. The difference between the two expressions is called the quantum discord,

$$\mathcal{D}_A(\rho) = I(\rho) - J_A(\rho), \quad (2.32)$$

which can be asymmetric with respect to an exchange of A and B . For the discord to be completely basis independent, J has to be maximised over the set of all possible

measurements [16]

$$D_A(\rho) = I(\rho) - \max_{\{\prod_j^A\}} J_{\{\prod_j^A\}}(\rho) = S(\rho_A) - S(\rho) + \min_{\{\prod_j^A\}} S\left(\rho_{B|\{\prod_j^A\}}\right). \quad (2.33)$$

The presence of discord shows the quantumness of the correlation and the non-commutativity of the quantum operators.

The density matrix of a two-qubit state, ρ , with subsystems A and B , like the $t\bar{t}$ system, is given by Equation (2.7). The quantum discord of the subsystem A is then given by

$$\mathcal{D}_A = S(\rho_B) - S(\rho) + \min_{\hat{n}} [p_{\hat{n}} S(\rho_{\hat{n}}) + p_{-\hat{n}} S(\rho_{-\hat{n}})], \quad (2.34)$$

with $\rho_{A,B} = \text{Tr}_{B,A}\rho$ being the reduced quantum states in A, B respectively and $S(\rho) = -\text{Tr}\rho \log_2 \rho$ the Von Neumann entropy [62]. $\rho_{\pm\hat{n}}$ describes the conditional quantum state of the qubit in A after the one in B has been measured in the state $|\pm\hat{n}\rangle$ with the probability of doing so given by $p_{\pm\hat{n}}$,

$$\rho_{\hat{n}} = \frac{\mathbb{1} + B_{\hat{n}}^+ \cdot \vec{\sigma}}{2}, \quad B_{\hat{n}}^+ = \frac{B^+ + C \cdot \hat{n}}{1 + \hat{n} \cdot B^-}, \quad p_{\hat{n}} = \frac{1 + \hat{n} \cdot B^-}{2}. \quad (2.35)$$

The minimisation in Equation (2.34) is performed over the Bloch sphere of the qubit in B , which is a geometric representation of the state of a qubit [89]. The minimisation means choosing the measurement that least disturbs the overall quantum state while still providing information about it [16]. Equivalent relations hold for the discord in subsystem B , but A is exchanged for B , B^+ for B^- and C for C^T . The uncertainty propagation for this calculation can be found in Appendix A.

As Equation 2.34 shows, no closed analytical form for the discord exists for a general quantum state. But a closed form can be determined for quantum states diagonal in the Bell basis, the so-called Bell-diagonal states. The two-qubit state is a Bell-diagonal state in case of zero polarisations and a diagonal spin correlation matrix, C_{ij} , which results in the spin density matrix of

$$\rho = \frac{1}{4} \left(\mathbb{1} + \sum_{i=1}^3 C_{ii} \sigma_i \otimes \sigma_i \right). \quad (2.36)$$

For these states, the discord can be calculated as [90]

$$\mathcal{D}_A = \mathcal{D}_B = 2 + \sum_{i=1}^4 \lambda_i \log_2 \lambda_i - \frac{1-C}{2} \log_2(1-C) - \frac{1+C}{2} \log_2(1+C) \quad (2.37)$$

2. Theoretical Background

with $C = \max\{|C_{11}|, |C_{22}|, |C_{33}|\}$ and λ_i defined by

$$\lambda_1 = (1 - C_{11} - C_{22} - C_{33})/4, \quad \lambda_2 = (1 - C_{11} + C_{22} + C_{33})/4, \quad (2.38)$$

$$\lambda_3 = (1 + C_{11} - C_{22} + C_{33})/4, \quad \lambda_4 = (1 + C_{11} + C_{22} - C_{33})/4. \quad (2.39)$$

Quantum Discord in Top Quark Pairs

Quantum discord is an interesting addition to the study of quantum entanglement in top quark pairs because quantum discord is separately defined for the top and anti-top quark, whereas quantum entanglement regards the system as a whole. This property can be used to search for CP -violation and new physics.

Similarly to quantum entanglement, quantum discord depends on the production mode of the top quark pair. In Figure 2.11, the discord of the top quark is shown as a function of $\beta = \sqrt{1 - 4m_t^2/M_{t\bar{t}}}$ and the production angle θ in the $t\bar{t}$ centre-of-mass frame for the two leading order (LO) production processes, similar to Figure 2.7. At leading order, the top and anti-top quark discord are predicted to be symmetric. Higher-order corrections can lead to an asymmetry.

Quantum discord can be studied best in top quarks if the spin correlation matrix is taken in the beam basis. Then, the spin correlation matrix becomes diagonal with $C_{xx} = C_{yy} = C_{\perp}$ and $C_{zz} = C_z$, which is one of the criteria for the Bell-diagonal states which have a simplified calculation of quantum discord. The second criterion of no individual spin polarisation is only true for a leading order production of top quarks and can not be generally assumed. For a simplified picture of the discord, this assumption can be used to obtain an estimation. In Figure 2.12, quantum discord calculated via the simplified assumption is displayed as a function of only C_{\perp} and C_z . The dashed white line marks the classical states with $C_{\perp} = 0$, and the solid red line shows the critical boundary of separability. The green line shows the MC prediction for $t\bar{t}$ systems at the LHC at $\sqrt{s} = 13$ TeV for $\beta \leq 1$ (circle) and $\beta \leq 0.1$ (cross). The figure is reproduced with ATLAS MC simulation after the example from [62].

Large statistics of recorded top quark pairs at the ATLAS experiment allow us to perform the minimisation after Equation (2.34) without simplification. However, the direction \hat{n} cannot continuously be defined, instead discrete ensembles of events (patches) have to be defined. A detailed discussion of the experimental considerations can be found in Chapter 7.

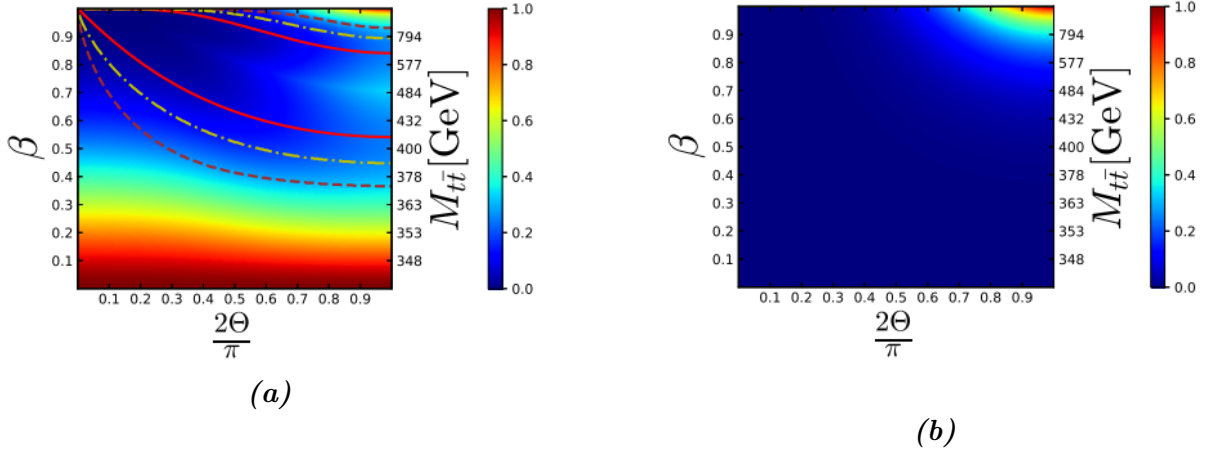


Figure 2.11.: Quantum discord of the spin density matrix as a function of the top velocity β and the production angle θ in the $t\bar{t}$ centre-of-mass frame for **a)** $gg \rightarrow t\bar{t}$, **b)** $q\bar{q} \rightarrow t\bar{t}$. Solid red, dashed-dotted yellow and dashed brown are the critical boundaries of separability, steerability and Bell locality, respectively [62].

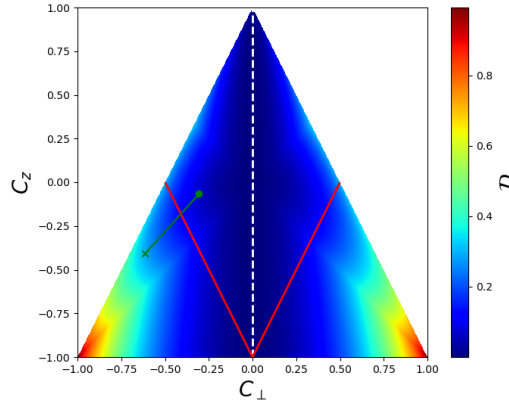


Figure 2.12.: Quantum discord as a general function of C_{\perp} and C_z . The dashed white line marks the classical states with $C_{\perp} = 0$, and the solid red line shows the critical boundary of separability. The green line shows the MC prediction for $t\bar{t}$ systems at LHC at $\sqrt{s} = 13$ TeV for $\beta \leq 1$ (circle) and $\beta \leq 0.1$ (cross). Reproduced with ATLAS simulation after the example of [62].

3. Experimental Setup

The physics simulations used in this thesis are based on the experimental setup of the ATLAS experiment at the Large Hadron Collider, as presented in this chapter. This allows for an actual measurement using data later.

3.1. The Large Hadron Collider

The LHC (Large Hadron Collider) [91] is a particle collider located at CERN (Conseil Européen pour la Recherche Nucléaire) near Geneva, Switzerland. It is a synchrotron with a circumference of 27 km operating using either protons or heavy ions. For this thesis, the proton-proton collisions are used. Its design centre-of-mass energy for proton-proton collisions is $\sqrt{s} = 14$ TeV. Up to today, the highest centre-of-mass energy recorded was 13.6 TeV in Run 3. The LHC started operation in 2008 with the first stable beams. Since then, there have been three data taking periods: Run I from 2010 to 2013 with $\sqrt{s} = 7(8)$ TeV, Run 2 from 2015 to 2018 with $\sqrt{s} = 13$ TeV and Run 3 since 2022 with $\sqrt{s} = 13.6$ TeV.

At four points around the accelerator the particles can collide and the collision event is recorded using one of the detectors: ATLAS [92], ALICE [93], CMS [94] or LHCb [95]. The detectors are built independently using different technologies to ensure the independence of the results. ATLAS and CMS are multipurpose experiments with the goal of precision measurement of Standard Model processes and searches for Beyond the Standard Model physics. LHCb focuses on the physics of B -hadrons and CP -violation, and ALICE is specialised in heavy-ion physics and the research of the quark-gluon plasma.

3. Experimental Setup

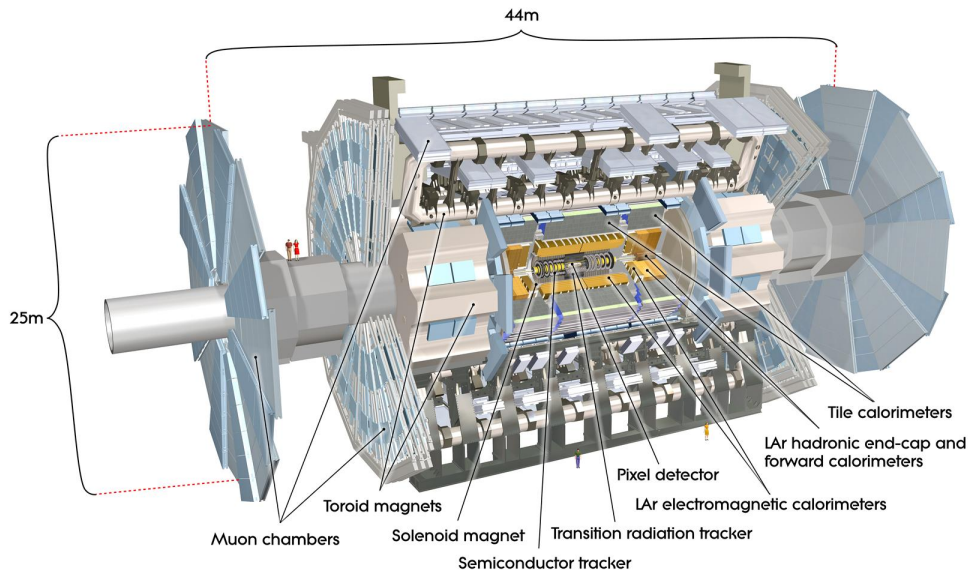


Figure 3.1.: Overview of the ATLAS detector with subdetectors ©CERN.

3.2. The ATLAS Experiment

The ATLAS detector is, with a length of 44 m, a diameter of 25 m and a weight of 7000 t, the largest particle detector at an accelerator ever built. In Figure 3.1, an overview of ATLAS as of Run 2 is shown. ATLAS is designed with multiple layers of subdetectors since there is no single detector design that can provide complete information on all kinds of particles. In Figure 3.2, a cross-section of ATLAS with its layers is shown and the signatures of muons, electrons, photons, neutrons and protons are drawn in. Neutrinos leave the detector without interaction. Other particles are not long-lived enough to reach the detector and can only be measured via their decay products.

The Inner Detector

The Inner Detector is the innermost part of the ATLAS detector and consists of the Pixel detector, the Semiconductor Tracker and the Transition Radiation Tracker. It can measure the direction, momentum and charge of electrically charged particles based on particle tracks. A track can then be reconstructed based on the hits a particle leaves within the tracking detector. The tracks are essential for determining the vertex the particles originate from and for assigning different signatures in other subdetectors to particles. In the Pixel and Semiconductor Tracker, a particle hit is measured by the ionisation of a depleted silicon diode, which creates electron-hole pairs. These charge carriers drift towards the electrodes, producing a signal. In the Transition Radiation Tracker, Xenon

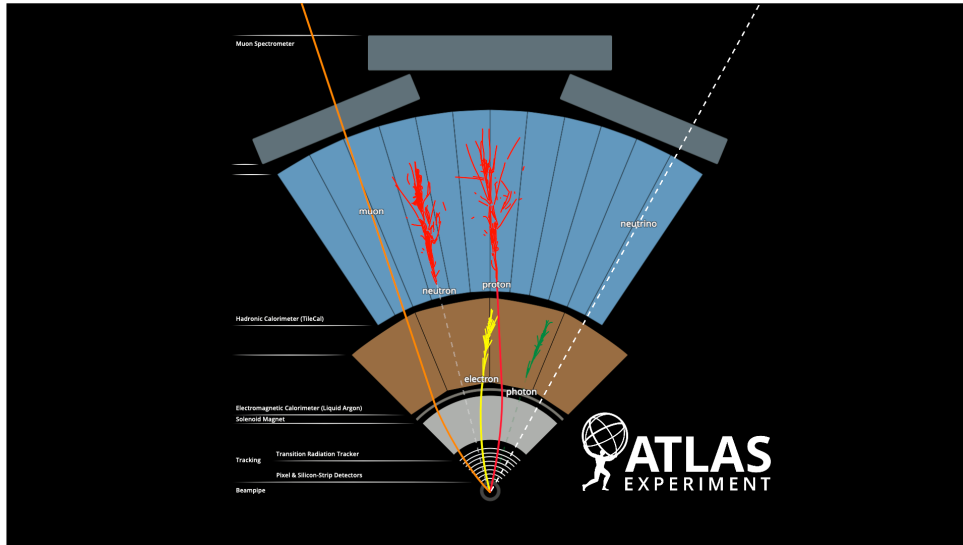


Figure 3.2.: Cross-section view of ATLAS with signatures of muons, electrons, photons, neutrons and protons in the different subdetectors ©CERN. Neutrinos leave the detector without interaction.

gas is ionised due to the transition radiation of a charged particle passing through a boundary between two different media.

The Calorimeters

In the calorimeters, the particles interact with a high density material and secondary particles with lower energy are created until the energy becomes too low and the particle is stopped. This process is called showering. The energy of the original particle can be inferred by the size of the shower.

The Liquid Argon Calorimeter surrounds the Inner Detector and measures the energy of electrons, photons and hadrons. It is a sampling calorimeter consisting of layers of metal (tungsten, copper or lead) which act as the shower generating material. Between the layers is liquid argon, which is ionised and creates a signal. Around the Liquid Argon Calorimeter is the Tile Calorimeter, which measures the energy of hadronic particles that have not deposited all their energy before. The showers are created in layers of steel and plastic scintillator tiles in between produce a measurable signal.

The Muon Spectrometers

Muons are minimal ionising particles which only weakly interact due to their high mass. That is why the outermost layer of ATLAS is reserved for the muon detector. All the other particles will have been stopped and absorbed before, except for neutrinos, which

3. *Experimental Setup*

will leave the detector without interaction. The Muon spectrometer consists of gas-filled detectors which are ionised by passing muons. This allows for a precise determination of the position and momentum of the muon.

The Magnet System

For measuring the momentum and charge of a particle, a magnetic field is necessary to bend the particle tracks. ATLAS has a central solenoid magnet located at the detector core surrounding the Inner Detector. It is superconducting and provides a magnetic field of $|\vec{B}| = 2 \text{ T}$. Moreover, there are three toroid magnets (two at the end of the detector, one surrounding the centre) which provide a magnetic field of $|\vec{B}| = 3.5 \text{ T}$, especially relevant for measuring the momentum of muons.

Trigger and Data Acquisition

In ATLAS, up to 1.7 billion collisions happen each second, equivalent to a data volume of 60 million megabytes per second. Because this would not be manageable, ATLAS filters out potentially interesting events using triggers. The first level trigger is a hardware trigger located on the detector, which works on a subset of information from the calorimeters and Muon Spectrometer. The second level trigger is a software trigger which conducts a detailed analysis of each event, examining information from various detector regions. Ultimately, about 1000 events per second are stored for offline analysis.

4. Modelling and Object Reconstruction

The work presented in this thesis is based on Monte Carlo simulations corresponding to the full Run 2 dataset taken with the ATLAS detector at $\sqrt{s} = 13$ TeV between 2015 and 2018. The integrated luminosity of the dataset is $140.1 \pm 1.2 \text{ fb}^{-1}$ [96]. This chapter describes the modelling of the different processes, the reconstruction of the physical objects from the simulated detector responses and the reconstruction of the top quark system from those objects.

4.1. Monte Carlo Simulations

The production of $t\bar{t}$ events was modelled using the POWHEGv2 generator [97–100] at NLO with the NNPDF3.0 [101] PDF set and the h_{damp} parameter set to $1.5 m_t$. The parton shower and hadronisation were modelled by PYTHIA 8 [102] using the NNPDF2.3 PDF set [103] and the parameters set according to the A14 tune [104]. In this analysis, two of these samples MC samples with at least one lepton $t\bar{t}$ events are used: one with the full detector simulation as nominal and one with a fast simulation AtlFast2 [105] for comparison to alternative samples. Alternative samples of the $t\bar{t}$ production are used for systematic modelling uncertainty, the differences between these samples and the nominal one are described in Chapter 5.

The associated production of single top quarks with W bosons (tW) was simulated using the POWHEGv2 generator at NLO in QCD using the five-flavour scheme and the parton shower was modelled using PYTHIA 8, using the same PDF sets as described above. The single top quark s - and t -channel productions were modelled with the same settings but the four- instead of five-flavour scheme.

The production of diboson final states was modelled using SHERPA 2.2.2 [106] and the NNPDF3.0 PDF set, including off-shell effects and Higgs boson contributions where ap-

4. Modelling and Object Reconstruction

appropriate at NLO accuracy in QCD for up to one and at LO accuracy for up to three additional parton emissions. The production of boson+jets processes was simulated using the SHERPA 2.2.2 generator with the same PDF set at NLO accuracy for up to two and LO accuracy for up to four additional partons.

The $t\bar{t}Z$ and $t\bar{t}W$ processes are modelled using the MADGRAPH_AMC@NLO 2.3.3 [107] generator at NLO and interfaced with PYTHIA using the same PDF sets as the $t\bar{t}$ sample. The production of the $t\bar{t}H$ process was simulated using the same generator setup as the $t\bar{t}$ sample. Lastly, the $t\bar{t}t\bar{t}$ process was modelled using the MADGRAPH_AMC@NLO 2.3.3 generator at NLO and the same settings as the $t\bar{t}Z$ and $t\bar{t}W$ processes.

4.2. Object Definitions

Electrons

Electrons are identified by the tracks they leave in the Inner Detector and the energy they deposit in the electromagnetic calorimeter, using a likelihood-based definition [108]. They are required to have a transverse momentum $p_T > 25/27/28$ GeV (for 2015+16/17/18, respectively) based on the single lepton trigger and pseudorapidity $|\eta| < 2.47$. The region of $1.37 < |\eta| < 1.52$ is excluded due to the LAr crack region. Electrons must pass the *FCTight* isolation criterion [109] in order to suppress contributions from non-prompt leptons. The transverse impact parameter d_0 needs to pass $|d_0/\sigma(d_0)| < 5$ and the longitudinal impact parameter z_0 needs to pass $|z_0 \sin \theta| < 0.5$ mm.

Muons

Muons can be identified via their tracks in the Muon Spectrometer and the Inner Detector. Similarly to the electrons, muons are required to have a transverse momentum $p_T > 25/27/28$ GeV (for 2015+16/17/18, respectively) based on the single lepton trigger and pseudorapidity $|\eta| < 2.5$. They also need to pass the *FCTight* isolation criterion. The transverse impact parameter d_0 needs to pass $|d_0/\sigma(d_0)| < 3$ and the longitudinal impact parameter z_0 needs to pass $|z_0 \sin \theta| < 0.5$ mm.

Jets

Jets are reconstructed using the anti- k_t algorithm [110] for jet clustering on particle flow objects [111] with a distance parameter of $R = 0.4$ based on the tracks in the Inner Detector and the energy deposition in the hadronic calorimeter. The jets are required

to have a transverse momentum $p_T > 25$ GeV and pseudorapidity $|\eta| < 2.5$. For jets with $p_T < 60$ GeV and $|\eta| < 2.4$ a JetVertexTagger requirement is applied to suppress contributions from pileup interactions [112]. Jets originating from B -hadrons are tagged using the DL1r tagger [113].

Missing Transverse Energy

The missing transverse momentum \vec{p}_T^{miss} and the missing transverse energy E_T^{miss} are determined based on the sum of reconstructed objects and the assumption of momentum and energy conservation in the transverse plane in pp collisions. Consequently, the missing transverse momentum can be calculated according to

$$\vec{p}_T^{\text{miss}} = -(\vec{p}_T^{\text{electrons}} + \vec{p}_T^{\text{muons}} + \vec{p}_T^{\text{jets}} + \vec{p}_T^{\text{soft}}), \quad (4.1)$$

where $\vec{p}_T^{\text{electrons/muons/jets}}$ describes the sum of the electrons/muons/jets transverse momentum and \vec{p}_T^{soft} the sum of all tracks not associated to any object.

Overlap Removal

In order to prevent signatures in the detector from being associated with more than one object, overlap removal is applied. Electrons are removed if they share an ID track with a muon or are within a $\Delta R < 0.4$ distance to a jet. Jets are removed if there is an electron within a $\Delta R < 0.2$ distance or if they have fewer than three tracks and there is a muon in $\Delta R < 0.2$ distance. Muons are removed if there are in a $\Delta R < 0.4$ distance of any remaining jet.

4.3. *b*-Tagging Algorithm

Since top quarks decay almost exclusively to b quarks, identifying b -jets is crucial to every top quark analysis. The b quark is the second-heaviest quark after the top quark and has an unusually high lifetime ($\tau \approx 1.5$ ps), despite its high mass, due to the CKM-suppressed decay possibilities of the b quark. This lifetime leads to a mean flight length of energetic b hadrons $\langle l \rangle = \beta\gamma c\tau$ of a few mm before decaying. These so-called secondary vertices can be measured within the detector.

Charm-jets display similar properties as b -jets and behave differently than light-flavoured jets, which is why b -tagging algorithms can more easily mistag c -jets as b -jets. This feature can help identify the down-type quark for the entanglement analysis in the semileptonic

4. Modelling and Object Reconstruction

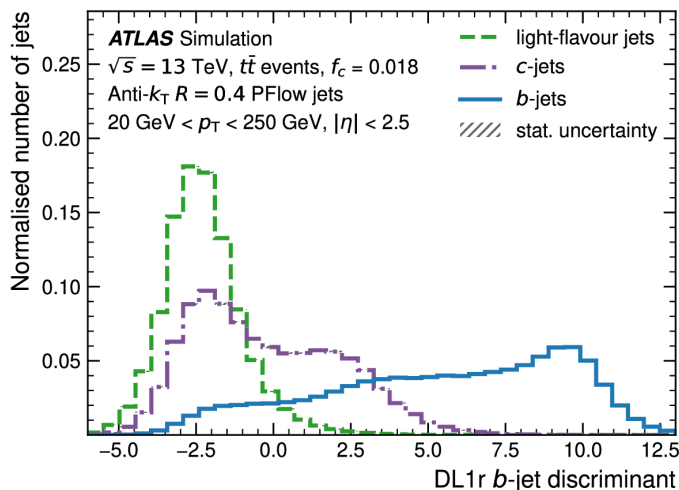


Figure 4.1.: Output distributions of the DL1r b -jet discriminant for b -jets, c -jets and light-flavour jets in $t\bar{t}$ simulated events [113].

decay channel since W bosons are expected to always decay into an up- and a down-type quark. If one of the jets associated with the W boson is a mistagged charm-jet, the other one should be a down-type jet suitable for spin analysis.

The algorithm is designed to tag jets as b -jets using the long lifetime, high mass, high decay multiplicity of B -hadrons and the properties of the heavy quark fragmentation [113]. The output distribution of the b -tagging score for b -jets, c -jets and light-flavoured jets of DL1r on a simulated $t\bar{t}$ sample is displayed in Figure 4.1. It is visible that the distribution for the b -jets is shifted to higher values of the discriminant, whereas the light-flavoured jets are shifted to lower values. The charm jets are located in between, demonstrating the difference to the other two categories. The b -jets distribution is not localised but spreads over various values. That is why working points were introduced, which include 85 %, 77 %, 70 % and 60 % of all the true b -jets, respectively. That means that the tightest working point, the 60 % working point, has a high purity but low efficiency, whereas the loosest working point, the 85 % working point, has a low purity but high efficiency. The intermediate working points are used to identify c -jets in the semileptonic decay channel, as this is where the b -jet and c -jet distributions overlap.

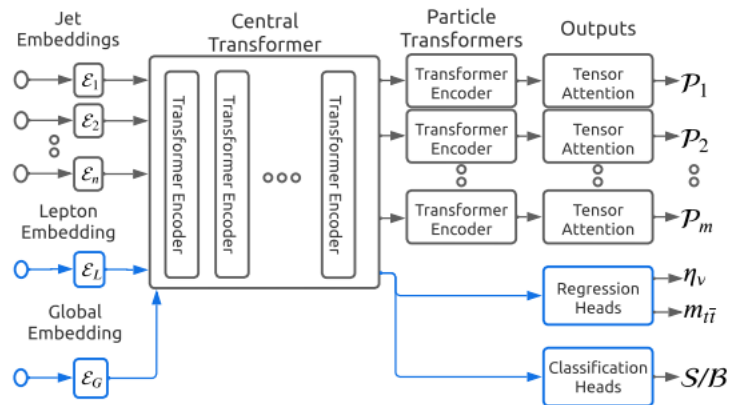


Figure 4.2.: High level structure of SPA-NET [117].

4.4. Kinematic Reconstruction of the Top-Anti-Top Quark System

Short-lived particles like the top quark cannot be measured directly in the detector but only via their longer-lived decay products. The main challenges for the kinematic top quark reconstruction are assigning particles to the top quarks and the intermediate decay products (W bosons) and determining the neutrino four-vector(s). These problems can be solved differently in the semileptonic and dileptonic decay channel.

4.4.1. Semileptonic Decay Channel

In the semileptonic decay channel, a major challenge is given by assigning the detected particles to the partons of the decay since many partons cannot be distinguished based on their detector signature. The combinatorics of the problem increase with the number of partons, and the efficiency of making the right choice decreases. This assignment problem can be solved analytically, for example with kinematic likelihoods as in KL FITTER [114]. This method is limited by the limited amount of kinetic information and the growing number of permutations. Alternatively, a machine learning approach can be used for the event reconstruction. This work uses SPA-NET, a symmetry preserving attention network [115–117].

In the input, jets are represented through their four-momenta and the b -tagging score as additional information. The leptons are incorporated through the charged leptons four-momentum with flavour information as well as the missing transverse energy characterising the neutrino kinematics in the transverse plane.

4. Modelling and Object Reconstruction

Table 4.1.: Reconstruction efficiencies for hadronically decaying (t_H) and leptonically decaying (t_L) top quarks and full events for semileptonic $t\bar{t}$ with SPA-NET and KLFITTER, taken from [117].

	Events	t_H	t_L
SPA-NET	76 %	73 %	85 %
KLFITTER	42 %	44 %	53 %

SPA-NET performs three different tasks: reconstruction, classification and regression. As an output, the assignment of detector objects to partons is given, as well as the regressed neutrino η and $M_{t\bar{t}}$ and a signal-versus-background classification score. The confidence of SPA-NET in its assignment of the hadronic and leptonic top quarks is quantified in a range between 0 and 1 via the SPA-NET `hadtop assignment` and SPA-NET `leptop assignment` variables, respectively. Similarly, SPA-NET provides information about how well the hadronic and leptonic top can be reconstructed at all via the SPA-NET `hadtop detection` and SPA-NET `leptop detection` variables.

In Figure 4.2, the high-level structure of SPA-NET is shown. It consists of four components: (1) independent jet embeddings, (2) a stack of transformer encoders, (3) transformer encoders for each particle and (4) a tensor-attention to produce the jet-parton assignment distributions.

The kinematics of neutrino can either be determined by SPA-NET via regression or analytically using a constraint on the mass of the W boson. For this analysis, both approaches yielded similar results, and the decision was made to use the traditional analytical reconstruction approach.

In Table 4.1, a comparison of the reconstruction efficiencies of SPA-NET and KLFITTER for semileptonic $t\bar{t}$ events is presented. The efficiencies are split into the hadronically decaying (t_H) and leptonically decaying (t_L) top quarks and the full event. It is remarkable that SPA-NET outperforms KLFITTER in every category and reaches efficiencies of $> 70\%$.

4.4.2. Dileptonic Decay Channel

The dileptonic decay channel of the $t\bar{t}$ system is particularly challenging to reconstruct because of the two undetected neutrinos in the final state. The measured objects in a dileptonic $t\bar{t}$ decay are two charged leptons, one or two tagged b -jets and missing transverse energy. In the case of only one tagged b -jet in the event, the untagged jet with the highest p_T is taken as the second b -jet. From this information, finding one distinct solution for the top quark kinematic reconstruction is impossible. However, several algorithms can be used to solve this problem: the Ellipse method [118], the Sonnenschein method [119] and the Neutrino Weighting method [120, 121].

The kinematics of the top quark and the anti-top quark are determined based on the kinematics of their decay products according to

$$p_t = p_b + p_{l^+} + p_\nu, \quad p_{\bar{t}} = p_{\bar{b}} + p_{l^-} + p_{\bar{\nu}}. \quad (4.2)$$

The assignment of the charged leptons to the top/anti-top quark can be done based on the charge, but the b -jets assignment is intertwined with the determination of the neutrino four vectors. In total, the system has eight unknowns that need to be determined. The solutions can be constrained through kinematic constraints on the known top quark and W boson mass

$$m_t^2 = (p_b + p_{l^+} + p_\nu)^2 = (p_{\bar{b}} + p_{l^-} + p_{\bar{\nu}})^2, \quad m_W^2 = (p_{l^+} + p_\nu)^2 = (p_{l^-} + p_{\bar{\nu}})^2, \quad (4.3)$$

and vanishing neutrino masses $m_\nu \approx m_{\bar{\nu}} \approx 0$. Together with the information on the E_T^{miss}

$$E_{T,x}^{\text{miss}} = p_{\nu,x} + p_{\bar{\nu},x}, \quad E_{T,y}^{\text{miss}} = p_{\nu,y} + p_{\bar{\nu},y}, \quad (4.4)$$

eight constraints can be used to solve for the eight unknowns. It has to be noted that these constraints assume SM processes only and that any BSM processes (e.g. a decay via supersymmetric particles) would skew the result.

The Sonnenschein method [119] uses the kinematic relations above and reduces the system of equations to two equations in $p_{\nu,x}$ and $p_{\nu,y}$ and solves the system analytically. The remaining neutrino kinematics can be determined from there on using the relations above. The Ellipse method [118] has a similar approach to the problem but solves the system geometrically. The W^+ and W^- kinematic constraints can be understood as ellipsoids in momentum-space with an intersection that consists of two ellipses, which are the con-

4. Modelling and Object Reconstruction

straints on the neutrino kinematics. Both of these approaches to the neutrino kinematics can yield no or multiple solutions, of which the one with the lowest $m_{t\bar{t}}$ is taken as the physical solution.

The Neutrino Weighting method [120, 121], in contrast, is an approximate numerical method which estimates the pseudorapidity of the neutrino η_ν by sampling from corresponding distributions generated from POWHEG+ PYTHIA NLO-QCD $t\bar{t}$ simulation. The remaining neutrino kinematics are again obtained via the kinematic constraint relations. Each solution from the sampled distribution is assigned a weight

$$w = \exp \left[\left(\frac{-\Delta E_x^2}{2\sigma_x^2} \right) \cdot \left(\frac{-\Delta E_y^2}{2\sigma_y^2} \right) \right], \quad (4.5)$$

based on the difference between the observed E_T^{miss} and the E_T^{miss} of the calculated solution ΔE and the resolution of the E_T^{miss} σ . The solution with the highest weight is picked at the end.

The samples used for this analysis used the Ellipse method in 85% of events and in case the Ellipse method failed to find a solution, the Neutrino Weighting method was used to solve the problem, which was the case for 5% of events. If that also failed (10% of events), each lepton was paired with the closest b -jet. The Sonnenschein method was not used because it is so similar to the Ellipse method that it fails in 99% of cases the Ellipse method fails and the Ellipse method was found to be better suitable as the default. For every method, all possible combinations of charged lepton and b -jet have been considered, and the most suitable one has been chosen. The assumptions on the W boson and top quark mass used in the Ellipse method are smeared according to their theoretical uncertainties with a Gaussian distribution with $\mu_W = 80.379$ GeV and $\sigma_W = 2.085$ GeV, $\mu_t = 172.5$ GeV and $\sigma_t = 1.480$ GeV.

5. Systematic Uncertainties

To estimate the sensitivity of an analysis, systematic uncertainties on the expected result must be studied. This chapter describes the sources of systematic uncertainties for the analyses. Unless stated otherwise, the results presented later include all of them.

5.1. Signal Modelling Uncertainties

The signal modelling systematic uncertainties are related to settings in the nominal $t\bar{t}$ MC POWHEG+PYTHIA 8 sample [39, 99, 100], which impact the distributions on all levels.

For the **p_T hard** uncertainty, the nominal sample is compared to one where the **pThard** setting in PYTHIA is set to 1 instead of 0. This assesses the uncertainty in the matching of the NLO matrix elements to the parton shower. The uncertainty concerning the differences between using different parton showers and hadronisation models is called the **Parton Shower**. It compares the nominal POWHEG+PYTHIA 8 sample to a POWHEG+HERWIG 7.13 sample [122, 123], using the HERWIG default set of tuned parameters [124] and the MMHT2014 PDF set [125].

An important setting of PYTHIA is the **recoil** parameter, which defines which final-state particle additional hard radiation will recoil off. The **Recoil to Top** systematic uncertainty compares the nominal sample with **recoilToColour** setting to one with **recoilToTop** setting [126]. Another relevant parameter is the **hdamp** parameter, which regulates the high- p_T radiation the $t\bar{t}$ system recoils against. The **hdamp** uncertainty describes the comparison of the nominal sample with a **hdamp** parameter of $1.5m_t$ to one with a **hdamp** parameter of $3m_t$.

Additionally, the **Top Decay** uncertainty estimates the difference in the modelling of the line shape of $M_{t\bar{t}}$. This is done by comparing the nominal sample to one in which MADSPIN [127] is allowed to decay the top quarks. In the nominal sample, the top quark decay is handled by POWHEG. The mass of the top quark is an important input param-

5. Systematic Uncertainties

eter, which is set to 172.5 GeV per default. In the **Top Mass** uncertainty, the nominal sample is compared to samples with a variation of m_t by 0.5 GeV. This estimates the effect of uncertainties on the top mass. For the **Colour Reconnection** uncertainty, the nominal sample with the MPI-based colour reconnection model is compared to samples using the different colour reconnection models (QCD-based or Gluon-move models) [128] and the largest difference is taken as the systematic uncertainty.

In the POWHEG matrix element (ME) generation, the renormalisation and factorisation scale can be varied to cover theoretical uncertainties. The **Scale μ_R** and **Scale μ_F** uncertainty is estimated by comparing the nominal event weight to one with a variation of the scales by a factor of 2 up and down. Similarly, the **ISR α_S** and **FSR α_S** uncertainty is estimated by comparing the nominal event weight to one with a variation of ISR α_S and FSR α_S by a factor of 2 up and down in the POWHEGME generation. For the **PDF** uncertainty, the nominal event weight is compared to one with a variation of the PDF using the PDF4LHC [129] decomposition in the POWHEGME generation.

5.2. Experimental Uncertainties

The systematic uncertainties considered for electrons and muons arise due to the uncertainty in their reconstruction, identification, isolation and trigger efficiencies. The uncertainties are considered via variations of the scale factors for the leptons. They are measured using tag-and-probe measurements in Z and J/Ψ decays [108, 130].

The systematic uncertainties associated with jets are separated into those related to the Jet Energy Scale (JES), for which the flavour response is considered separately, the Jet Energy Resolution, and the Jet Vertex Tagging. The JES is derived from test-beam data, LHC collision data and simulation [131]. The b -tagging algorithm has uncertainties associated with the calibration, which are incorporated in varying the b -tagging scale factors. There are 45 variations for the b -jet, 20 for the c -jet and 20 for the light-jet calibration. There is also an uncertainty covering the uncertainty in the extrapolation of the scale factors to high p_T jets. The uncertainties on the energy scales and resolutions of leptons and jets are propagated to calculate the missing transverse momentum. Also, there are scale and resolution uncertainties associated with the soft term. The luminosity uncertainty is also propagated, there are uncertainties on the normalisation of the background and on the estimation of pile-up effects applied.

6. Quantum Entanglement in the Semileptonic Decay Channel

As a critical feature of quantum mechanics, quantum entanglement in top quark pairs holds the unique potential to test quantum mechanics at high energy scales and the SM in unexplored phase spaces [14]. This chapter presents the first sensitivity study for entanglement in top quark pairs in the semileptonic decay channel at the ATLAS experiment. All results shown are expected sensitivities based on simulations. No data has been considered yet.

6.1. Event Selection

For selecting the semileptonic $t\bar{t}$ final state in detector-level events, the following preselection has been applied:

- exactly one electron or muon with $p_T > 25/27/28$ GeV (for 2015 + 16/17/18, respectively),
- missing transverse energy of at least 20 GeV,
- at least four jets with $p_T > 25$ GeV,
- at least two b -tagged jets at the 60% efficiency working point of DL1r.

A region enriched in c -jets has been defined to access the down-type jet for spin analysis. Further explanation for the choice of the down-type jet as the hadronic spin analyser can be found in Chapter 6.3. For the c -jet enriched region, the two jets SPA-NET assigned to the hadronically decaying W boson are checked for their b -tagging scores since c -jets behave similarly to b -jets, as described in Chapter 4.3. With this, the decay modes $W \rightarrow cs$ and $W \rightarrow cd$ can be selected, of which the latter is suppressed. This makes up roughly half of all hadronic W boson decays. The non- c -tagged jet can consequently be taken as the down-type jet useful for the analysis. The other hadronic decay modes $W \rightarrow ud$

6. Quantum Entanglement in the Semileptonic Decay Channel

Table 6.1.: Overview of a fraction of events with correctly matched, incorrectly matched or non-reconstructible down-type jets.

	correctly matched	incorrectly matched	non-reconstructible
inclusive	54.1 %	14.1 %	31.8 %
hadtop detection > 0.7	73.1 %	13.5 %	13.4 %

(dominant), $W \rightarrow us$ (suppressed), $W \rightarrow ub$ (suppressed) and $W \rightarrow cb$ (suppressed) are not taken into account. The c -tagged region is constructed as follows:

- The two jets assigned to the hadronic W boson must have different b -tagging working points. This means that the jets are distinguishable.
- These two jets are required to have a b -tagging working point lower than the 60% efficiency one. This ensures that the c -tagged jet is not, in reality, a misassigned b -jet coming from the top quark instead of the W boson.

If these two requirements are met, the jet with the lower b -tagging score is considered the down-type jet for constructing the spin-sensitive observable.

Moreover, the signal region only considers events with top quarks produced near the production threshold, meaning $M_{t\bar{t}} < 390$ GeV. The validation regions consider the ranges 390 GeV $< M_{t\bar{t}} < 500$ GeV and $M_{t\bar{t}} > 500$ GeV.

In addition to selection of the region low in $M_{t\bar{t}}$, a requirement on $\beta_{t\bar{t}} = p_{t\bar{t}}/E_{t\bar{t}} < 0.55$ is applied in order to enhance the fraction of ggF induced states even more. Moreover, only well-reconstructible events are selected to suppress systematic uncertainties, which show a larger effect in badly reconstructed events. This is done by requiring SPA-NET `hadtop detection` > 0.7, a measure of confidence of SPA-NET for reconstructing the hadronic top at all, as further described in Chapter 4.4.1. Table 6.1 shows the fraction of events with correctly matched, incorrectly matched or non-reconstructible down-type jets. Correctly matched means that the jet chosen as down-type corresponds to the true down-type quark on parton-level. Incorrectly matched means the down-type jet exists in the jet selection but has not been correctly identified. If the down-type jet is not reconstructible, the down-type jet is not in the jet collection on detector-level. It is visible that selecting events with a high value of the SPA-NET `hadtop detection` variable increases the fraction of correctly matched events significantly. In Figure 6.1, the distribution of correctly matched, incorrectly matched and non-reconstructible events as a function of SPA-NET `hadtop detection` is shown, illustrating how the fraction of correctly matched down-type jets increases with the hadtop detection.

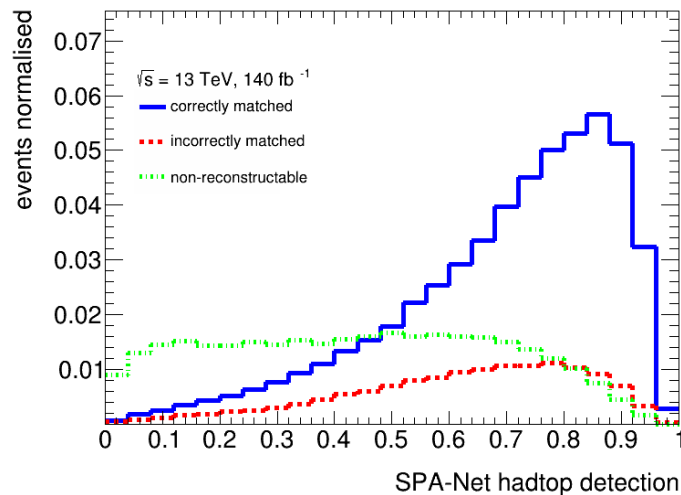


Figure 6.1.: Fraction of events with correctly matched, incorrectly matched or non-reconstructable down-type jets as a function of SPA-NET hadtop detection. The fraction of correctly matched down-type jets increases with the hadtop detection score.

The theoretical predictions about quantum entanglement are only valid on the parton-level because detector effects dilute and smear the measurements. The process $pp \rightarrow t\bar{t} \rightarrow b\bar{b}W^+W^- \rightarrow b\bar{b}l\nu q\bar{q}'$ is theoretically modelled, denoted as parton-level. The parton-level is used for comparisons to theory predictions.

On parton-level, there is no assignment uncertainty and the event selection can be formulated as

- two b quarks coming from the top quark directly,
- one charged lepton coming from the W boson,
- one neutrino coming from the W boson,
- two quarks coming from the other W boson.

Equivalent to the detector-level selection, a region with one charm quark coming from the W boson and the respective orthogonal region are defined. Also, the selection on $M_{t\bar{t}}$ and $\beta_{t\bar{t}}$ is applied.

Additionally, there is the particle-level on which the jet formation has been applied and which is used to disentangle some systematic uncertainties. The selection applied to particle-level matches the one on parton-level.

6.2. Analysis Strategy

The basic principle of measuring entangled top quark pairs is to construct the entanglement marker D and test it against the entanglement limit

$$D < -1/3, \quad (6.1)$$

as derived in Chapter 2.3.1. This relation is only valid at parton-level, but measurements cannot directly access these values. Therefore, a method to map the measured values to the parton-level equivalent is necessary. An approach using profile-likelihood unfolding to unfold the $\cos\varphi$ distribution from detector- to parton-level showed a bias based on the MC simulation used to perform the unfolding. Instead, the more robust method, the calibration curve, has been chosen.

The calibration curve corrects the measured values for detector effects to the fiducial particle-level as a first step after subtracting the expected background. In a second step, the parton-level entanglement limit is propagated to particle-level as well using a second calibration curve such that the test can be performed at particle-level, reducing the systematic uncertainties.

The D values are extracted from the $\cos\varphi$ distribution using the relation $D = -3\langle\cos\varphi\rangle/\alpha_h$. To construct a complete curve, several hypotheses for D_{parton} , i.e. different physics scenarios, are created and propagated to particle and detector-level. Each pair of D values is plotted, and a first-order polynomial is fitted to interpolate between the points. An illustration of the method is shown in Figure 6.2. Once the curve is created, every measured value can be calibrated to its corresponding D_{particle} value and compared to the particle-level entanglement limit. The uncertainty on the calibrated parameter is obtained by mapping the measured value to its corresponding upper and lower limit within the uncertainty band, as illustrated in Figure 6.2.

The degrees of entanglement cannot easily be changed in the MC simulation samples since the effect of entanglement is fundamentally built into the underlying field theory. Therefore, it cannot be changed at the generator level to generate alternate samples. However, because the degree of entanglement can directly be accessed via the D coefficient extracted from a linear distribution, the slope of the parton-level $\cos\varphi$ distribution can be manipulated to create different entanglement scenarios. This is done by assigning a weight w to each event based on the parton-level $\cos\varphi$ and $D_{\text{parton}}(M_{t\bar{t}})$ values and a

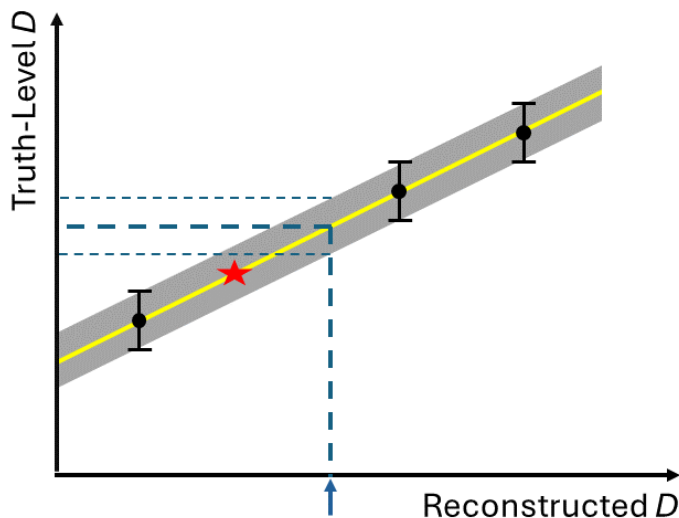


Figure 6.2.: Schematic representation of a calibration curve. The red asterisk marks the nominal SM prediction based on MC simulations. The black points are the reweighted points representing alternative levels of entanglement. The points are linearly interpolated, which creates the calibration curve. The blue arrow shows a possible measurement of D , which is mapped to the respective truth-level value. The uncertainty band is shown in grey.

scaling factor χ

$$w(M_{t\bar{t}}, \chi) = \frac{1 - D_{\text{parton}}(M_{t\bar{t}}) \cdot \chi \cdot \cos \varphi}{1 - D_{\text{parton}}(M_{t\bar{t}}) \cdot \cos \varphi}. \quad (6.2)$$

The $D_{\text{parton}}(M_{t\bar{t}})$ values are determined separately for every sample based on a parton-level $\cos \varphi$ versus $M_{t\bar{t}}$ matrix with a 1 GeV resolution for $M_{t\bar{t}}$. The resulting distribution of $D_{\text{parton}}(M_{t\bar{t}})$ can be seen in Figure 6.3. Five points with the scaling factors $\chi = \{0.4, 0.6, 0.8, 1.0, 1.2\}$ are used for the calibration curve. The resulting distributions are shown in Figure 6.4. They must retain their linearity under the reweighting. The weights obtained from the parton-level $\cos \varphi$ distribution are also propagated to particle- and detector-level.

For each source of systematic uncertainty, a new calibration curve is produced and the expected values are corrected to particle-level as described above. The uncertainty is taken as the shift between the expected nominal result and the systematically shifted result. In the case of a one-sided systematic uncertainty, when a systematic shift only exists in one direction, the total difference is taken in both directions. If the uncertainty is asymmetric, the larger of the two variations is symmetrised, resulting in $D \pm \Delta D$ with the symmetric uncertainty ΔD . The dominating systematic uncertainty in the analysis is the

6. Quantum Entanglement in the Semileptonic Decay Channel

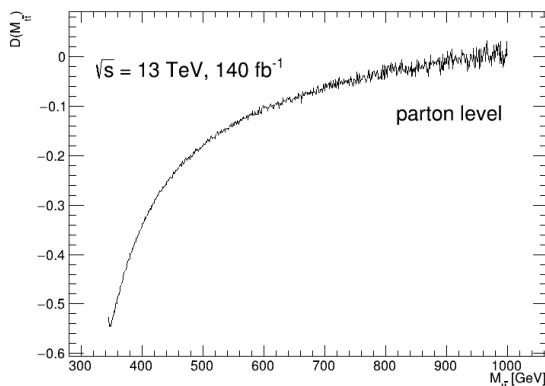


Figure 6.3.: Distribution of the $D_{\text{parton}}(M_{t\bar{t}})$ values for the nominal sample, used for reweighting.

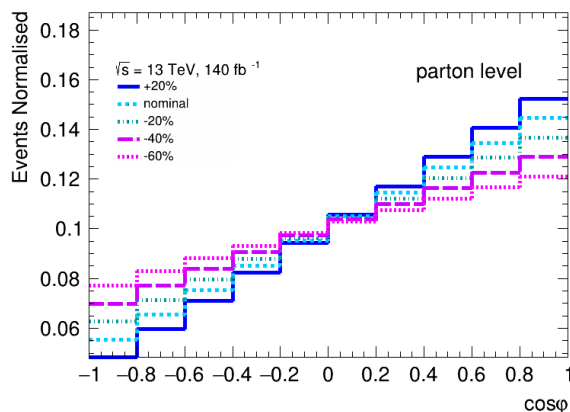


Figure 6.4.: Reweighted $\cos \varphi_{ld}$ distributions on parton-level used for creating the calibration curve.

choice of the parton shower, which compares the string hadronisation model implemented in PYTHIA to the cluster hadronisation model used in HERWIG. The systematic shift due to the parton shower uncertainty is similar on detector- and particle-level, as seen in Figure 6.5. Still, the effect is negligible on parton-level since no FSR radiation is applied to the top quarks and W bosons yet. Consequently, the curves for the different parton shower generators mapping detector- to particle-level do not show a difference as big as the one mapping detector- to parton-level directly. The parton shower systematic uncertainty is not applied to the propagation of the entanglement limit from parton- to particle-level, but instead, the entanglement limits are propagated separately using the two different generators. The same procedure has also already been employed in the analysis of the dileptonic decay channel [11].

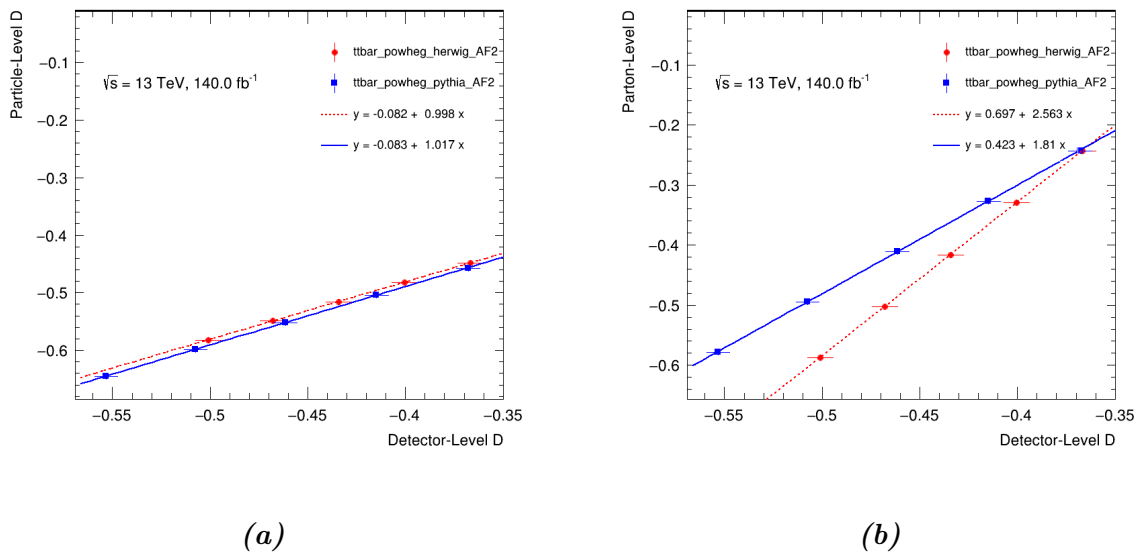


Figure 6.5.: Calibration curves mapping the detector-level D , extracted using $\cos \varphi_{ld}$, to a) particle-level D , b) parton-level D for both parton shower generators. It is visible that the systematic shift is larger if the detector-level D is directly mapped to the parton-level D .

6.3. Sensitivity Study

The sensitivity to quantum entanglement in the semileptonic decay channel highly depends on the choice of the hadronic spin analyser. In this analysis, the down-type jet from the hadronically decaying W boson, the b -jet from the hadronically decaying top quark and the optimal hadronic polarimeter, q_{opt} , have been studied. Identifying the down-type quark is experimentally challenging, as is assigning the b -quarks and the jets to the hadronically decaying W boson. Figure 6.6 compares the $\cos \varphi$ distributions with the different hadronic spin analysers on parton- and particle-level. On parton-level, all distributions are linear, but on particle-level, the distributions of $\cos \varphi_b$ and $\cos \varphi_{q_{\text{opt}}}$ show non-linear behaviour. This non-linear behaviour appears due to misassignment of the hadronic b -jet on particle-level, which does not affect the $\cos \varphi_{\text{down}}$ so much. Due to the non-linearities, the differential cross-section relation in Equation (2.25) does not hold, and the entanglement marker D cannot be extracted anymore. That is why the down-type quark was chosen as the hadronic spin analyser.

6. Quantum Entanglement in the Semileptonic Decay Channel

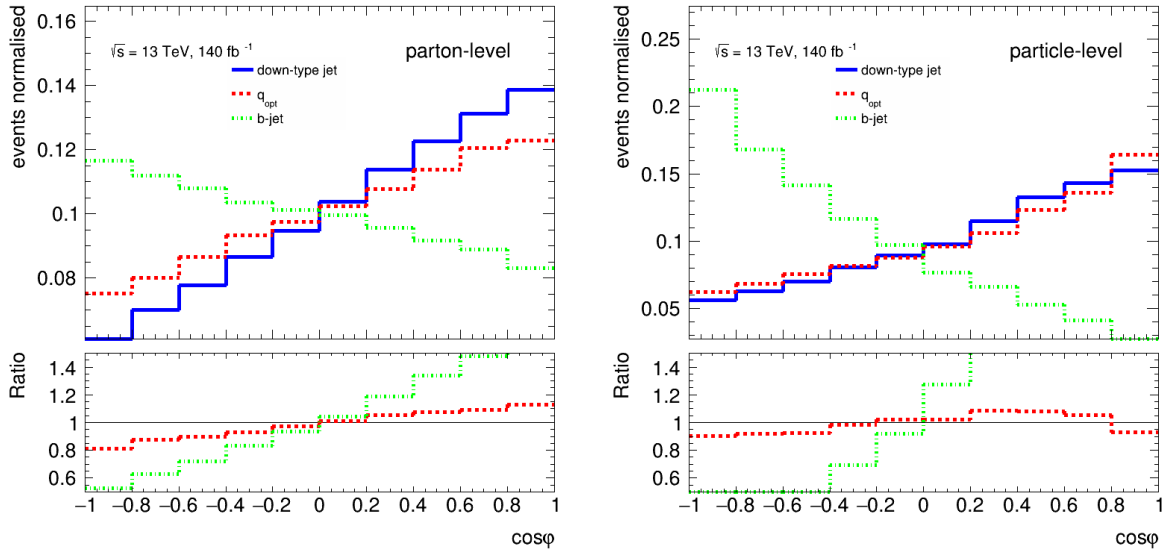


Figure 6.6.: Comparison of the $\cos \varphi$ distributions with the different hadronic spin analysers on parton- and particle-level.

6.3.1. Detector-Level Distributions

The distributions of $\cos \varphi$ in the signal and validation region can be seen in Figure 6.7. The signal is dominant. The shape of the distribution is linear as expected and necessary for the analysis. The background contribution can be seen closer in Figure 6.8 where the variables used for the event selection ($M_{t\bar{t}}$, SPA-NET hadtop detection and $\beta_{t\bar{t}}$) are shown with a logarithmic axis.

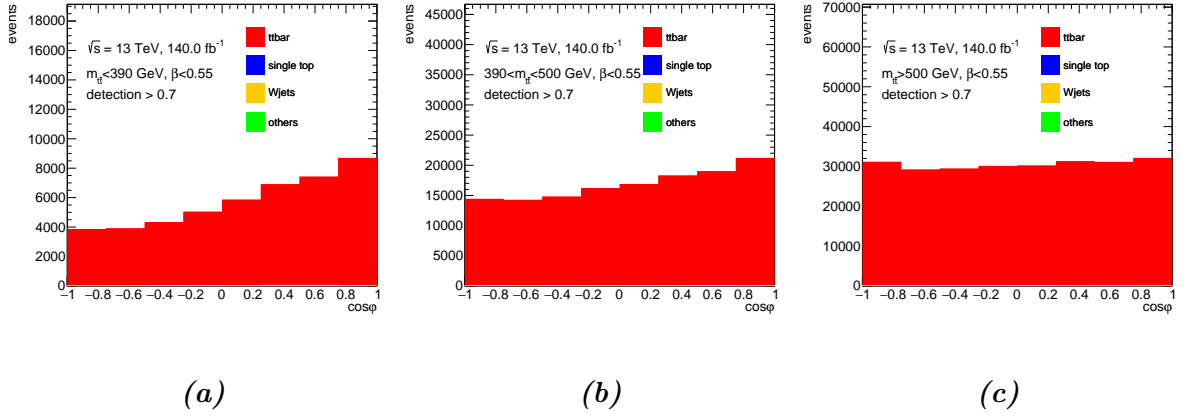


Figure 6.7.: Detector-level distributions of the $\cos \varphi$ observable in the signal region **a)** and the two validation regions **b)** and **c)** with higher $M_{t\bar{t}}$ requirements.

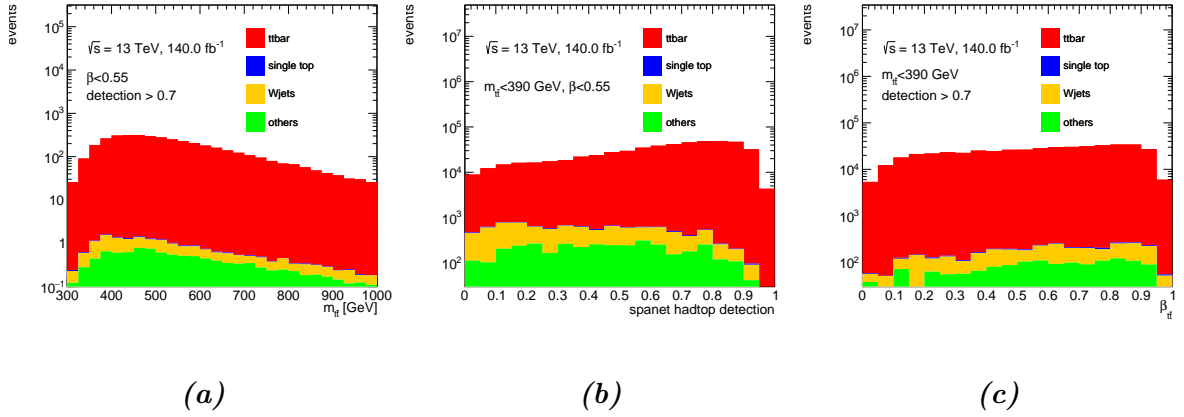


Figure 6.8.: Detector-level distributions of the variables which were used for the event selection. The y -axis is logarithmic to show the contribution of the background. Figure **a)** shows the distribution of $M_{t\bar{t}}$, **b)** of the SPA-NET hadtop detection and **c)** of $\beta_{t\bar{t}}$.

6.3.2. Curve from Detector- to Particle-Level

The calibration curve mapping detector-level to particle-level is shown in Figure 6.9 for the signal region and in Figure 6.10 for the validation regions. The expected value based on the MC simulations is highlighted with an asterisk. The uncertainty bands are shown for the statistical uncertainty and the total uncertainty. Table 6.2 lists the dominating sources of systematic uncertainty. Uncertainties associated with modelling the signal process, particularly the choice of parton shower algorithm, have the most significant impact on the calibration curve. The parton shower uncertainty was discussed in detail in Chapter 5, and the impact was reduced by selecting only events that are likely to be fully reconstructible. The more significant impact of the signal modelling has also been

6. Quantum Entanglement in the Semileptonic Decay Channel

Table 6.2.: Ranking of the impact of the ten most dominant sources of systematic uncertainty on the calibration of D from detector- to particle-level with their absolute and relative size.

Name of the Uncertainty	Absolute Size	Relative Size [%]
Parton Shower	0.0076	1.27
Jet Pile-up ρ topology	0.0064	1.08
$t\bar{t}$ Line Shape	0.0059	0.99
$t\bar{t}$ $p_{T\text{hard}}$	0.0059	0.98
Top Mass	0.0040	0.67
b -tag (Light) NP-0	0.0038	0.64
Jet JER NP-4	0.0028	0.47
$t\bar{t}$ Colour Reconnection	0.0019	0.31
b -tag (Charm) NP-0	0.0018	0.30
Jet JER NP-8	0.0017	0.28

observed in the analysis of quantum entanglement in the dileptonic $t\bar{t}$ channel [11].

The systematic uncertainties have a more significant impact on the curves in the validation regions since the event selection has only been optimised with respect to the significance in the signal region. Still, it is visible that the expected values for D in the validation regions differ from the one in the signal region. It is also expected that the D value in the intermediate region ($390 \text{ GeV} < M_{t\bar{t}} < 500 \text{ GeV}$) is lower than in the upper region ($M_{t\bar{t}} > 500 \text{ GeV}$), since there still is some level of entanglement in the intermediate region (see Figure 2.9).

The expected result in the signal region yields

$$D_{\text{particle}} = -0.598 \pm 0.006(\text{stat.}) \pm 0.017(\text{syst.}) \quad (M_{t\bar{t}} < 390 \text{ GeV}) \quad (6.3)$$

and in the validation regions

$$D_{\text{particle}} = -0.288 \pm 0.003(\text{stat.}) \pm 0.029(\text{syst.}) \quad (390 \text{ GeV} < M_{t\bar{t}} < 500 \text{ GeV}), \quad (6.4)$$

$$D_{\text{particle}} = -0.089 \pm 0.002(\text{stat.}) \pm 0.018(\text{syst.}) \quad (M_{t\bar{t}} > 500 \text{ GeV}). \quad (6.5)$$

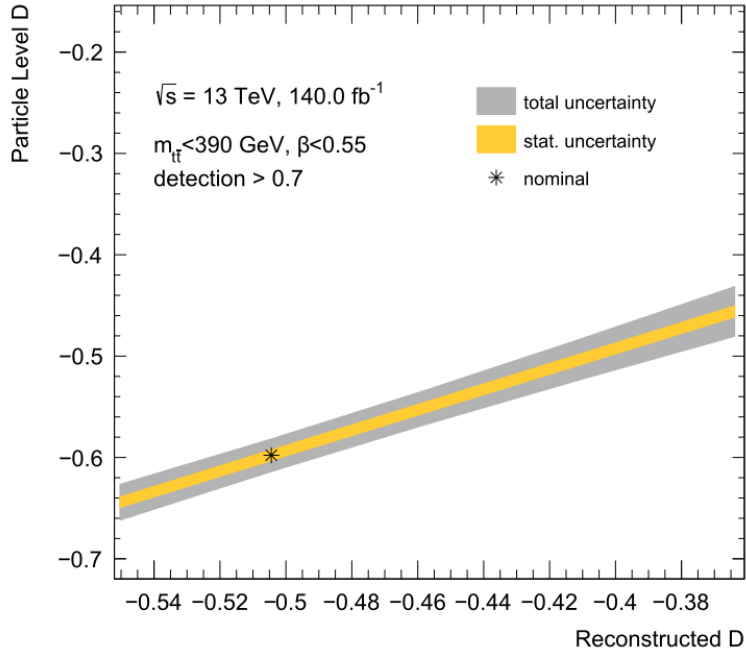
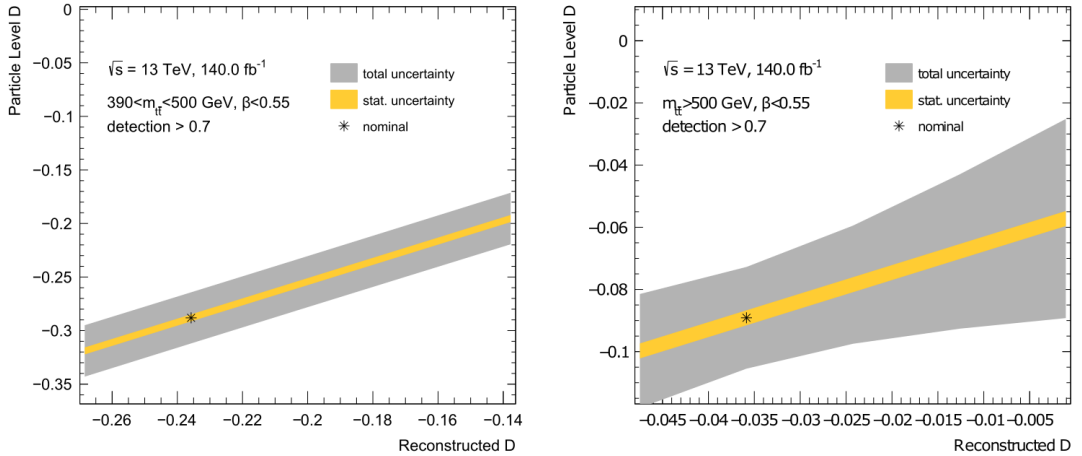


Figure 6.9.: Calibration curve mapping the detector-level D value to the particle-level value, including statistical and systematic uncertainties. The nominal predicted value is marked with an asterisk.



(a)

(b)

Figure 6.10.: Calibration curves mapping the detector-level D value to the particle-level value for the validation region a) with $390 \text{ GeV} < M_{t\bar{t}} < 500 \text{ GeV}$ and b) with $M_{t\bar{t}} > 500 \text{ GeV}$, including statistical and systematic uncertainties. The nominal predicted value is marked with an asterisk.

6.3.3. Curve from Parton- to Particle-Level

The curve mapping the parton-level to particle-level to propagate the entanglement limit in the signal region from parton-level is displayed in Figure 6.11. The point corresponding to the limit of $D_{\text{parton}} = -1/3$ is highlighted with an asterisk. The statistical uncertainty is negligible, and the systematic uncertainties are significantly lower than those of the detector-to-particle-level curve. Only the signal modelling uncertainties are considered in this curve, since the experimental uncertainties cannot be applied at either the particle- or parton-level. Since the entanglement limit is propagated separately for the two parton shower generators, this curve does not include the parton shower uncertainty. A comparison of the two curves is provided in Figure 6.12. A list of the most dominant systematic uncertainties is provided in Table 6.3.

The entanglement limits on particle-level are determined to be

$$D_{\text{particle}}^{-1/3} = -0.507 \pm 0.007(\text{syst.}) \quad (\text{PYTHIA}), \quad (6.6)$$

$$D_{\text{particle}}^{-1/3} = -0.484 \pm 0.006(\text{syst.}) \quad (\text{HERWIG}). \quad (6.7)$$

with a negligible statistical uncertainty of $1.8 \cdot 10^{-4}$. The relative size of the systematic uncertainties are assumed to be equal for both parton shower generators and are not determined again for the HERWIG sample.

The expected signal significance with respect to both parton shower generators, determined after Equation (2.27), are found to be

$$Z(\text{PYTHIA}) = 5.1 \sigma, \quad (6.8)$$

$$Z(\text{HERWIG}) = 6.4 \sigma. \quad (6.9)$$

An overview of the final results with MC simulations can be found in Figure 6.13. The results obtained using PYTHIA and HERWIG are in good agreement in the validation regions above the entanglement threshold. Still, tension is visible in the entangled signal region.

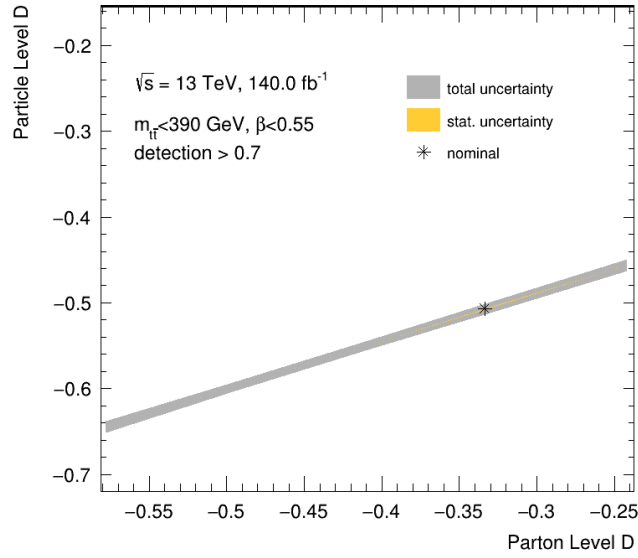


Figure 6.11.: Calibration curve mapping the parton-level D value to the particle-level value, including statistical and systematic uncertainties. The limit of $D = -1/3$ is marked with an asterisk.

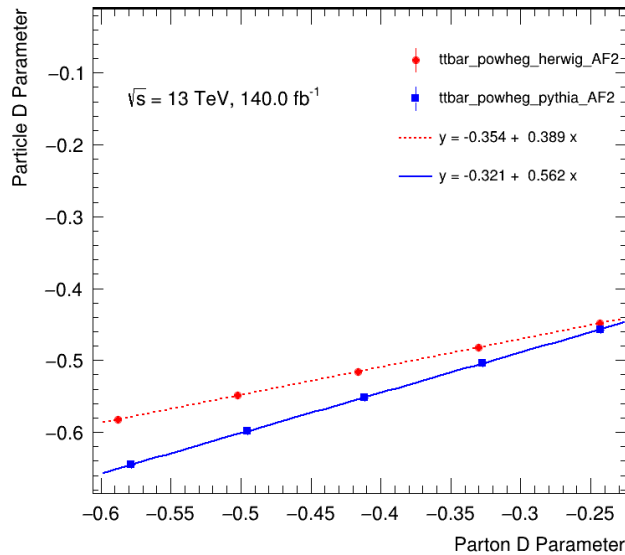


Figure 6.12.: Comparison of the calibration curves mapping from parton-level to particle-level D , generated using POWHEG+PYTHIA and POWHEG+HERWIG.

6. Quantum Entanglement in the Semileptonic Decay Channel

Table 6.3.: Ranking of the impact of the ten most dominant sources of systematic uncertainty on the calibration of D from parton- to particle-level with their absolute and relative size. Only the $t\bar{t}$ modelling uncertainties are considered.

Name of the Uncertainty	Absolute Size	Relative Size [%]
$t\bar{t}$ Line Shape	0.0051	1.00
Recoil to Top	0.0028	0.55
Top Mass	0.0018	0.34
$t\bar{t}$ $p_{T\text{hard}}$	0.0008	0.18
$t\bar{t}$ Colour Reconnection	0.0005	0.10
Scale μ_F	0.0005	0.10
$t\bar{t}$ hdamp	0.0003	0.06
PDF	0.0001	0.02
ISR	<0.0001	0.02
Scale μ_R	<0.0001	0.01

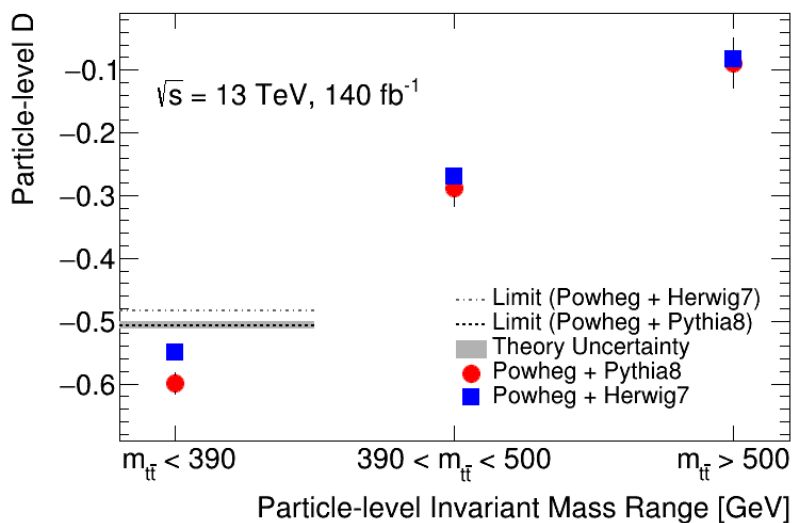


Figure 6.13.: Particle-level D value for the signal and validation regions and the particle-level entanglement limit. The expected values using PYTHIA, shown in red, agree well with the expected values using HERWIG, shown in blue, in the validation regions but show a discrepancy in the signal region. Both the expected values are below the entanglement limit in the signal region.

6.3.4. Comparison to Measurements Already Performed

ATLAS Measurement

A similar analysis to the one presented in this thesis has already been performed and published in the dileptonic decay channel of the $t\bar{t}$ system by the ATLAS collaboration in 2023 [11]. The analysis strategy using the calibration curve is identical, but the dileptonic decay channel profits from a cleaner signal due to the use of charged leptons and easier identification. At the same time, there are the challenges of reconstructing two neutrinos in the final states and reduced statistics. For the dileptonic decay channel, only a requirement on the mass of the $t\bar{t}$ system has been applied ($M_{t\bar{t}} < 380$ GeV), and there was no selection based on the $\beta_{t\bar{t}}$ or any reconstructibility criterion.

The observed (expected) results of the ATLAS dileptonic analysis are

$$D_{\text{particle}} = -0.547 \pm 0.002(\text{stat.}) \pm 0.021(\text{syst.}) \\ (-0.470 \pm 0.002(\text{stat.}) \pm 0.018(\text{syst.}))$$

for the signal region $M_{t\bar{t}} < 380$ GeV with a propagated entanglement limit of

$$D_{\text{particle}}^{-1/3} = -0.322 \pm 0.009 \quad (\text{PYTHIA}), \quad (6.10)$$

$$D_{\text{particle}}^{-1/3} = -0.27 \quad (\text{HERWIG}), \quad (6.11)$$

corresponding to the observation of quantum entanglement. A comparison of the results in the dileptonic and semileptonic decay channel can be seen in Figure 6.14. The expected D values on particle-level for the dileptonic decay channel are in a similar range to the ones predicted in this thesis. The propagated entanglement limit on particle-level has a higher value than the one in the semileptonic decay channel, which leads to a larger significance. This might be due to the reconstruction mechanism on particle-level, which is less trivial for the semileptonic decay channel.

Most importantly, the measurement of quantum entanglement in the dileptonic decay channel shows more entanglement than predicted by the MC simulations, which can be seen by comparing the data point to the prediction in the signal region. One explanation lies in the possibility of the hypothetical pseudo-bound toponium states, which would impact the top quark pair production at the production threshold and increase the level of entanglement [54]. The measurement in the semileptonic decay channel could complement the results already obtained in the dileptonic decay channel with ATLAS and investigate the tension observed further.

6. Quantum Entanglement in the Semileptonic Decay Channel

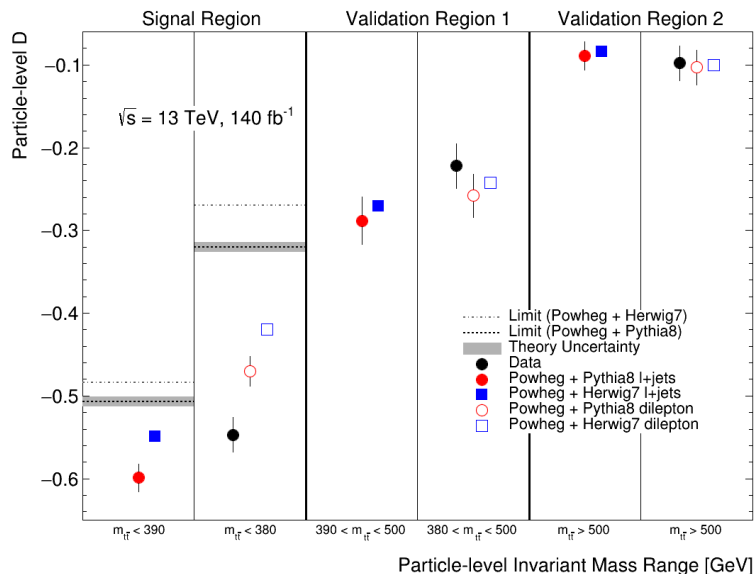


Figure 6.14.: Comparison of the results of the measurement in the dileptonic decay channel and the expected results obtained in this thesis. The particle-level D values for the signal and validation regions and the particle-level entanglement limits are shown. Dilepton results taken from [11].

CMS Measurements

In 2024, the CMS collaboration observed quantum entanglement as well in top quark pairs in the dileptonic decay channel [12]. In contrast to the ATLAS strategy, the CMS collaboration unfolded the $\cos\varphi$ distributions to parton-level, observing no bias from the input of MC simulations. The signal region probed included events with $M_{t\bar{t}} < 400$ GeV and $\beta_{t\bar{t}} < 0.9$ with a dataset corresponding to an integrated luminosity of 35.9 fb^{-1} .

The observed (expected) result in the signal region is [12]

$$D_{\text{parton}} = -0.478_{-0.027}^{+0.025} \quad (-0.465_{-0.028}^{+0.025}).$$

In their simulation, the hypothetical toponium state was included [54]. In Figure 6.15, an overview of the analysis results is presented and both approaches, with and without the toponium state, are shown. Without toponium, CMS observes a similar tension between the prediction and the measurement in the signal region, but including the toponium state seems to resolve that tension.

Also in 2024, the CMS collaboration measured quantum entanglement in top quark pairs in the semileptonic decay channel [13]. They performed a binned profile likelihood fit and

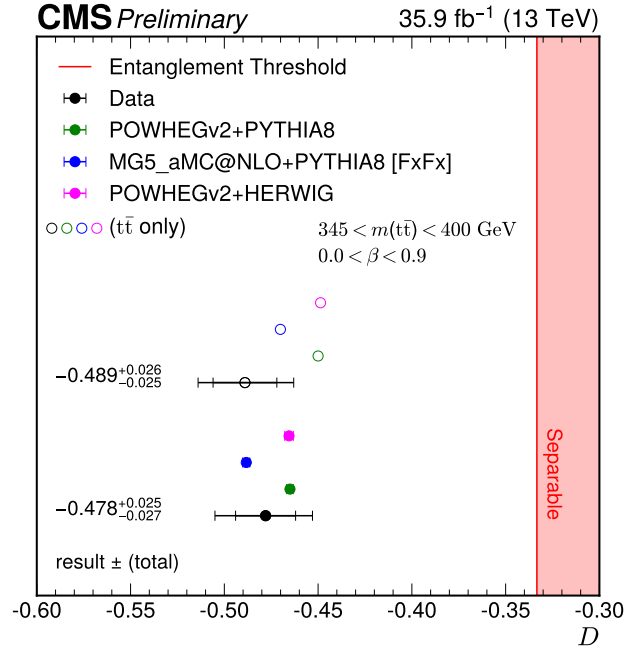


Figure 6.15.: Summary of the measurement in the dileptonic decay channel by the CMS collaboration. The results for the entanglement marker D compared to the expectations including (filled) or not including (open) contributions from the hypothetical toponium state are shown [12].

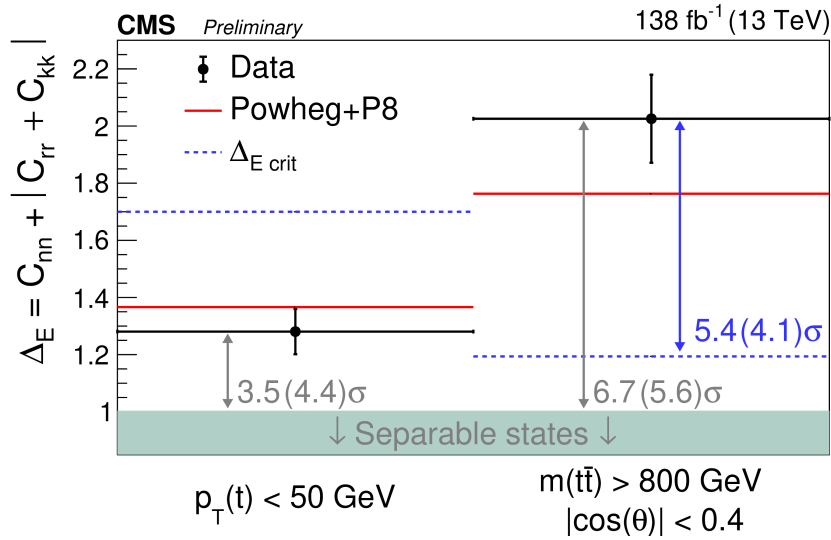


Figure 6.16.: Summary of the measurement in the semileptonic decay channel by the CMS collaboration. The levels of entanglement in the threshold region (first bin) and the high $M_{t\bar{t}}$ regime (second bin) are shown [13].

6. Quantum Entanglement in the Semileptonic Decay Channel

extracted all coefficients of the polarisation vectors and the spin correlation matrix. The used dataset corresponds to an integrated luminosity of 138 fb^{-1} . The measurement is performed in different regions, and the ones with the highest sensitivity to entanglement are shown in Figure 6.16. The first region is comparable to the threshold region already explored in the dileptonic decay channel, but instead of a requirement of $M_{t\bar{t}}$, the $p_T(t)$ is required to be $< 50 \text{ GeV}$. The observed (expected) significance of entanglement in this region is $3.5(4.4) \sigma$. The second region is a novelty, as entanglement has never been measured in the high $M_{t\bar{t}}$ regime. The region selects events with $M_{t\bar{t}} > 800 \text{ GeV}$ and $|\cos \theta| < 0.4$ with θ being the top quark scattering angle in the helicity basis. The observed (expected) significance of entanglement in this region is $6.7(5.6) \sigma$. This measurement is particularly significant as it is a first step towards testing the Bell inequalities in top quark pairs. The paper demonstrates that the high $M_{t\bar{t}}$ region is enriched in space-like separated top quark pairs, meaning that the entanglement can genuinely not be explained by any classical theory of communication.

7. Quantum Discord in the Dileptonic Decay Channel

While quantum entanglement can only be measured in correlated systems that are an inseparable whole, quantum discord is separately measured for each constituent of the correlation. This allows the test for new CP -violating physics in correlated top quark pairs on top of the test of quantum mechanics [62]. This chapter presents the first sensitivity study for quantum discord in top quark pairs in the dileptonic decay channel of the $t\bar{t}$ system at the ATLAS experiment. All results shown are expected sensitivities based on simulations. No data has been considered yet.

7.1. Event Selection

For the selection of dileptonic $t\bar{t}$ events, the events have to fulfil the following requirements on detector-level:

- exactly one electron and one muon with opposite sign electric charge and with $p_T \geq 15$ GeV,
- at least one trigger-matched lepton with $p_T \geq 25/27/28$ GeV (for 2015 + 16/17/18, respectively),
- at least two jets with $p_T \geq 25$ GeV,
- at least one b -tagged jet using the 85% efficiency working point of DL1r.

7.2. Analysis Strategy

The quantum discord of the top quark in the $t\bar{t}$ system is defined in Equation (2.34) with an extended explanation given in Chapter 2.3.2. The spin density matrix ρ of the system necessary for calculating the discord is given by Equation (2.7). Experimentally,

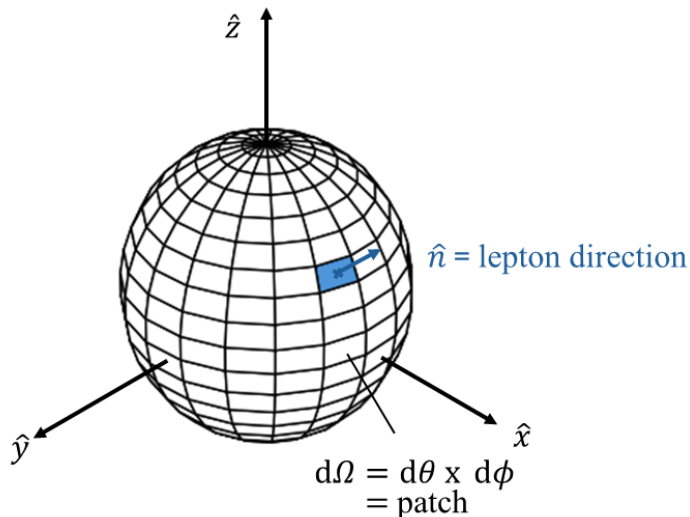


Figure 7.1.: Visualisation of the discretisation of the kinematics of the lepton in ϕ and θ . The vector \hat{n} is the vector of the lepton direction used to define the patches.

the elements of the spin density matrix can be determined from the angular distributions, $\cos \theta_i^\pm$ and $\cos \theta_i^+ \cos \theta_j^-$ for $i, j = x, y, z$, as described by Equation (2.8) and (2.10).

7.2.1. Calculation of Discord

The most challenging part of the discord calculation of the top quark is the minimisation over the quantum states of the anti-top quark. In Equation (2.34), the minimisation is performed over a discrete set of quantum states, described by the \hat{n} -vectors. In a laser-type experiment, the measurement can be repeated multiple times with the same choice of \hat{n} , as done in [132] with 1000 different \hat{n} -vectors. In contrast, the process is inherently random for top quark pairs, meaning the same \hat{n} -vector cannot be measured multiple times. Instead, an ensemble of events can be defined as a patch where the \hat{n} -vectors roughly align, depending on the size of the patch. An illustration can be seen in Figure 7.1.

For the minimisation, the quantum state of the anti-top quark is fixed and the induced polarisation on the top quark is measured. By fixing the spin state of the anti-top quark, the spin correlations between the top and anti-top quark vanish. To characterise the quantum states of the anti-top quark, the kinematics of the charged lepton coming from the anti-top quark in the rest frame of the anti-top quark are used as the charged lepton functions as the spin analyser. From this sphere of the kinematics of the lepton, the patches are defined in the ϕ^- and θ^- of the charged lepton in the range of $[-\pi, \pi]$ and

$[0, \pi]$, respectively. The number of patches is an experimental parameter that needs to be optimised with respect to the sensitivity to discord. The \hat{n} vector is taken as the vector pointing to the centre of the patch in the equation given above. Then, the polarisations $B_{\hat{n}}^+$ are measured in each patch via the relation described earlier, while for the polarisations in the opposite direction $B_{-\hat{n}}^+$, the opposite patch is picked as $\theta^- \rightarrow \pi - \theta^-$ and $\phi^- \rightarrow \pi + \phi^-$. With this strategy, the term

$$p_{\hat{n}}S(\rho_{\hat{n}}) + p_{-\hat{n}}S(\rho_{-\hat{n}}) \quad (7.1)$$

from the definition of discord can be computed and minimised over the patches. The two opposite patches that yield the minimal value for that term together are then used to calculate the discord of the top quark along with the inclusive measurements of the spin density matrix. The same procedure can be applied to the discord of the anti-top quark. The polarisations of the top quark in the patches are shown in Figure 7.2 on the unit sphere and in the 2D $\theta - \phi$ plane. The observed shape corresponds to an induced polarisation in the $i - j$ plane for the polarisation coefficient B_k^+ for $i, j, k = \{x, y, z\}$. In Figure 7.3, the value of the term $p_{\hat{n}}S(\rho_{\hat{n}}) + p_{-\hat{n}}S(\rho_{-\hat{n}})$ that is minimised in the definition of the discord is plotted on the unit sphere of the kinematic of the charged lepton. It can be seen that the term is symmetric around the z -axis.

The uncertainty of the calculated discord can be estimated by propagating the uncertainty of the input quantities through the construction of the spin density matrices and the calculation of the Von Neumann entropy. The detailed derivations can be found in Appendix A. The minimisation algorithm does not take the uncertainty into account.

7. Quantum Discord in the Dileptonic Decay Channel

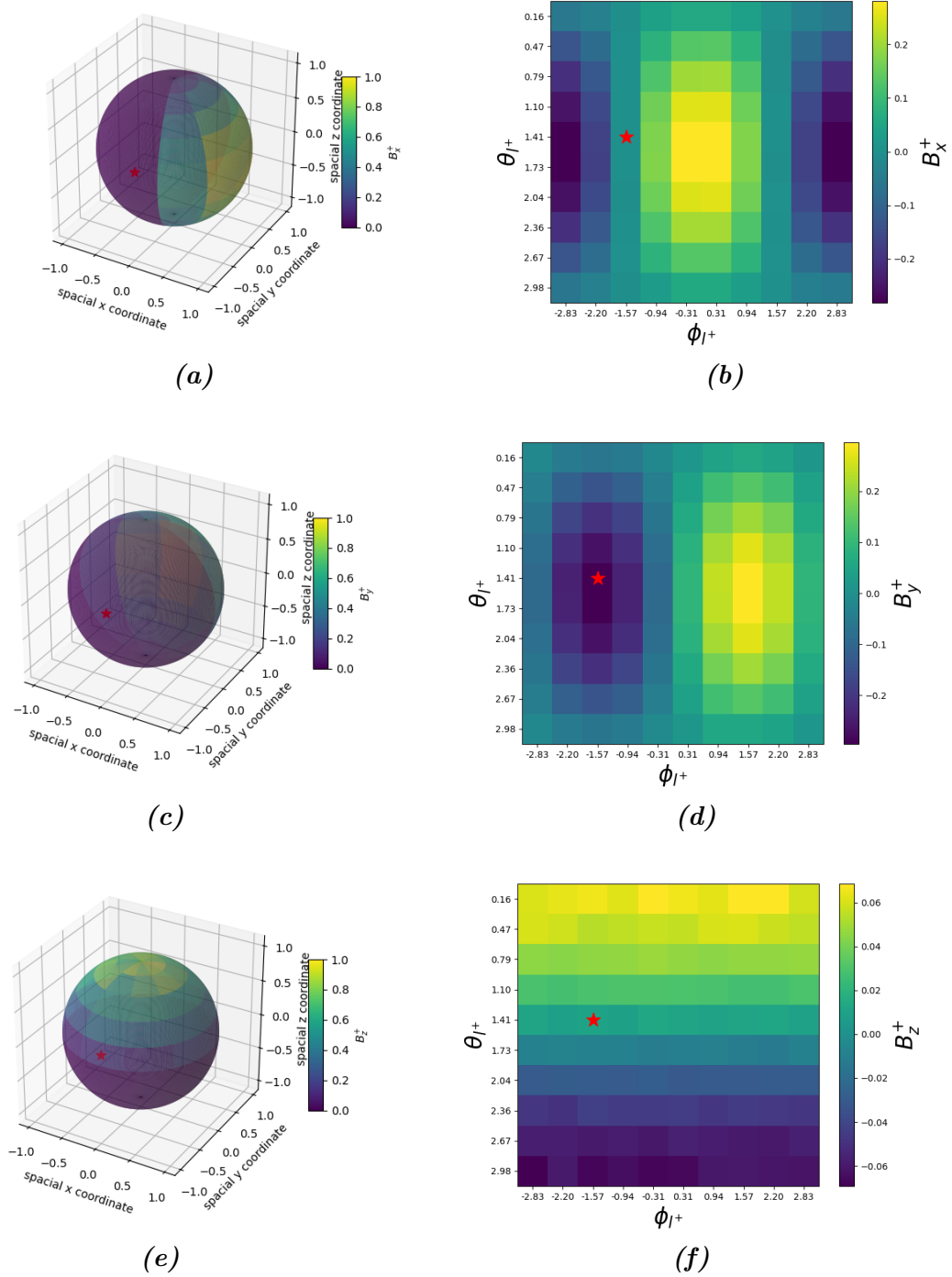


Figure 7.2.: Illustration of the top quark polarisation within an example of 100 patches in the kinematics of the charged lepton θ^-, ϕ^- on a unit sphere on parton level: **a+b)** B_x^+ , **c+d)** B_y^+ , **e+f)** B_z^+ . The red asterisk indicates the patch chosen in the minimisation.

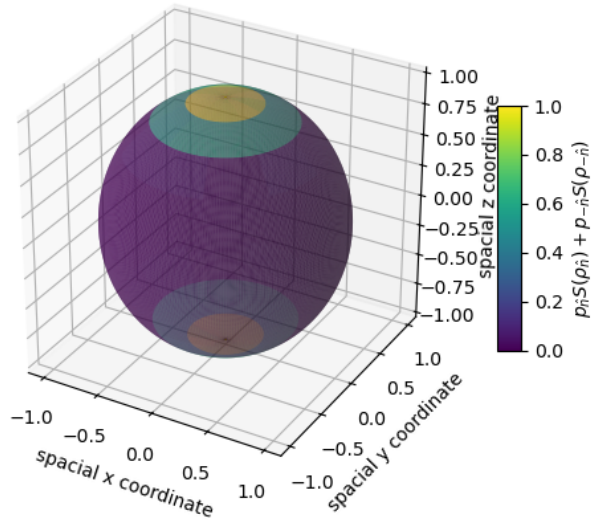


Figure 7.3.: Term $p_{\hat{n}}S(\rho_{\hat{n}}) + p_{-\hat{n}}S(\rho_{-\hat{n}})$ that has to be minimised for the definition of quantum discord in an example of 100 patches in kinematics of the charged lepton θ^- , ϕ^- on parton level. The quantity is rotational invariant around the z axis.

7.2.2. Profile Likelihood Unfolding

The measured distributions of the angular variables used to determine quantum discord are known to be distorted by experimental effects such as detector inefficiencies and resolutions. This can lead to an inaccurate representation of the underlying physics. In order to remove these detector-smearing effects and access the true distributions that show the real physics, unfolding has to be performed. Unfolding is a statistical process that can recover the underlying distribution from measured data using simulations of physics scenarios and simulated detector effects.

From the MC simulations of the physics process, the binned true (parton-level) distribution t_i is extracted. A migration matrix M_{ij} is constructed from the simulation, which shows the migration from events that are in bin j on the truth level and are reconstructed in bin i . The efficiency ϵ_i shows the fraction of events in bin i of the truth distribution which are included in the reconstructed distribution and thereby quantifies events not passing the detector-level event selection. Similarly, the acceptance a_i is defined as the fraction of events in bin i of the reconstructed distribution, which are also included in the truth distribution and shows the influence of background processes. The migration matrix, efficiency and acceptance mathematically quantify the detector effects and can be combined to the response matrix R_{ij}

$$R_{ij} = \epsilon_j M_{ij} \frac{1}{a_i}. \quad (7.2)$$

The simulated, reconstructed distribution r_i is built by folding each bin of the truth distribution with the response matrix. To each truth bin i , a normalisation factor μ_i is assigned and determined by the fit of the simulated, reconstructed distribution r_i to measured data. The unfolded distribution is then obtained by applying these normalisation factors to data.

In profile likelihood unfolding (PLU), the fit is performed via the minimisation of the negative logarithmic likelihood with a likelihood of the form

$$\mathcal{L}(\vec{n}|\vec{\mu}, \vec{\theta}) = \prod_i P(n_i|S_i(\vec{\mu}, \vec{\theta}) + B_i(\vec{\mu}, \vec{\theta})) \cdot \prod_j G(\theta_j). \quad (7.3)$$

It is built with the data distribution n_i and S_i, B_i , which are the signal and background distributions from the simulation. The contents of the bins are assumed to be Poisson distributed. Consequently, the term $P(n_i|S_i(\vec{\mu}, \vec{\theta}) + B_i(\vec{\mu}, \vec{\theta}))$ describes the Poisson distribution with the expectation value based on the simulation to yield the measured data.

The systematic uncertainties enter the likelihood via Gaussian constraint terms of the nuisance parameters θ with an expectation value of $\mu = 0$ and standard deviation of $\sigma = 1$. Any deviation from that constraint term leads to a penalty in the maximisation of the likelihood, since the initial estimations of the systematic uncertainties stem from dedicated studies (see Chapter 5). If the value of the expectation is still changed in the profile likelihood fit ("pull") or the value for the standard deviation ("constraint"), the origin of that deviation has to be well understood.

In this thesis, only Asimov fits are performed using simulated pseudo-data, called Asimov-data, instead of real data. Therefore, all normalisation factors are strictly $\mu_i = 1$.

7.2.3. Extraction of Spin Polarisation Coefficients

For the calculation of discord, the parameter of interest is not the cross-section and the absolute bin yields of the distribution, as determined per default by the PLU. Instead, the polarisation coefficients, B_i^\pm , need to be obtained from the $\cos\theta_i^\pm$ distributions, as described in Chapter 2.2. The differential cross-sections of $\cos\theta_i^\pm$ are linear in the polarisation coefficients, as shown in Equation (2.8), which can be used to access the coefficients while unfolding.

The B_i^\pm coefficients can be extracted via the PLU by reparameterising the normalisation factors μ_j for the bins $j = \{1, \dots, N_{\text{bins}}\}$. Using $\cos\theta_i^\pm = x$ and $\frac{1}{\sigma} \frac{d\sigma}{dx} = P(x, B^\pm) = \frac{1}{2}(1 \pm B^\pm x)$, the following relation holds for the unfolded bin contents N_j

$$N_j = N_{\text{tot}} \int_{x_{\text{min}}^j}^{x_{\text{max}}^j} P(x, B^\pm) dx = \mu_j y_j, \quad (7.4)$$

using the normalisation factors μ_j and the truth-level bin yields y_j . A new normalisation factor μ_{tot} can be introduced to scale the total number of unfolded events $N_{\text{tot}} = \mu_{\text{tot}} y_{\text{tot}}$, again with an expected value of $\mu_{\text{tot}} = 1$. Instead of N_{bins} degrees of freedom, now only two (B^\pm, μ_{tot}) are used. Consequently, every normalisation factor for every bin can be reparameterised as

$$\Rightarrow \mu_j = \mu_{\text{tot}} y_{\text{tot}} \frac{1}{2} \left(x_{\text{max}}^j - x_{\text{min}}^j \pm B^\pm \cdot \frac{1}{2} \left((x_{\text{max}}^j)^2 - (x_{\text{min}}^j)^2 \right) \right) / y_j \quad (7.5)$$

and the polarisation coefficients can be extracted using normalisation factors of the profile likelihood unfolding.

The coefficients of the spin correlation matrix are extracted in a slightly different way

7. Quantum Discord in the Dileptonic Decay Channel

from the distributions of the composite $\cos \theta_i^+ \cos \theta_i^-$ observables. The normalisation factor of the first bin is redefined in order to determine the mean of the distribution. Using $\cos \theta_i^+ \cos \theta_i^- = x$, the redefinition follows:

$$\langle x \rangle = \frac{\sum_{i=1}^{N_{\text{bins}}} x_i \cdot y_i \mu_i}{\sum_{i=1}^{N_{\text{bins}}} y_i \mu_i}, \quad (7.6)$$

$$\mu_1 = \frac{\sum_{i=2}^{N_{\text{bins}}} (x_i - \langle x \rangle) \cdot y_i \cdot \mu_i}{(\langle x \rangle - x_1) \cdot y_i}. \quad (7.7)$$

The different approach is chosen because of an unstable fit behaviour if the spin correlation coefficients are extracted via the differential cross-section instead of the mean.

7.3. Sensitivity Study

The sensitivity study for quantum discord is limited to the signal modelling systematic uncertainties, described in Chapter 5, because they are known to have the most significant impact on spin sensitive $t\bar{t}$ analyses (see Chapter 6.3 and [11]). The inclusive distributions and the distributions in the patches are unfolded, and the spin density matrix elements are extracted. Ultimately, the quantum discord can be calculated for the top and anti-top quark.

7.3.1. Unfolding of Inclusive Distributions

In the inclusive case, the distributions of $\cos \theta_i^+ \cos \theta_i^-$ with $i = \{x, y, z\}$ are unfolded and the diagonal entries of the correlation matrix are extracted, as described in Chapter 7.2.3. The migration matrices are shown in Figure 7.4. They are not perfectly diagonal, which means that events are migrating from one bin on parton-level to another one on detector-level, which needs to be corrected for in the unfolding. More significant migrations can cause larger uncertainties in the unfolding. But as seen in Figure 7.5, the total uncertainty of the unfolding process is small compared to the number of selected events. The results for the spin correlation coefficients C_{ii} are

$$C_{xx} = -0.31 \pm 0.005(\text{stat.}) \pm 0.03(\text{syst.}), \quad (7.8)$$

$$C_{yy} = -0.31 \pm 0.005(\text{stat.}) \pm 0.03(\text{syst.}), \quad (7.9)$$

$$C_{zz} = -0.07 \pm 0.001(\text{stat.}) \pm 0.02(\text{syst.}), \quad (7.10)$$

which is well compatible with the expectation of $C_{xx} = C_{yy}$ in the beam basis. The results are multiple standard deviations away from zero, meaning that the spin correlation is

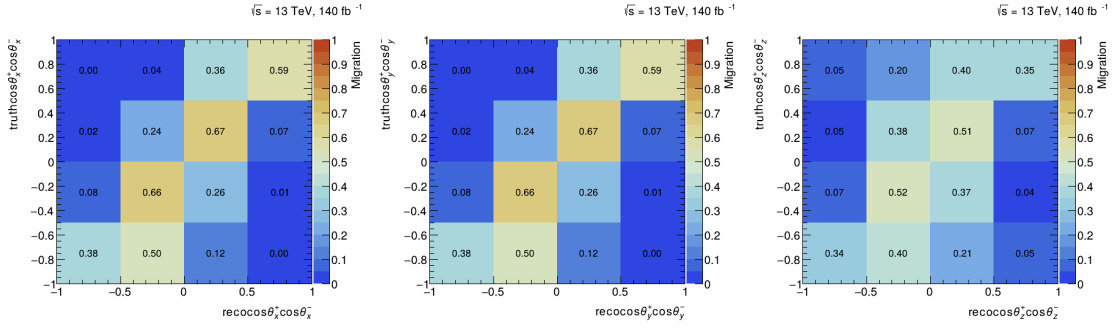


Figure 7.4.: Migration matrices for the inclusive distributions of $\cos \theta_i^+ \cos \theta_i^-$ using POWHEG+PYTHIA, used for the unfolding procedure.

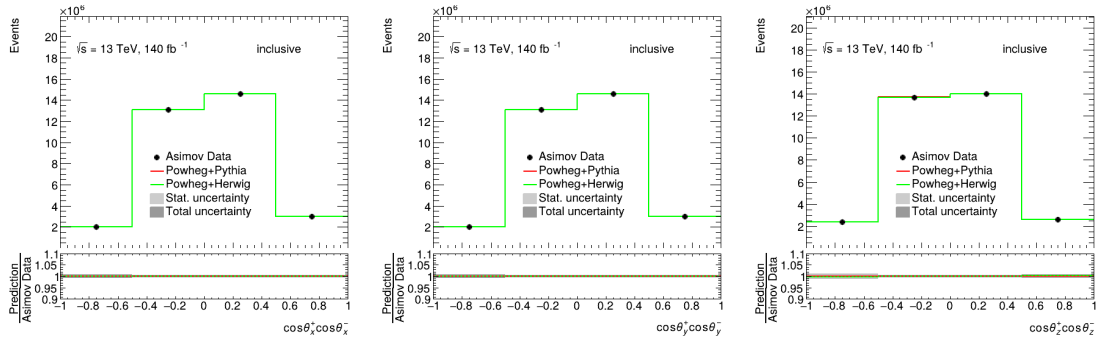


Figure 7.5.: Results of the unfolding procedure using Asimov-data. The nominal prediction using POWHEG+PYTHIA is shown, as well as the alternative predictions using POWHEG+HERWIG. The uncertainty is represented by the grey uncertainty band.

measurable with this setup. The results for the individual spin polarisation coefficients B_i^\pm are

$$B_x^+ = 0.000 \pm 0.002(\text{stat.}) \pm 0.001(\text{syst.}), \quad (7.11)$$

$$B_y^+ = 0.000 \pm 0.002(\text{stat.}) \pm 0.001(\text{syst.}), \quad (7.12)$$

$$B_z^+ = 0.000 \pm 0.003(\text{stat.}) \pm 0.001(\text{syst.}), \quad (7.13)$$

$$B_x^- = 0.000 \pm 0.002(\text{stat.}) \pm 0.001(\text{syst.}), \quad (7.14)$$

$$B_y^- = 0.000 \pm 0.002(\text{stat.}) \pm 0.001(\text{syst.}), \quad (7.15)$$

$$B_z^- = 0.000 \pm 0.003(\text{stat.}) \pm 0.001(\text{syst.}), \quad (7.16)$$

and within uncertainties compatible with zero, which matches the expectation of unpolarised top quark production at leading order.

7. Quantum Discord in the Dileptonic Decay Channel

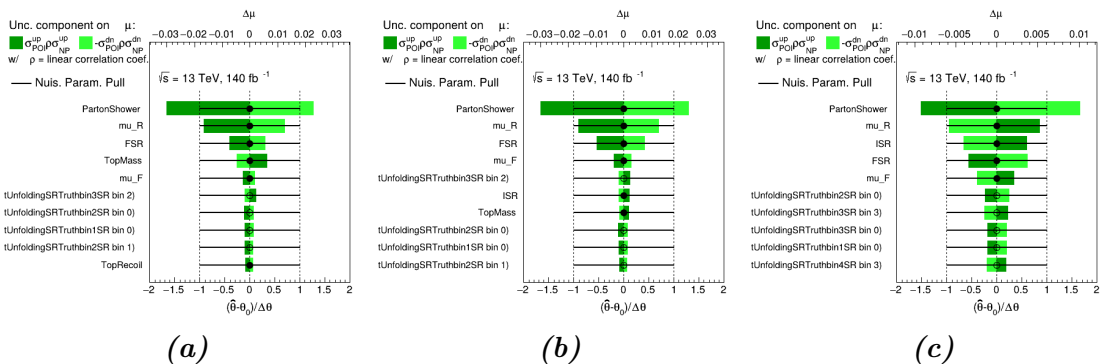


Figure 7.6.: Ranking of the contribution of the nuisance parameters to the total uncertainty of the parameter of interest **a)** C_{xx} , **b)** C_{yy} and **c)** C_{zz} . The values are extracted from the off-diagonal elements of the fit covariance matrix, which correspond to the covariance of the nuisance parameter with the parameter of interest.

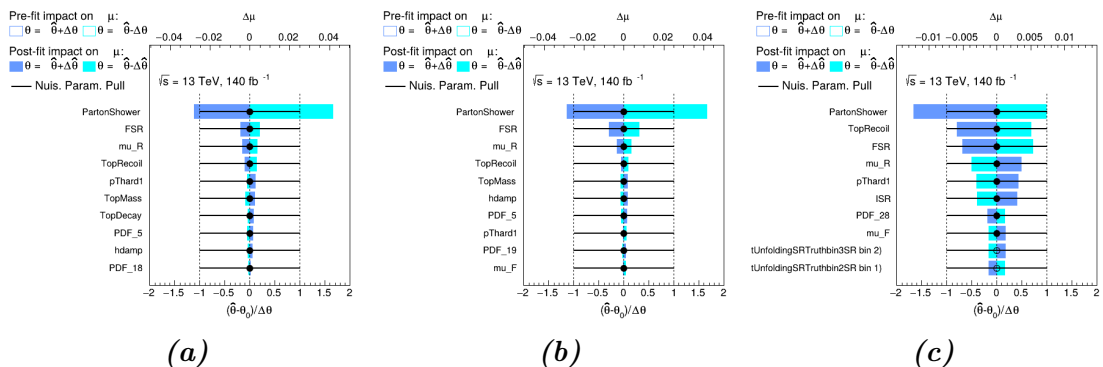


Figure 7.7.: Ranking of the impact of the nuisance parameters on the parameter of interest **a)** C_{xx} , **b)** C_y and **c)** C_{zz} . The impact is obtained by running multiple fits and fixing one of the nuisance parameters to ± 1 of its pre- and post-fit values.

In Figure 7.6, the components of the uncertainty on the parameter of interest (here the spin correlation coefficient) are ranked according to their contribution to the total uncertainty. The uncertainty decomposition is based on the off-diagonal elements of the covariance matrix of the fit, which corresponds to the covariance of the nuisance parameter and the parameter of interest [133]. The systematic uncertainty concerning the parton shower ranks high again, which is no surprise as the same effect has also been seen in the entanglement analysis. Similarly, the impact of the systematic uncertainties is ranked in Figure 7.7, and the post- and pre-fit impact is compared. The impact is obtained by running multiple fits and fixing one of the nuisance parameters to ± 1 of its pre- and post-fit values. Again, the parton shower systematic uncertainty is the dominating one. The post- and pre-fit impacts match the systematic uncertainties with the highest impacts as

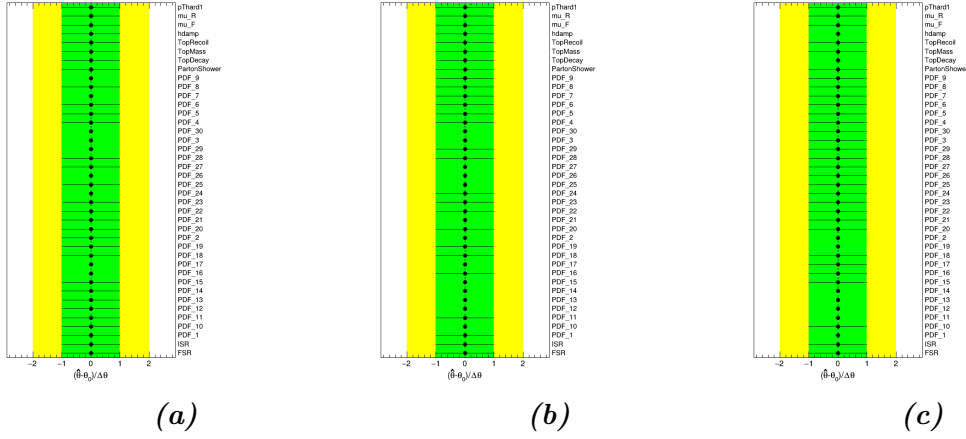


Figure 7.8.: Constraints for the nuisance parameters for a) $\cos\theta_x^+ \cos\theta_x^-$, b) $\cos\theta_y^+ \cos\theta_y^-$ and c) $\cos\theta_z^+ \cos\theta_z^-$.

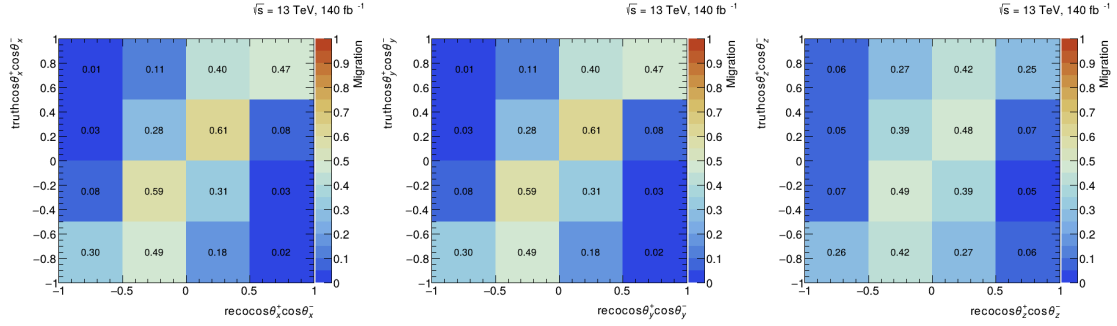


Figure 7.9.: Migration matrices for the inclusive distributions of $\cos\theta_i^+ \cos\theta_i^-$ using POWHEG+HERWIG, used as a systematic variation for the unfolding procedure. The comparison with Figure 7.4 shows a significant deviation in the diagonality of the matrices.

there are no constraints. But as can be seen in Figure 7.8, the nuisance parameters for some of the variations of the parton distribution functions are strongly constrained.

The high impact on and contribution to the uncertainty of the parameter of interest can be understood from the comparison of the migration matrices of POWHEG+PYTHIA in Figure 7.4 and POWHEG+HERWIG in Figure 7.9. The migration matrix for POWHEG+HERWIG is significantly less diagonal than the one for POWHEG+PYTHIA. Even though the parton-level distributions of POWHEG+PYTHIA and POWHEG+HERWIG match well in Figure 7.5, due to the large migration differences, the detector-level distributions cannot match well. This can also be seen in Figure 7.10, which shows the systematic shift for the unfolding distribution per truth bin. In a significant amount of bins, the deviations exceed 100%. The reason for that lies in the fact that the large deviation for the two parton shower genera-

7. Quantum Discord in the Dileptonic Decay Channel

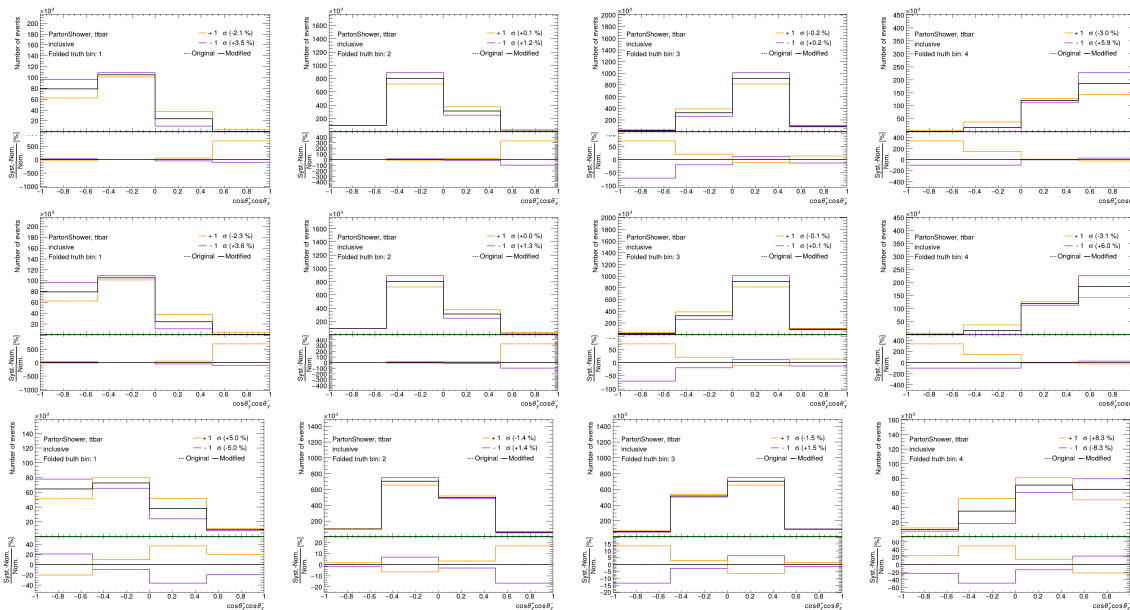


Figure 7.10.: Comparison of the unfolding distributions per truth-bin for the nominal POWHEG+PYTHIA and the systematic variation POWHEG+HERWIG. The deviation exceeds in some bins the 100 %, which causes a large impact on the parameter of interest.

tors only appears at particle-level and is then propagated to detector-level. The origin of this difference is presented in more detail for the observation of quantum entanglement in the dileptonic decay channel in [11].

The results presented are still preliminary, and the input distributions need to be studied in further detail to solve the issues mentioned.

7.3.2. Unfolding of Distributions in Patches

The unfolding of the polarisation distributions in the kinematic patches is done independently for the top and anti-top quark as they have independently defined patches. In the following, the focus is on the results for the top quark, and the results for the anti-top quark can be found in Appendix B since they are similar.

In the patches of the top quark, the distributions of $\cos \theta_i^+$ with $i = \{x, y, z\}$ are unfolded and the spin polarisations B_i^+ are extracted, as described in Chapter 7.2.3. To optimise the patch size, a trade-off of statistics per patch and the bias due to the patch size had to be made while considering the influence of the systematic uncertainties. The configuration which maximised the sensitivity to quantum discord was found to be $18 \times 18 = 324$

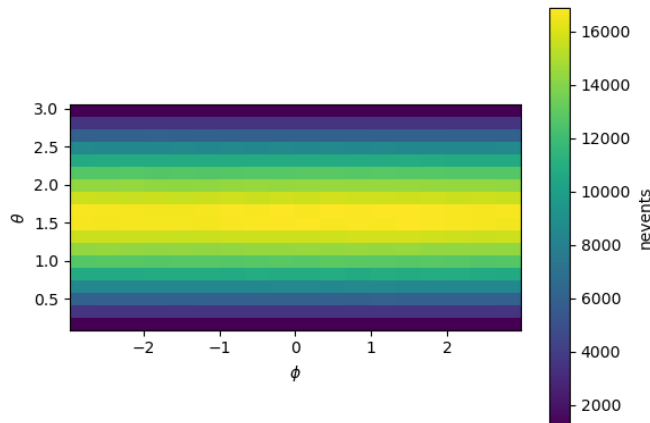


Figure 7.11.: Number of expected events per patch. The number of events is independent of ϕ^- and has a maximum around $\theta \approx \pi/2$, the region relevant for quantum discord.

patches. This means that the range $[0, \pi]$ of θ^- was divided in 18 equidistant bins and so was the range $[-\pi, \pi]$ of ϕ^- . As shown in parton-level studies in Figure 7.2, the results differ highly for the polarisation directions and position on the sphere. However, as Figure 7.3 demonstrates, the minimisation quantity is symmetric around the z -axis, and the minimum lies around $\theta \approx \pi/2$. This coincides with the region with the maximal number of expected events, as shown in Figure 7.11.

In the following, only the results for the specific patch picked in the minimisation are discussed, as this is the only patch directly influencing the sensitivity. The picked patch describes the region $-\pi < \phi^- < -8/9\pi$, $\pi/2 < \theta^- < 5/9\pi$. The migration matrices in this patch are shown in Figure 7.12. They are more diagonal than the inclusive ones due to the tight restrictions on the patch definition. But as seen in Figure 7.13, the total uncertainty of the unfolding process is significant compared to the number of selected events. The results for the spin polarisation coefficients B_i^+ are

$$B_x^+ = -0.30 \pm 0.02(\text{stat.}) \pm 0.05(\text{syst.}), \quad (7.17)$$

$$B_y^+ = -0.05 \pm 0.02(\text{stat.}) \pm 0.05(\text{syst.}), \quad (7.18)$$

$$B_z^+ = 0.00 \pm 0.03(\text{stat.}) \pm 0.04(\text{syst.}). \quad (7.19)$$

This means there is only a spin polarisation measurable in this patch in the x -direction, which is unsurprising when looking at Figure 7.2.

7. Quantum Discord in the Dileptonic Decay Channel

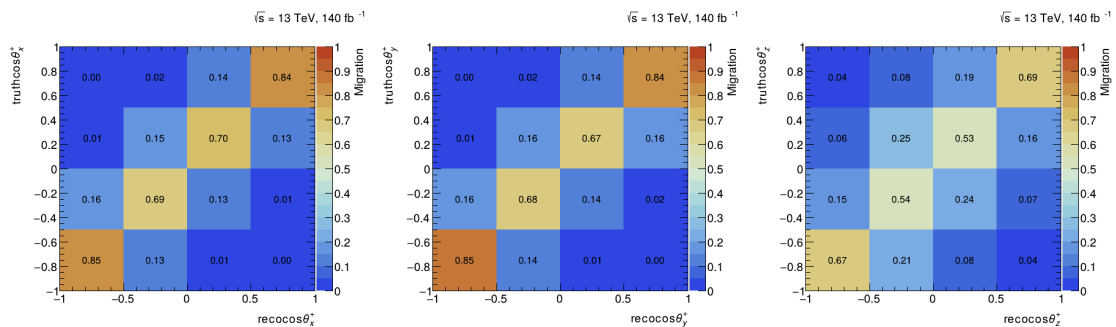


Figure 7.12.: Migration matrices for the distributions of $\cos\theta_i^+$ in the region $-\pi < \phi^- < -8/9\pi$, $\pi/2 < \theta^- < 5/9\pi$, used for the unfolding procedure.

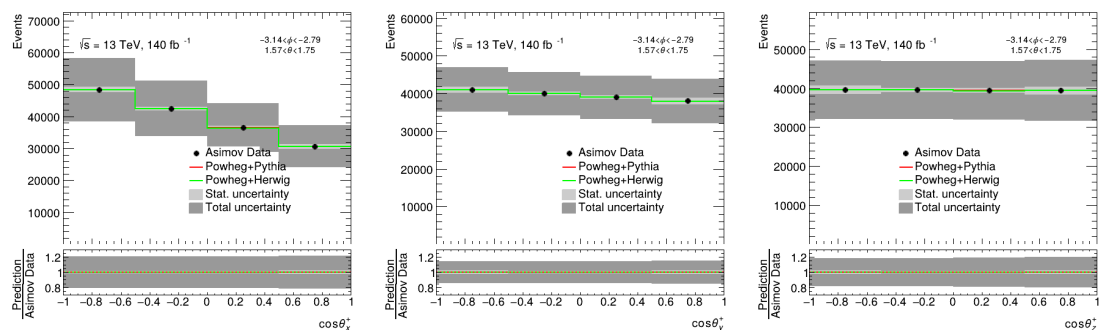


Figure 7.13.: Results of the unfolding procedure using Asimov-data, in the region $-\pi < \phi^- < -8/9\pi$, $\pi/2 < \theta^- < 5/9\pi$. The nominal prediction using POWHEG+PYTHIA is shown, as well as the alternative predictions using POWHEG+HERWIG. The uncertainty is represented by the grey uncertainty band.

The systematic uncertainties with the highest contributions to the uncertainty on the parameter of interest (here the spin polarisation coefficients) are ranked in Figure B.3. There are no visible constraints on any nuisance parameters. The systematic uncertainties concerning the parton distribution contribute the most to the uncertainty on the spin coefficient B_x^+ in the patch. A high impact of these systematics on spin-sensitive coefficients has already been observed in the analysis of entanglement in the dileptonic decay channel [11]. The comparison of the unfolding distributions per truth bin can be seen in Figure 7.15.

Ultimately, the quantum discord can be calculated for the top quark and anti-top quark,

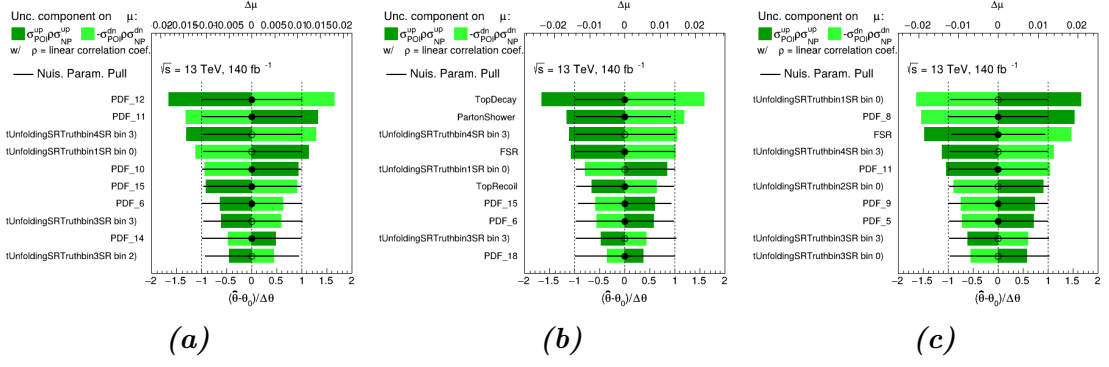


Figure 7.14.: Ranking of the contribution of the nuisance parameters to the total uncertainty of the parameter of interest **a)** B_x^+ , **b)** B_y^+ and **c)** B_z^+ , in the region $-\pi < \phi^- < -8/9\pi$, $\pi/2 < \theta^- < 5/9\pi$. The values are extracted from the off-diagonal elements of the fit covariance matrix, which correspond to the covariance of the nuisance parameter with the parameter of interest.

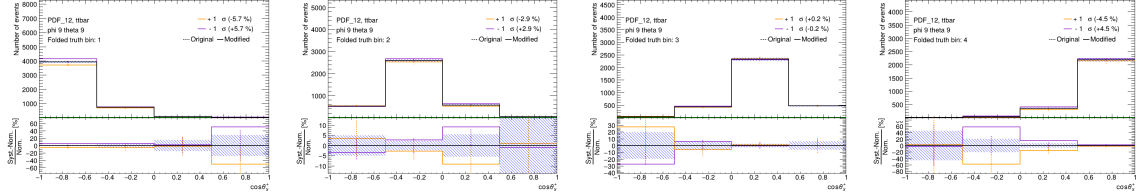


Figure 7.15.: Comparison of the unfolding distributions per truth-bin for the nominal distribution and the one using the twelfth variation of the parton distribution functions.

which yields

$$\mathcal{D}_t = 0.07 \pm 0.019(\text{stat.}) \pm 0.04(\text{syst.}), \quad (7.20)$$

$$\mathcal{D}_{\bar{t}} = 0.07 \pm 0.019(\text{stat.}) \pm 0.04(\text{syst.}). \quad (7.21)$$

The resulting significances with respect to zero are

$$Z(\mathcal{D}_t) = 1.7 \sigma, \quad (7.22)$$

$$Z(\mathcal{D}_{\bar{t}}) = 1.7 \sigma, \quad (7.23)$$

which is lower than the 3σ threshold for evidence of quantum discord. Only considering the statistical uncertainty, the significances exceed the 3σ threshold. This motivates further studies of quantum discord, especially studies of the reconstruction of the dileptonic decay channel of the top quark system, to reduce the impact of systematic uncertainties.

8. Conclusion and Outlook

The analysis of quantum entanglement in top quark pairs is an important contribution to the research of quantum information at high-energy colliders like the LHC. It holds potential for studying new, pseudo-bound particles like toponium. The measurement of quantum entanglement in the dileptonic decay channel of the $t\bar{t}$ system by ATLAS [11] is the first measurement of quantum entanglement in top quark pairs. It shows a surprising discrepancy between the MC prediction and the measured data. The measurement by CMS in the same channel hints that the discrepancy can be resolved by considering contributions from the pseudo-bound toponium particle [12]. As this thesis shows, the measurements in the dileptonic channel can be supported by measurements in the semileptonic decay channel. The semileptonic decay channel requires more sophisticated reconstruction tools and an extended study of the systematic uncertainties, but as the results obtained in this thesis demonstrate, it is a feasible and sensitive channel to support the measurements in the dileptonic channel based on the MC predictions. For both decay channels, a study of the contribution of toponium would be interesting in order to compare it to the results obtained by CMS. If the results obtained by the semileptonic and dileptonic decay channels could be combined, the sensitivity could be further enhanced. In a future study of quantum entanglement in top quark pairs, the high $m_{t\bar{t}}$ regime provides an interesting opportunity to learn more about quantum entanglement in top quark pairs. The semileptonic analysis of CMS already demonstrated the feasibility of such a measurement in the semileptonic channel [13].

Quantum discord is a quantum property measurable in top quark pairs which might unravel CP -violating physics beyond the standard model. It is measured separately for the top quark and anti-top quark. This thesis presents the first sensitivity study for measuring quantum discord in the dileptonic channel of the top quark system. This laid the groundwork for the first measurement of quantum discord in the dileptonic decay channel. The analysis is limited by systematic uncertainties. The systematic uncertainties could be reduced using novel top quark reconstruction methods and selecting well-reconstructible events, similar to the entanglement analysis in the semileptonic decay channel. One can-

8. Conclusion and Outlook

didate is the ν^2 -flows method that uses normalising flows to reconstruct multi-neutrino final states [134]. The paper demonstrates how, for a double differential observable sensitive to the $t\bar{t}$ spin correlation, the statistical precision with ν^2 -flows improved compared to classical methods. Moreover, ν^2 -flows is able to reconstruct the $t\bar{t}$ system without enforcing constraints on the top quark and W boson mass, as the Ellipse and Sonnenschein methods do.

The measurements of quantum entanglement and quantum discord open the doors to future studies of quantum information at the ATLAS experiment. They hold potential for new observations of physics beyond the standard model [14]. The results from this thesis can be used to test data for the predictions based on simulations.

Bibliography

- [1] E. Schrödinger, *Discussion of Probability Relations between Separated Systems*, Math. Proc. Camb. Philos. Soc. **31(4)**, 555 (1935)
- [2] A. Einstein, M. Born, H. Born, *The Born-Einstein Letters: Correspondence Between Albert Einstein and Max and Hedwig Born from 1916-1955, with Commentaries by Max Born*, Macmillan (1971)
- [3] A. Aspect, P. Grangier, G. Roger, *Experimental Realization of Einstein-Podolsky-Rosen-Bohm Gedankenexperiment: A New Violation of Bell's Inequalities*, Phys. Rev. Lett. **49**, 91 (1982)
- [4] E. Hagley, et al., *Generation of Einstein-Podolsky-Rosen Pairs of Atoms*, Phys. Rev. Lett. **79**, 1 (1997)
- [5] M. Steffen, et al., *Measurement of the Entanglement of Two Superconducting Qubits via State Tomography*, Science **313(5792)**, 1423 (2006)
- [6] Belle Collaboration, *Measurement of EPR-type flavour entanglement in $\Upsilon(4S) \rightarrow B0$ anti- $B0$ decays*, Phys. Rev. Lett. **99**, 131802 (2007)
- [7] J. A. Formaggio, et al., *Violation of the Leggett-Garg Inequality in Neutrino Oscillations*, Phys. Rev. Lett. **117**, 050402 (2016)
- [8] B. Hensen, et al., *Loophole-free Bell inequality violation using electron spins separated by 1.3 kilometres*, Nature **526(7575)** (2015)
- [9] D. Bouwmeester, et al., *Experimental quantum teleportation*, Nature **390(6660)**, 575 (1997)
- [10] *The Nobel Prize in Physics 2022.*, <https://www.nobelprize.org/prizes/physics/2022/summary/>, 05 Apr 2024.
- [11] ATLAS Collaboration, *Observation of quantum entanglement with top quarks at the ATLAS detector*, Nature **633**, 542 (2024)

Bibliography

- [12] CMS Collaboration, *Observation of quantum entanglement in top quark pair production in proton-proton collisions at $\sqrt{s} = 13$ TeV* (2024), 2406.03976
- [13] CMS Collaboration, *Measurements of polarization and spin correlation and observation of entanglement in top quark pairs using lepton+jets events from proton-proton collisions at $\sqrt{s} = 13$ TeV* (2024), 2409.11067
- [14] F. Maltoni, et al., *Quantum detection of new physics in top-quark pair production at the LHC*, JHEP **99** (2024)
- [15] A. J. Barr, et al., *Quantum entanglement and Bell inequality violation at colliders* (2024), 2402.07972
- [16] H. Ollivier, W. H. Zurek, *Quantum Discord: A Measure of the Quantumness of Correlations*, Phys. Rev. Lett. **88**, 017901 (2001)
- [17] R. Auccaise, et al., *Experimentally Witnessing the Quantumness of Correlations*, Phys. Rev. Lett. **107**, 070501 (2011)
- [18] G. Passante, et al., *Experimental detection of nonclassical correlations in mixed-state quantum computation*, Phys. Rev. A **84**, 044302 (2011)
- [19] G. H. Aguilar, et al., *Experimental Estimate of a Classicality Witness via a Single Measurement*, Phys. Rev. Lett. **108**, 063601 (2012)
- [20] S. Hosseini, et al., *Experimental verification of quantum discord in continuous-variable states*, J. Phys. B **47(2)**, 025503 (2014)
- [21] S. L. Glashow, *Partial Symmetries of Weak Interactions*, Nucl. Phys. **22**, 579 (1961)
- [22] S. Weinberg, *A Model of Leptons*, Phys. Rev. Lett. **19**, 1264 (1967)
- [23] A. Salam, *Weak and Electromagnetic Interactions*, ed. Nobel Symposium No. 8 (Almqvist & Wiksell, Stockholm, 1968)
- [24] H. D. Politzer, *Reliable Perturbative Results for Strong Interactions*, Phys. Rev. Lett. **30**, 1346 (1973)
- [25] H. D. Politzer, *Asymptotic Freedom: An Approach to Strong Interactions*, Phys. Rept. **14**, 129 (1974)
- [26] D. J. Gross, F. Wilczek, *Asymptotically Free Gauge Theories*, Phys. Rev. D **8**, 3633 (1973)

- [27] E. Noether, *Invariante Variationsprobleme*, Nachr. d. König. Gesellsch. d. Wiss. zu Göttingen **1918**, 235 (1918)
- [28] P. W. Higgs, *Broken Symmetries and the Masses of Gauge Bosons*, Phys. Rev. Lett. **13**, 508 (1964)
- [29] F. Englert, R. Brout, *Broken Symmetry and the Mass of Gauge Vector Mesons*, Phys. Rev. Lett. **13**, 321 (1964)
- [30] ATLAS Collaboration, *Observation of a new particle in the search for the Standard Model Higgs boson with the ATLAS detector at the LHC*, Phys. Lett. B **716(1)**, 1 (2012)
- [31] CMS Collaboration, *Observation of a new boson at a mass of 125 GeV with the CMS experiment at the LHC*, Phys. Lett. B **716(1)**, 30 (2012)
- [32] J. E. Augustin, et al., *Discovery of a Narrow Resonance in e^+e^- Annihilation*, Phys. Rev. Lett. **33**, 1406 (1974)
- [33] J. J. Aubert, et al., *Experimental Observation of a Heavy Particle J* , Phys. Rev. Lett. **33**, 1404 (1974)
- [34] L. M. Lederman, *The Upsilon Particle*, Sci. Am. **239(4)**, 72 (1978)
- [35] DØ Collaboration, *Search for High Mass Top Quark Production in $p\bar{p}$ Collisions at $\sqrt{s} = 1.8$ TeV*, Phys. Rev. Lett. **74**, 2422 (1995)
- [36] CDF Collaboration, *Observation of Top Quark Production in $p\bar{p}$ Collisions with the Collider Detector at Fermilab*, Phys. Rev. Lett. **74**, 2626 (1995)
- [37] B. Andersson, et al., *Parton fragmentation and string dynamics*, Phys. Rep. **97(2)**, 31 (1983)
- [38] B. Andersson, *The Lund Model*, volume 7 of *Cambridge Monographs on Particle Physics, Nuclear Physics and Cosmology*, Cambridge University Press (2023)
- [39] T. Sjöstrand, et al., *PYTHIA*, Comput. Phys. Commun. **135**, 238 (2001)
- [40] G. C. Fox, S. Wolfram, *A model for parton showers in QCD*, Nucl. Phys. B **168(2)**, 285 (1980)
- [41] R. D. Field, S. Wolfram, *A QCD model for e^+e^- annihilation*, Nucl. Phys. B **213(1)**, 65 (1983)

Bibliography

- [42] G. Marchesini, et al., *HERWIG*, Comput. Phys. Commun. **67**, 465 (1992)
- [43] G. Corcella, et al., *HERWIG 6: an event generator for hadron emission reactions with interfering gluons (including supersymmetric processes)*, JHEP **0101**, 010 (2001)
- [44] N. Cabibbo, *Unitary Symmetry and Leptonic Decays*, Phys. Rev. Lett. **10**, 531 (1963)
- [45] M. Kobayashi, T. Maskawa, *CP Violation in the Renormalizable Theory of Weak Interaction*, Prog. Theor. Phys. **49**, 652 (1973)
- [46] Particle Data Group, *Review of Particle Physics*, PTEP **2023**, 083C01 (2023)
- [47] *Standard Atomic Weights of 14 Chemical Elements Revised*, Chem. Int. **40(4)**, 23 (2018)
- [48] I. I. Bigi, et al., *Production and Decay Properties of Ultra-Heavy Quarks*, Phys. Lett. B **181**, 157 (1986)
- [49] G. Mahlon, S. J. Parke, *Spin Correlation Effects in Top Quark Pair Production at the LHC*, Phys. Rev. D **81**, 074024 (2010)
- [50] K. Hagiwara, Y. Sumino, H. Yokoya, *Bound-state effects on top quark production at hadron colliders*, Phys. Lett. B **666(1)**, 71â76 (2008)
- [51] Y. Kiyo, et al., *Top-quark pair production near threshold at LHC*, Eur. Phys. J. C **60(3)**, 375 (2009)
- [52] Y. Sumino, H. Yokoya, *Bound-state effects on kinematical distributions of top quarks at hadron colliders*, JHEP **2010(9)** (2010)
- [53] W.-L. Ju, et al., *Top quark pair production near threshold: single/double distributions and mass determination*, JHEP **2020(6)** (2020)
- [54] B. Fuks, et al., *Signatures of toponium formation in LHC run 2 data*, Phys. Rev. D **104**, 034023 (2021)
- [55] A. Czarnecki, M. Jezabek, J. H. Kühn, *Lepton spectra from decays of polarized top quarks*, Nucl. Phys. B **351(1)**, 70 (1991)
- [56] M. Jezabek, J. Kühn, *V - A tests through leptons from polarised top quarks*, Phys. Lett. B **329(2)**, 317 (1994)

- [57] A. Brandenburg, Z. Si, P. Uwer, *QCD-corrected spin analysing power of jets in decays of polarized top quarks*, Phys. Lett. B **539(3)**, 235 (2002)
- [58] F. Hubaut, et al., *ATLAS sensitivity to top quark and W boson polarization in $t\bar{t}$ events*, Eur. Phys. J. C **44(S1)**, 13 (2005)
- [59] B. Tweedie, *Better hadronic top quark polarimetry*, Phys. Rev. D **90**, 094010 (2014)
- [60] Z. Dong, et al., *Entanglement and Bell inequalities with boosted $t\bar{t}$* , Phys. Rev. D **109**, 115023 (2024)
- [61] Y. Afik, J. R. M. de Nova, *Entanglement and quantum tomography with top quarks at the LHC*, Eur. Phys. J. Plus **136(9)** (2021)
- [62] Y. Afik, J. R. M. de Nova, *Quantum Discord and Steering in Top Quarks at the LHC*, Phys. Rev. Lett. **130**, 221801 (2023)
- [63] H. M. Wiseman, S. J. Jones, A. C. Doherty, *Steering, Entanglement, Nonlocality, and the Einstein-Podolsky-Rosen Paradox*, Phys. Rev. Lett. **98**, 140402 (2007)
- [64] J. S. Bell, *On the Einstein Podolsky Rosen paradox*, Phys. Phys. Fiz. **1**, 195 (1964)
- [65] A. Peres, *Separability Criterion for Density Matrices*, Phys. Rev. Lett. **77**, 1413 (1996)
- [66] P. Horodecki, *Separability criterion and inseparable mixed states with positive partial transposition*, Phys. Lett. A **232(5)**, 333 (1997)
- [67] W. K. Wootters, *Entanglement of Formation of an Arbitrary State of Two Qubits*, Phys. Rev. Lett. **80**, 2245 (1998)
- [68] G. L. Kane, G. A. Ladinsky, C. P. Yuan, *Using the top quark for testing standard-model polarization and CP predictions*, Phys. Rev. D **45**, 124 (1992)
- [69] W. Bernreuther, A. Brandenburg, *Tracing CP violation in the production of top quark pairs by multiple TeV proton-proton collisions*, Phys. Rev. D **49**, 4481 (1994)
- [70] W. Bernreuther, et al., *Top-Quark Spin Correlations at Hadron Colliders: Predictions at Next-to-Leading Order QCD*, Phys. Rev. Lett. **87**, 242002 (2001)
- [71] W. Bernreuther, et al., *Top quark pair production and decay at hadron colliders*, Nucl. Phys. B **690** (2004)

Bibliography

- [72] W. Bernreuther, D. Heisler, Z.-G. Si, *A set of top quark spin correlation and polarization observables for the LHC: Standard Model predictions and new physics contributions*, JHEP **2015(12)**, 1 (2015)
- [73] DØ Collaboration, *Measurement of Spin Correlation in $t\bar{t}$ Production Using a Matrix Element Approach*, Phys. Rev. Lett. **107**, 032001 (2011)
- [74] DØ Collaboration, *Measurement of spin correlation in $t\bar{t}$ production using dilepton final states*, Phys. Lett. B **702(1)**, 16 (2011)
- [75] DØ Collaboration, *Evidence for Spin Correlation in $t\bar{t}$ Production*, Phys. Rev. Lett. **108**, 032004 (2012)
- [76] DØ Collaboration, *Measurement of spin correlation between top and antitop quarks produced in $p\bar{p}$ collisions at $\sqrt{s} = 1.96$ TeV*, Phys. Lett. B **757**, 199 (2016)
- [77] CDF Collaboration, *Measurement of $t\bar{t}$ spin correlation in $p\bar{p}$ collisions using the CDF II detector at the Tevatron*, Phys. Rev. D **83**, 031104 (2011)
- [78] ATLAS Collaboration, *Observation of Spin Correlation in $t\bar{t}$ Events from pp Collisions at $\sqrt{s} = 7$ TeV Using the ATLAS Detector*, Phys. Rev. Lett. **108**, 212001 (2012)
- [79] ATLAS Collaboration, *Measurements of spin correlation in top-antitop quark events from proton-proton collisions at $\sqrt{s} = 7$ TeV using the ATLAS detector*, Phys. Rev. D **90**, 112016 (2014)
- [80] ATLAS Collaboration, *Measurement of Spin Correlation in Top-Antitop Quark Events and Search for Top Squark Pair Production in pp Collisions at $\sqrt{s} = 8$ TeV Using the ATLAS Detector*, Phys. Rev. Lett. **114**, 142001 (2015)
- [81] ATLAS Collaboration, *Measurement of the correlation between the polar angles of leptons from top quark decays in the helicity basis at $\sqrt{s} = 7$ TeV using the ATLAS detector*, Phys. Rev. D **93**, 012002 (2016)
- [82] ATLAS Collaboration, *Measurements of top quark spin observables in $t\bar{t}$ events using dilepton final states in $\sqrt{s} = 13$ TeV pp collisions with the ATLAS detector*, JHEP **2017(3)** (2017)
- [83] ATLAS Collaboration, *Measurements of top-quark pair spin correlations in the $e\mu$ channel at $\sqrt{s} = 13$ TeV using pp collisions in the ATLAS detector*, Eur. Phys. J. C **80**, 1 (2020)

- [84] CMS Collaboration, *Measurements of $t\bar{t}$ Spin Correlations and Top-Quark Polarization Using Dilepton Final States in pp Collisions at $\sqrt{s} = 7$ TeV*, Phys. Rev. Lett. **112**, 182001 (2014)
- [85] CMS Collaboration, *Measurement of spin correlations in $t\bar{t}$ production using the matrix element method in the muon+jets final state in pp collisions at $\sqrt{s} = 8$ TeV*, Phys. Lett. B **758** (2016)
- [86] CMS Collaboration, *Measurements of $t\bar{t}$ spin correlations and top quark polarization using dilepton final states in pp collisions at $\sqrt{s} = 8$ TeV*, Phys. Rev. D **93**, 052007 (2016)
- [87] CMS Collaboration, *Measurement of the top quark polarization and $t\bar{t}$ spin correlations using dilepton final states in proton-proton collisions at $\sqrt{s} = 13$ TeV*, Phys. Rev. D **100**, 072002 (2019)
- [88] C. Shannon, *A Mathematical Theory of Communication*, Bell Labs Tech. J. **27** (1948)
- [89] F. Bloch, *Nuclear Induction*, Phys. Rev. **70**, 460 (1946)
- [90] S. Luo, *Quantum discord for two-qubit systems*, Phys. Rev. A **77**, 042303 (2008)
- [91] L. Evans, P. Bryant, *LHC Machine*, JINST **3(08)**, S08001 (2008)
- [92] ATLAS Collaboration, *The ATLAS Experiment at the CERN Large Hadron Collider*, JINST **3(08)**, S08003 (2008)
- [93] ALICE Collaboration, *The ALICE Experiment at the CERN Large Hadron Collider*, JINST **3(08)**, S08002 (2008)
- [94] CMS Collaboration, *The CMS Experiment at the CERN Large Hadron Collider*, JINST **3(08)**, S08004 (2008)
- [95] LHCb Collaboration, *The LHCb Experiment at the CERN Large Hadron Collider*, JINST **3(08)**, S08005 (2008)
- [96] ATLAS Collaboration, *Luminosity determination in pp collisions at $\sqrt{s} = 13$ TeV using the ATLAS detector at the LHC*, Eur. Phys. J. C **83** (2023)
- [97] P. Nason, *A new method for combining NLO QCD with shower Monte Carlo algorithms*, JHEP **2004(11)**, 040 (2004)

Bibliography

- [98] S. Frixione, G. Ridolfi, P. Nason, *A positive-weight next-to-leading-order Monte Carlo for heavy flavour hadroproduction*, JHEP **2007(09)**, 126 (2007)
- [99] S. Frixione, P. Nason, C. Oleari, *Matching NLO QCD computations with parton shower simulations: the POWHEG method*, JHEP **2007(11)**, 070 (2007)
- [100] S. Alioli, et al., *A general framework for implementing NLO calculations in shower Monte Carlo programs: the POWHEG BOX*, JHEP **2010(6)** (2010)
- [101] R. D. Ball, et al., *Parton distributions for the LHC run II*, JHEP **2015(4)** (2015)
- [102] T. Sjöstrand, et al., *An introduction to PYTHIA 8.2*, Comput. Phys. Commun. **191**, 159 (2015)
- [103] R. D. Ball, et al., *Parton distributions with LHC data*, Nucl. Phys. B **867(2)**, 244 (2013)
- [104] ATLAS Collaboration, *ATLAS Pythia 8 tunes to 7 TeV data*, Technical report, CERN, Geneva (2014), ATL-PHYS-PUB-2014-021
- [105] W. Lukas, *Fast Simulation for ATLAS: Atfast-II and ISF*, J. Phys. Conf. Ser. **396(2)**, 022031 (2012)
- [106] E. Bothmann, et al., *Event generation with Sherpa 2.2*, SciPost Phys. **7**, 034 (2019)
- [107] J. Alwall, et al., *The automated computation of tree-level and next-to-leading order differential cross sections, and their matching to parton shower simulations*, JHEP **2014(7)** (2014)
- [108] ATLAS Collaboration, *Electron and photon performance measurements with the ATLAS detector using the 2015-2017 LHC proton-proton collision data*, JINST **14(12)** (2019)
- [109] ATLAS Collaboration, *Performance of electron and photon triggers in ATLAS during LHC Run 2*, Eur. Phys. J. C **80(1)** (2020)
- [110] M. Cacciari, G. P. Salam, G. Soyez, *The anti- k_t jet clustering algorithm*, JHEP **2008(04)** (2008)
- [111] ATLAS Collaboration, *Jet reconstruction and performance using particle flow with the ATLAS Detector*, Eur. Phys. J. C **77(7)** (2017)

- [112] ATLAS Collaboration, *Performance of pile-up mitigation techniques for jets in pp collisions at $\sqrt{s} = 8$ TeV using the ATLAS detector*, Eur. Phys. J. C **76(11)** (2016)
- [113] ATLAS Collaboration, *ATLAS flavour-tagging algorithms for the LHC Run 2 pp collision dataset*, Eur. Phys. J. C **83** (2023)
- [114] J. Erdmann, et al., *A likelihood-based reconstruction algorithm for top-quark pairs and the KLFitter framework*, Nucl. Instrum. Methods Phys. Res. A **748**, 18 (2014)
- [115] M. J. Fenton, et al., *Permutationless many-jet event reconstruction with symmetry preserving attention networks*, Phys. Rev. D **105(11)** (2022)
- [116] A. Shmakov, et al., *SPANet: Generalized permutationless set assignment for particle physics using symmetry preserving attention*, SciPost Physics **12(5)** (2022)
- [117] M. J. Fenton, et al., *Reconstruction of Unstable Heavy Particles Using Deep Symmetry-Preserving Attention Networks*, Commun Phys **7** (2024)
- [118] B. A. Betchart, R. Demina, A. Harel, *Analytic solutions for neutrino momenta in decay of top quarks*, Nucl. Instrum. Methods Phys. Res. A **736**, 169 (2014)
- [119] L. Sonnenschein, *Analytical solution of ttbar dilepton equations*, Phys. Rev. D **73**, 054015 (2006), [Erratum: Phys.Rev.D 78, 079902 (2008)]
- [120] DØ Collaboration, *Measurement of the Top Quark Mass Using Dilepton Events*, Phys. Rev. Lett. **80**, 2063 (1998)
- [121] ATLAS Collaboration, *Measurement of Top Quark Polarization in Top-Antitop Events from Proton-Proton Collisions at $\sqrt{s}=7$ TeV Using the ATLAS Detector*, Technical report (2013)
- [122] M. Bähr, et al., *Herwig++ physics and manual*, Eur. Phys. J. C **58(4)** (2008)
- [123] J. Bellm, et al., *Herwig 7.0/Herwig++ 3.0 release note*, Eur. Phys. J. C **76(4)** (2016)
- [124] J. Bellm, et al., *Herwig 7.1 Release Note* (2017), 1705.06919
- [125] L. A. Harland-Lang, et al., *Parton distributions in the LHC era: MMHT 2014 PDFs*, Eur. Phys. J. C **75(5)** (2015)
- [126] H. Brooks, P. Skands, *Coherent showers in decays of colored resonances*, Phys. Rev. D **100(7)** (2019)

Bibliography

- [127] P. Artoisenet, et al., *Automatic spin-entangled decays of heavy resonances in Monte Carlo simulations*, JHEP **2013(3)** (2013)
- [128] ATLAS Collaboration, *Measurements of observables sensitive to colour reconnection in $t\bar{t}$ events with the ATLAS detector at $\sqrt{s} = 13$ TeV*, Eur. Phys. J. C **83(518)** (2023)
- [129] J. Butterworth, et al., *PDF4LHC recommendations for LHC Run II*, J. Phys. G **43(2)**, 023001 (2016)
- [130] ATLAS Collaboration, *Electron reconstruction and identification in the ATLAS experiment using the 2015 and 2016 LHC proton-proton collision data at $\sqrt{s} = 13$ TeV*, Eur. Phys. J. C **79(8)** (2019)
- [131] ATLAS Collaboration, *Jet energy scale and resolution measured in proton-proton collisions at $\sqrt{s} = 13$ TeV with the ATLAS detector*, Eur. Phys. J. C **79** (2020)
- [132] C. Zhang, et al., *Experimental Validation of Quantum Steering Ellipsoids and Tests of Volume Monogamy Relations*, Phys. Rev. Lett. **122**, 070402 (2019)
- [133] A. Pinto, et al., *Uncertainty components in profile likelihood fits*, Eur. Phys. J. **84** (2024)
- [134] J. A. Raine, et al., *Fast and improved neutrino reconstruction in multineutrino final states with conditional normalizing flows*, Phys. Rev. D **109(1)** (2024)

A. Uncertainty Estimation of Quantum Discord

A.1. Uncertainty Propagation of the Von Neumann Entropy

Take a generic differentiable matrix function $f(X)$. Its differential is $df(X) = L_f(X)(dX)$ for small dX and some linear operator L_f (the Fréchet Derivative). We have

$$f(X + dX) \approx f(X) + L_f(X)(dX) \quad (\text{A.1})$$

such that

$$\text{Tr}[f(X + dX)] = \text{Tr}[f(X)] + \text{Tr}[L_f(X)(dX)] = \text{Tr}[f(X)] + d \text{Tr}[f(X)]. \quad (\text{A.2})$$

Introduce a matrix E_{ij} which is 1 at (i, j) and 0 everywhere else. The differential of the trace is then:

$$d \text{Tr}[f(X)] = \text{Tr}[L_f(X)(dX)] = \text{Tr}[dX L_f(X)] \quad (\text{A.3})$$

$$= \text{Tr}[dX_{ij} E_{ij} L_f(X)] = dX_{ij} \text{Tr}[E_{ij} L_f(X)], \quad (\text{A.4})$$

since dX_{ij} is a scalar. It follows:

$$\frac{\partial \text{Tr}[f(X)]}{\partial X_{ij}} = \text{Tr}[E_{ij} L_f(X)] = L_f(X)_{ji} \rightarrow E_{ij} \text{ "pulls out" the } (j, i)\text{th component} \quad (\text{A.5})$$

Now take $f(X) = X \log X$, such that $L_f(X) = \mathbb{1} + \ln X$:

$$\frac{\partial \text{Tr}[X \ln X]}{\partial X_{ij}} = (\mathbb{1} + \ln X)_{ij} \quad (\text{A.6})$$

A. Uncertainty Estimation of Quantum Discord

The Von Neumann entropy is $S = \text{Tr}[X \log_2 X] = \text{Tr}[X \ln X / \ln 2] = 1 / \ln 2 \text{Tr}[f(X)]$ and its variance is:

$$V[S] = \sum_{i,j} \left(\frac{\partial S}{\partial X_{ij}} \sigma_{ij} \right)^2 = \sum_{i,j} \left(\frac{1}{\ln 2} \cdot (\mathbb{1} + \ln X)_{ji} \sigma_{ij} \right)^2, \quad (\text{A.7})$$

where σ_{ij} is the uncertainty on X_{ij} .

$$\Rightarrow \sigma_S = \frac{1}{\ln 2} \sqrt{\sum_{i,j} (\mathbb{1} + \ln X)^T \cdot \sigma} \quad (\text{A.8})$$

A.2. Uncertainty Propagation of the Construction of the Density Matrices

Spin Density Matrix

The spin density matrix ρ of the two-qubit state is given by Equation (2.7). The density matrix containing the propagated uncertainties can be constructed using this

$$\sigma_\rho = \left(\sqrt{\sum_{i=1}^3 \left(\sigma_{B_i^+}^2 (\sigma^i)^2 \otimes \mathbb{1}_2 + \sigma_{B_i^-}^2 \mathbb{1}_2 \otimes (\sigma^i)^2 \right) + \sum_{i,j=1}^3 \sigma_{C_{ij}}^2 (\sigma^i)^2 \otimes (\sigma^j)^2} \right) / 4, \quad (\text{A.9})$$

where the absolute value is taken for any complex number.

Partial Trace of Spin Density Matrix

The partial trace over the first qubit can be calculated as

$$\rho_1 = \text{Tr}_1(\rho) = \sum_k \langle k | \rho | k \rangle = \frac{1}{2} \left(\mathbb{1} + \sum_i B_i^- \sigma_i \right), \quad (\text{A.10})$$

leading to the uncertainty propagation of

$$\sigma_{\rho_1} = \left(\sqrt{\sum_{i=1}^3 \sigma_{B_i^-}^2 (\sigma^i)^2} \right) / 2. \quad (\text{A.11})$$

The analogous relations hold for the partial trace over the second qubit, but switching $B^- \leftrightarrow B^+$.

Conditional Spin Density Matrix

The conditional spin density matrix when fixing the second qubit in the state $|\pm \hat{n}\rangle$ is given by

$$\rho_{\hat{n}} = (\mathbb{1} + \sum_i B_{\hat{n},i}^+ \sigma_i) / 2, \quad (\text{A.12})$$

which leads to the uncertainty propagation of

$$\sigma_{\rho_{\hat{n}}} = \left(\sqrt{\sum_i (B_{\hat{n},i}^+ \sigma_i)^2} \right) / 2. \quad (\text{A.13})$$

The probability to measure the second qubit in $|\pm \hat{n}\rangle$, $p_{\hat{n}} = (1 + \hat{n} \cdot B^-) / 2$ leads to an uncertainty propagation of

$$\sigma_{p_{\hat{n}}} = \left(\sqrt{\sum_i (\hat{n}_i B_i^-)^2} \right) / 2. \quad (\text{A.14})$$

Again, the analogous relations hold for the conditional spin density matrix and conditional probability for the second qubit but switching $B^+ \leftrightarrow B^-$.

A.3. Uncertainty Estimation due to the Patch Size

The theoretical predictions for the quantum discord include a minimization over the Bloch sphere, which is theoretically done point-wise analytically. With real data, it cannot be done pointwise but with fixed-size patches. Due to the size of the patch, an extra uncertainty is introduced. This uncertainty is estimated via propagation of the size in θ $\sigma_\theta = \pi / (2N_\theta)$ and ϕ $\sigma_\phi = \pi / N_\phi$ as an uncertainty through the calculation. This leads to

$$\sigma_{\hat{n}} = \left(\begin{array}{c} \sqrt{\sigma_\theta^2 (\cos \phi \cos \theta)^2 + \sigma_\phi^2 (\sin \theta \sin \phi)^2} \\ \sqrt{\sigma_\theta^2 (\sin \phi \cos \theta)^2 + \sigma_\phi^2 (\sin \theta \cos \phi)^2} \\ \sigma_\theta \sin \theta \end{array} \right), \quad (\text{A.15})$$

which results in an additional uncertainty on the polarisation in the patch $B_{\hat{n}}^\pm$ according to Equation (2.34)

$$\sigma_{B_{\hat{n}}^\pm} = \left(\begin{array}{c} \sigma_{\hat{n},x} (B_z^\mp \hat{n}_z C_{x,x} + B_y^\mp \hat{n}_y C_{x,x} - B_x^\pm B_x^\mp) / (1 + \hat{n} \cdot B^\mp)^2 \\ \sigma_{\hat{n},y} (B_z^\mp \hat{n}_z C_{y,y} + B_x^\mp \hat{n}_x C_{y,y} - B_y^\pm B_y^\mp) / (1 + \hat{n} \cdot B^\mp)^2 \\ \sigma_{\hat{n},z} (B_x^\mp \hat{n}_x C_{z,z} + B_y^\mp \hat{n}_y C_{z,z} - B_z^\pm B_z^\mp) / (1 + \hat{n} \cdot B^\mp)^2 \end{array} \right), \quad (\text{A.16})$$

with the overall spin polarisations B and spin correlations C .

B. Additional Figures for the Quantum Discord of the Anti-Top Quark

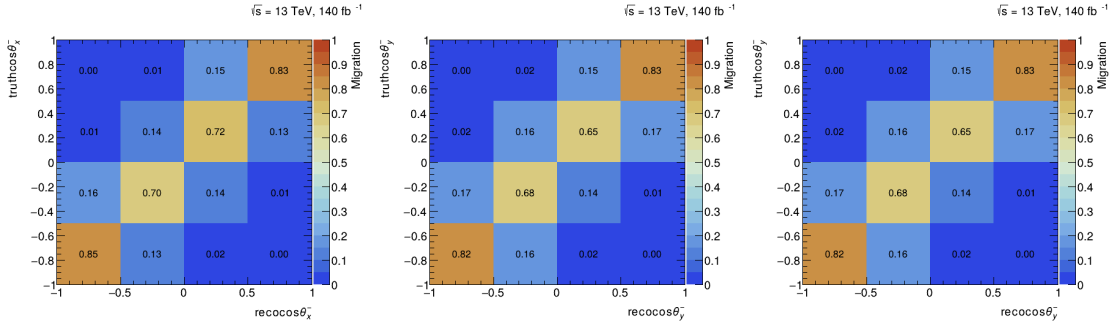


Figure B.1.: Migration matrices for the distributions of $\cos \theta_i^-$ in the region $-\pi < \phi^- < -8/9\pi$, $\pi/2 < \theta^- < 5/9\pi$, used for the unfolding procedure.

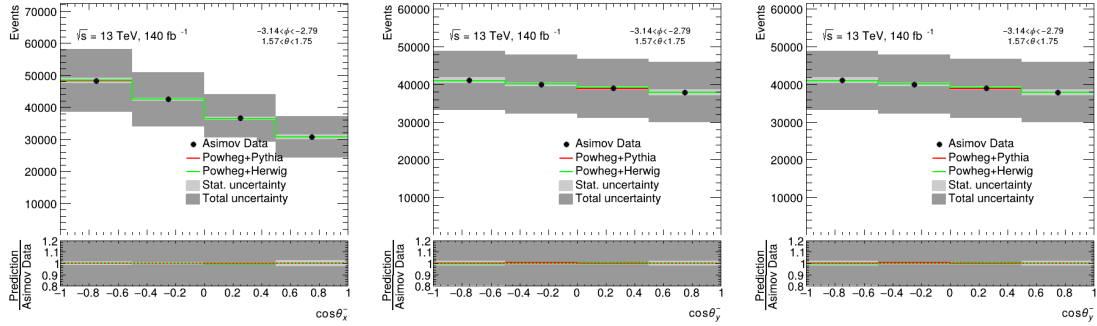


Figure B.2.: Results of the unfolding procedure using Asimov-data, in the region $-\pi < \phi^- < -8/9\pi$, $\pi/2 < \theta^- < 5/9\pi$. The nominal prediction using POWHEG+PYTHIA is shown, as well as the alternative predictions using POWHEG+HERWIG. The uncertainty is represented by the grey uncertainty band.

B. Additional Figures for the Quantum Discord of the Anti-Top Quark

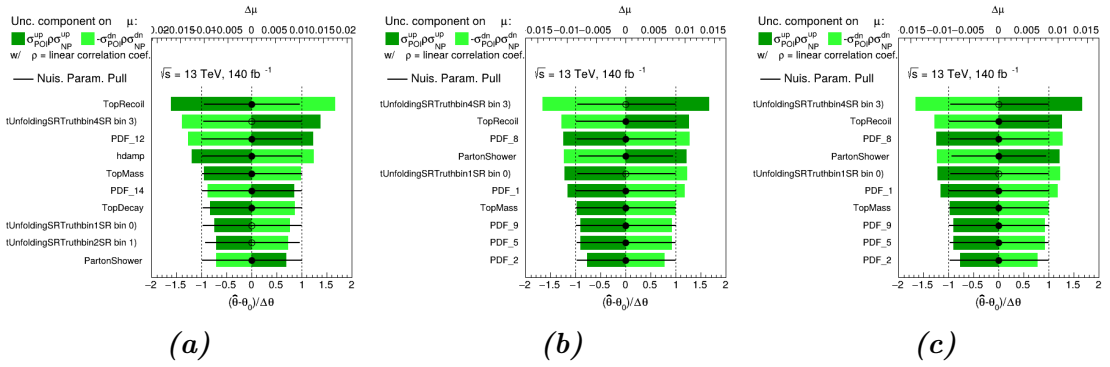


Figure B.3.: Ranking of the contribution of the nuisance parameters to the total uncertainty of the parameter of interest **a)** B_x^- , **b)** B_y^- and **c)** B_z^- , in the region $-\pi < \phi^- < -8/9\pi$, $\pi/2 < \theta^- < 5/9\pi$. The values are extracted from the off-diagonal elements of the fit covariance matrix, which correspond to the covariance of the nuisance parameter with the parameter of interest.

#Thanks

My first thanks of this thesis definitely belongs to Prof. Dr. Arnulf Quadt who supported everything I did over the past years. He not only supervised my Bachelor's and Master's Thesis, but awoke my passion for particle physics at first. I want to thank him for all the opportunities he gave me to extend my knowledge at various conferences. It was always obvious that he especially supports women in physics and I will always remember that.

I also want to thank Prof. Dr. Ariane Frey for agreeing to be my second referee for this thesis. I also want to thank the 'Studienstiftung des Deutschen Volkes' for supporting me through my BSc and MSc degree.

My biggest gratitude for this thesis belongs to Dr. Baptiste Ravina without whom this thesis would not have been possible. He introduced me to the world of quantum information with top quarks and has been a steady companion during my academic journey. It was a pleasure to work with him, and I would always choose to do it again.

I also want to thank Dr. Elizaveta Shabalina for all her advice and help and for sharing her knowledge. I especially would like to thank Dr. Sebastian Wozniewski for his patience and help with the GoeGrid, whether it was a GoeGrid- or a me-problem. I also thank Dr. Steffen Korn for proofreading this thesis.

I want to highlight the excellent services of Anne Gaa as our equal-opportunities officer (or, more accurately, "equalizer"). I also consider myself incredibly lucky to have had so many supportive colleagues with open ears for all my worries in these troubling times. I wouldn't have wanted to do it without you.

Lastly, I want to thank all the people who have accompanied and supported me through my five years at the university. I hope to welcome you all at the next step of my adventure in Geneva! But for now, it's time to go, and get wasted like all my potential!

Erklärung

nach §17(9) der Prüfungsordnung für den Bachelor-Studiengang Physik und den Master-Studiengang Physik an der Universität Göttingen: Hiermit erkläre ich, dass ich diese Abschlussarbeit selbständig verfasst habe, keine anderen als die angegebenen Quellen und Hilfsmittel benutzt habe und alle Stellen, die wörtlich oder sinngemäß aus veröffentlichten Schriften entnommen wurden, als solche kenntlich gemacht habe.

Darüberhinaus erkläre ich, dass diese Abschlussarbeit nicht, auch nicht auszugsweise, im Rahmen einer nichtbestanden Prüfung an dieser oder einer anderen Hochschule eingereicht wurde.

Göttingen, den 30. September 2024



(Theresa Reisch)